THE EFFECT OF FLUID VISCOELASTICITY IN SOFT ELASTOHYDRODYNAMIC LUBRICATION

A THESIS SUBMITTED TO

THE GRADUATE SCHOOL OF ENGINEERING AND SCIENCE

OF BILKENT UNIVERSITY

IN PARTIAL FULFILLMENT OF THE REQUIREMENTS FOR

THE DEGREE OF

MASTER OF SCIENCE

IN

MECHANICAL ENGINEERING

By

Mehmet Hakan Sarı

July 2024

The effect of fluid viscoelasticity in soft elastohydrodynamic lubrication
By Mehmet Hakan Sarı
July 2024

We certify that we have read this thesis and that in our opinion it is fully adequate, in scope and in quality, as a thesis for the degree of Master of Science.

Luca, Biancofiore(Advisor)

İlker, Temizer

Carmine, Putignano

Approved for the Graduate School of Engineering and Science:

Orhan Arıkan
Director of the Graduate School

ABSTRACT

THE EFFECT OF FLUID VISCOELASTICITY IN SOFT ELASTOHYDRODYNAMIC LUBRICATION

Mehmet Hakan Sarı
M.S. in Mechanical Engineering
Advisor: Luca, Biancofiore
July 2024

Lubrication is crucial across various industries and natural environments to prevent direct contact between solid surfaces. Elastohydrodynamic lubrication specifically addresses situations where solid surfaces are likely to deform. Viscoelastic additives in fluids can alter lubrication characteristics significantly. Reduced models available today efficiently solve viscoelastic equations numerically in thin film contacts, surpassing direct numerical computations in efficiency. Employing numerical techniques, viscoelastic fluids within the linear elastic regime are successfully analyzed. Further investigations into contraction geometries aim to elucidate findings on soft lubrication. An elementary experimental study was conducted to demonstrate the effect of viscoelasticity on load-carrying capacity. A comprehensive literature review provided the necessary mathematical foundation for understanding viscoelasticity and solid deformation. Concepts such as the upper convected time derivative and polymeric constitutive equations were summarized. Reynolds equation, incorporating polymeric elastic stress, is combined under the thin film lubrication approximation. Viscoelasticity is characterized by the non-dimensional number De, which represents the ratio of polymer relaxation time to observation time t/t_o . In the context of lubrication, the observation time t/t_o is defined as L/U, where L is the length of the channel and U is the speed of flow. The reduced numerical methods are based on finite differencing schemes and linearization of the flow with respect to De. The linearized flow using the Oldroyd-B constitutive model forms the basis for a more complex numerical model that is compatible with direct numerical solvers. A unique semi-implicit method has been developed to solve

nonlinear stress equations. The coupling between solid and fluid solvers is fully explained with schematics, and the boundary element method is integrated with the finite difference method. Prior to presenting results, the developed numerical methods were validated against previous outcomes published in journal articles. Elastohydrodynamic lubrication results indicate that the friction coefficient decreases with increasing De at high deformabilities. To further illustrate EHL cases, step-like channels were studied. Finally, experimental data is provided for future use, concluding with remarks to contextualize our findings.

Keywords: elastohydrodynamic lubrication, fluid viscoelasticity, Oldroyd-B model, polymeric additives.

ÖZET

VİSKOELASTİK AKIŞKANLARİN YUMUŞAK ELASTOHİDRODİNAMİK YAĞLAMAYA ETKİSİ

Mehmet Hakan Sarı
Makine Mühendisliği, Yüksek Lisans
Tez Danışmanı: Luca, Biancofiore
Temmuz 2024

Tabanı kayganlaştırma, katı yüzeyler arasında doğrudan teması önlemek için çeşitli endüstrilerde ve doğal ortamlarda hayati önem taşır. Özellikle elastohidrodinamik lubrikasyon, katı yüzeylerin deformasyona uğrama olasılığının yüksek olduğu durumları ele alır. Sıvılara eklenen viskoelastik katkı maddeleri, lubrikasyon özelliklerini önemli ölçüde değiştirebilir. Günümüzde mevcut azaltılmış modeller, viskoelastik denklemleri ince film temasında sayısal olarak verimli bir şekilde çözebilir ve doğrudan sayısal hesaplamaları geride bırakabilir. Sayısal teknikler kullanılarak, viskoelastik sıvılar lineer elastik rejimde başarıyla analiz edilmektedir. Daralma geometrilerine yönelik daha ileri araştırmalar, yumuşak lubrikasyon üzerine bulguları açıklığa kavuşturmayı amaçlamaktadır. Viskoelastikiyetin yük taşıma kapasitesi üzerindeki etkisini göstermek için temel bir deneysel çalışma yapılmıştır. Kapsamlı bir literatür taraması, viskoelastikiyeti ve katı deformasyonu anlamak için gerekli matematiksel temeli sağlamıştır. Üst taşınmış zaman türevi ve polimerik kurucu denklemler gibi kavramlar özetlenmiştir.Polimerik elastik gerilim içeren Reynolds denklemi, ince film lubrikasyon yaklaşımı altında birleştirilmiştir. viskoelastisite, polimer rahatlama süresinin gözlem süresine oranını, t/t_o, temsil eden birimsiz sayı olan De ile karakterize edilir. Lubrikasyon bağlamında, gözlem süresi t_o kanal uzunluğu L ve akış hızı U tarafından tanımlanır. Azaltılmış sayısal yöntemler, sonlu fark şemalarına dayanmakta ve De ye göre akışın lineerleştirilmesini içermektedir. Oldroyd-B kurucu modeli kullanılarak doğrusallaştırılmış akış, doğrudan sayısal çözücülerle uyumlu daha karmaşık bir sayısal modelin temelini

oluşturur. Doğrusal olmayan gerilim denklemlerini çözmek için benzersiz yarı-örtülü bir yöntem geliştirilmiştir. Katı ve sıvı çözücüler arasındaki bağlantı şematiklerle tam olarak açıklanmış ve sınır elemanları yöntemi sonlu fark yöntemiyle entegre edilmiştir. Sonuçları sunmadan önce, geliştirilen sayısal yöntemler daha önce yayınlanan makalelerde elde edilen sonuçlarla doğrulanmıştır. Elastohidrodinamik lubrikasyon sonuçları, yüksek deformabilite durumlarında De ile artan sürtünme katsayısının azaldığını göstermektedir. EHL vakalarını daha iyi anlatmak için basamaklı kanallar incelenmiştir. Son olarak, gelecekteki kullanım için deneysel veriler sunulmuş ve bulgularımızı bağlamlandırmak için açıklamalar yapılmıştır.

Anahtar sözcükler: elastohidrodinamik yağlama, akışkan viskositesi, Oldroyd-B modeli, polimerik katkı maddeleri .

Acknowledgement

Foremost, I would like to express my deepest gratitude to my advisor. During this period, Dr. Biancofiore showed his full support and conidence in my work and was always available whenever I needed his guidance.

I would like to acknowledge the Turkish National Research Agency (TUBITAK) for supporting this work under the project 221M576. Experimental work has been conducted under Austrian COMET-Program (K2, program InTribology2, FFG no. 906860, project coordinator AC2T research GmbH) for 3 months.

I would like to thanks to Yunus Altıntop and Ahmet B. Yıldırım for being good fellows in our windowless prison office. Without them it will be so hard to endure my graduate life in Bilkent.

I graditude Carmine Putignano for welcoming me in Bari and sharing Poliba's facilities. I meet wonderful people in Bari which I never forget.

I am grateful to AC2T family for providing me the opportunity to deepen my subject with experimental instruments and a very joyful research enviroment. I specifically thanks to Shreyas Jalikop for all his effords and contributions. Also, great support from Krenn Stephen, Bianca Aigner and Gerald Gruber for carrying experiments.

I am quite in debt to Dr.Humayun Ahmed for very fruitful discussions, contributions and being a fellow for scientific thinking. And ofcourse another good friend sharing our precious prison.

Finally, I will like to give all thanks to my family, who always push me to learn

more, think more and read more. I had a great experience not only in science but all aspects of my life during this three years.

Contents

List of Figures

List of Tables

Chapter 1

Introduction

Lubrication has been a prominent field of study in the mechanical domain for over a century. It is closely associated with tribology, which encompasses the scientific and technological investigation of interacting and contacting surfaces [1]. This includes the examination of lubrication, friction, and wear in various mechanical systems, such as bearings, cams, pistons, cutting tools, and others, which play a crucial role in transmitting power and facilitating motion in industrial applications. Understanding tribological contacts is essential in the context of global energy consumption, as approximately 23 percent of the total energy loss is attributed to dissipative heat generated by these contacts [2]. However, lubrication is not confined to the industrial domain alone; its applications extend to diverse scientific research areas. For instance, it is used in surface design applications [3], nanotechnology studies [4], and the investigation of biological intersections [5]. Moreover, polymers and polymeric composites are extensively used in industrial applications due to their cost-effectiveness and lighter weight compared to metals. Rubber bearings, seals, and dampers are examples where polymers exhibit superior performance over their metal counterparts [6, 7]. Studies have been conducted on tilted rubber pads under

hydrodynamic lubrication, exploring aspects such as energy dissipation and elastic deformation [8].

Lubrication plays a crucial role in reducing friction between solid-solid contacts, thereby preventing wear and energy loss. When solid contacts are in relative motion, the surfaces are susceptible to deformation due to the high shear stress and heat generated by friction. This is especially problematic in machinery with periodic movements, as it significantly reduces efficiency, making lubrication indispensable. The addition of solid adhesives in the form of coatings, fluid-type, or mixed lubricants helps prevent direct solid-solid contact. The study of lubricant types has become a vast field, with mineral-based oils being the traditional choice. However, there has been a shift towards exploring alternatives such as bio-lubricants and polymer-added high-temperature durable lubricants, driven by the need to improve durability, sustainability, efficiency, and reduce pollution [9], [10]. As technology progresses, there have been advancements in viscosity enhancers, anti-wear, and friction additives. Interestingly, there is a trend towards using rubber-based components instead of metallic ones, primarily due to their advantages in terms of cost, lightweight, and performance [2]. The broad range of lubricants, especially biofluids, presents complex rheological behaviors, which have attracted significant attention in the lubrication field [11]. With the introduction of more complex fluids, classic lubrication theories are being reevaluated, and new concepts are emerging to address these novel challenges.

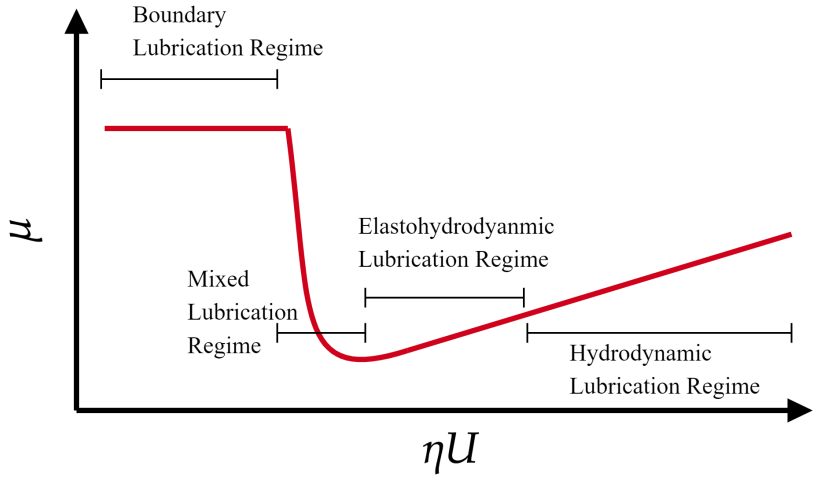

Figure 1.1: The lubrication regimes

Mechanical parts that require lubrication often experience load and sliding motion, leading to changes in lubrication properties. This distinction has led to the categorization of different lubrication types based on specific situations, which are depicted in Fig.1.1 in terms of friction and viscous force νU. Complete lubrication occurs when sliding surfaces are fully and continually separated from each other, floating in the lubricant film, as described by Reynolds [12]. However, under high carrying loads, low entrainment speeds, or intentional design, the lubricant film may become very thin, causing the surfaces to touch each other, leading to what is known as boundary lubrication. In this scenario, the chemical nature of the boundaries also plays a critical role [13]. Boundary lubrication exhibits distinct physics, and the choice of lubricant becomes more complex, considering the boundary conditions. Instead of relying on a lubricant film, surface-active materials like long-chain polar compounds form mono-molecular layers attached to the surfaces [14]. In this case, the lubricant's bulk properties, such as viscosity, do not play a significant role, as molecular interactions take precedence. Surprisingly, even with the solids in direct

contact, the presence of a very thin lubricant layer can still have a substantial impact on wear and friction [15]. Therefore, considering chemical properties, corrosion, wear, and temperature is essential in boundary lubrication [16]. The type of contact is of paramount importance when studying boundary lubrication physics. Even in cases where there is an adequate fluid film separating the surfaces, the surface type significantly influences lubrication properties in various mechanical parts, such as journal bearings, ball bearings, cams, etc. Thus, factors like contact area, load, and relative velocity of the surfaces become significant in determining the effectiveness of lubrication in these situations.

As the field of lubrication has evolved, it has branched out into various divergent parts, deviating from the classical lubrication theory. These differences encompass aspects such as surface roughness, non-uniform internal faces, changes in lubricant density, and the use of Non-Newtonian lubricants [17]. Over the years, researchers have conducted experiments and developed theoretical explanations to comprehensively understand lubrication in various scenarios. Among these differences, the micro-texture design of interacting surfaces stands out as a critical topic influencing friction and load capacity performance. This realization has led to the incorporation of micro pockets and grooves in commercial products and has spurred numerous ongoing studies, especially in face seals [18]. In vessel rotary shafts, lip seals has also attention as the performance of sealing is directly related to ocean pollution [19, 20].

Etsion's work in constructing a mathematical model for micro-designed structured and porous surfaces has significantly advanced the topic of surface design. The model emphasizes the importance of cavitation occurring in each pore, leading to an integrated effect on the bearing's carrying capacity [21]. Cavitation, which naturally arises from using micro-designed textures, becomes a main factor in enhancing lubrication performance. Just like the roughness of metal surfaces, the surface texture of rubber materials can also be seen as an irregularity. As a result, the shape and

dimensions of the surface texture play a vital role in determining friction and load capacity [17, 18]. Consequently, cavitation becomes an essential consideration in texture design across various lubrication types.

The latest studies of lubrication are not limited by machinery and industrial applications. Thin films can commonly be found in biological living. As bio-aspired mechanical systems and materials are gaining more popularity in the field of engineering, there are examples regarding lubrication and contact mechanics. Especially, soft structures are quite beneficial in robotics due to their structural rigidity and lightweight [22]. Their counterpart can take place in living bodies, such as animal cell dynamics and bio-surface mechanics [23, 24]. Following biological soft surfaces, there are numerous natural bio-fluids both behaving like Newtonian and non-Newtonian. The non-Newtonian fluids present in human joints (synovial fluid) [5, 25], mouth (saliva) [26], eye (aqueous humour) [27] and blood flows [28] where they come into contact with soft tissues, brings attention to the study of complex fluids within the scope of soft lubricated contacts. The idea of studying complex fluid and soft bodies has also been brought up in previous studies [29].

Following this brief introduction, the fundamental aspects of lubrication theory are outlined. While this field has broad applications and encompasses a wide range of study topics, the focus narrows down to the specific area of interest by following the subsequent subsections.

1.1 Elastohydrodynamic Lubrication Review

The characteristics of mechanical contacts change based on various factors, such as the geometrical properties of machine elements, the entrainment speed, and the carried load. When machine elements rest on a fluid film, the contact area's width

determines whether the surfaces are conformal or non-conformal. In the case of conformal surfaces, like those found in journal bearings, the contact area is wide, and the sliding surfaces have a large area in contact with each other [30]. The geometry of the sliders is comparable in size to their entire bodies, and the fluid film is considered as a bulk medium. On the other hand, non-conformal surfaces are heavily influenced by Herzt's studies on elastic contact, where the contact pressure occurs between two bodies and does not significantly affect far points from the contact [31]. This assumption is known as the Hertzian or Elastic Half Space assumption. In non-conformal surfaces, the contact pressure is highly concentrated on the touching surfaces, and the deformation is small enough to neglect linear elastic theories concerning the scaling of deformation and radii of curvature of the contact area. The dimensions of the contacting solid surfaces are large enough that the stress due to contact has no effect on the shape of the solids and how they are supported. Under these conditions, considering the contact area as a semi-infinite plane surface is referred to as the elastic half-space. Non-conformal contact can take various forms, such as point, line, or elliptical contacts, and each type requires independent consideration of contact pressure and deformation [32]. However, this approach is invalid for conformal surfaces, where a different approach should be employed.

Conformal surfaces are particularly suitable for use in hydrodynamic lubrication (HL), which is commonly observed in journal bearings and slider bearings. In HL, the solid-fluid interaction area is substantial, leading to relatively low pressures being generated. As a result, bulk deformations of the solids can be neglected, and the lubricant's viscosity is often assumed to remain unchanged, treated as a Newtonian fluid. Typically, one might expect the fluid to simply slide under the load caused by gravity. However, when there is sufficient speed, hydrodynamic lubrication conditions are established, and the bearing converges to a film thickness that results in positive pressure. The pressure generated by the squeezed film counteracts the bearing load, effectively supporting the load. Although the generated pressure is usually too low to

significantly deform the bearing surfaces, the film thickness depends on the velocity of the bearing and the contact properties avoids direct contact. By employing conformal surfaces in hydrodynamic lubrication, the bearing's efficiency is enhanced, and wear between solid components is minimized. This lubrication mechanism proves to be critical in ensuring the smooth and efficient operation of machinery and is extensively utilized in various industrial applications.

Nonconformal surfaces are better suited for elastohydrodynamic lubrication (EHL) due to their ability to adapt to changes in the contact area caused by applied loads on the bearing. Unlike hydrodynamic lubrication (HL), where the contact area remains relatively constant, EHL involves the generation of a fluid film between the nonconformal contacts, but this film is thinner compared to HL. In EHL, the pressure generated is significant enough to elastically deform the bearing surfaces, making the film thickness dependent on the elastic modulus of the bearings. EHL can be categorized into two types: hard and soft. In hard EHL, the pressure can reach up to 4 GPa, leading to non-Newtonian effects on the lubricant. Under these extreme pressures, the lubricant's viscosity changes significantly due to the magnitude of the pressure. Hard EHL usually occurs in contact surfaces made of metal-type materials. On the other hand, soft EHL is observed in soft materials like polymeric materials and rubber, where even light loads can cause significant surface deformations. In soft EHL, the load created by the lubrication typically reaches a maximum of 1 MPa, which does not disturb the lubricant's viscosity, and the assumption of a Newtonian fluid remains valid [15]. In both hard and soft EHL, the critical aspect is that the fluid film formed between the surfaces prevents direct contact, reducing friction and wear while improving the overall efficiency of the bearing. The typical geometry with deformation is depicted in Fig.1.2

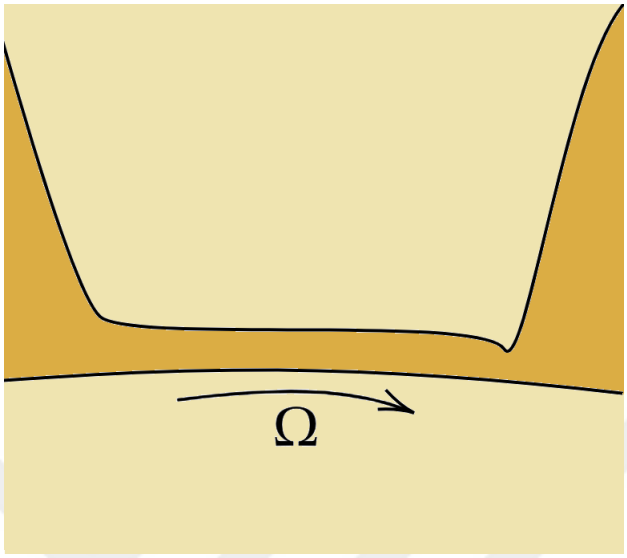

Figure 1.2: A typical EHL showcase with deformed top body in gear contacts or bearings where bottom body rotates with angular speed Ω

Lubricants exhibiting non-Newtonian behaviors are widely discussed topics for several applications. Most of the time, in the case of hydrodynamic lubrication, the generated pressure does not significantly affect the fluid viscosity. However, as mentioned earlier, a large variety of lubricants can show shear-thinning or thickening effects, or due to some additives, the fluid begins to behave as non-Newtonian [10]. To describe these kinds of effects, the term generalized Newtonian fluid (GNF) is used. GNF encompasses polymeric additives, temperature effects, and piezoviscosity effects.

In the case of hard elastohydrodynamic lubrication, the change in fluid viscosity is an essential part of the process, where there is a wide range of experimental and numerical studies focused on this problem. An extensive overview of these studies has been conducted by Spikes, where the studies are introduced under EHL over the last 60 years [33].

Experiments in the field of lubrication have primarily focused on the automotive industry, particularly investigating motor oil properties under elastohydrodynamic lubrication (EHL) conditions. Researchers like Bair have examined shear-thinning effects using various models that consider time and shear stress-dependent viscosity [34]. Additionally, the study of motor oil with polymer additives has been explored, taking into account the contribution of polymer shear stress and natural shear thinning in EHL contacts [35, 36]. Piezo-viscosity, as a significant non-Newtonian fluid property in EHL due to high pressure, has also been subject to numerous investigations. Various piezo-viscosity models have been numerically explored for EHL line and point contacts, with the Roelands model being widely used to examine viscosity changes with pressure. For volume fraction effects, different approaches have been employed [37, 38]. Moreover, researchers have studied viscoelasticity in EHL line contacts, and experimental rheological studies on motor oil have been carried out by Bair et al. [39]. Similar investigations have been conducted for pure hydrodynamic lubrication conditions in journal bearings, where researchers have experimentally examined the elastic effects of polymers [40] and numerically studied them [41]. However, there is limited research that mathematically establishes viscoelastic polymeric fluids in the specific context of EHL. Further exploration of other viscoelastic formulations is warranted [42].

Numerical studies conducted by Wang et al. have explored various scenarios in elastohydrodynamic lubrication (EHL) contacts, considering viscoelastic, viscoplastic, and thermal effects, while using shear-stress dependent viscosity models for pure oil [43, 44]. Subsequent research has further focused on non-Newtonian effects, limited shear stress, and piezo-viscosity effects [45]. However, in many EHL applications, fluid viscoelasticity is often neglected, especially in non-polymer-added lubricants, where minimal memory effects are observed [46]. In the cases mentioned up to this point, non-Newtonian effects remain time-independent. However, in certain EHL scenarios or when polymer additives are used in lubricants, viscoelastic behavior may be present, introducing time-dependent non-Newtonian effects.

Viscoelastic fluids exhibit responses that account for both viscous shear and elastic shear. Additionally, the normal stress created by viscoelasticity can have a dominant effect [30]. To address these effects, the Reynolds equation must be extended, and a viscoelastic model should be employed to analyze the fluid behavior accurately. Viscoelasticity is particularly crucial in lubricants used in soft matter and bio-tribology topics, where its effect has not been fully revealed yet.

Accounting for solid deformation, there are several methodologies to solve elastic or plastic deformation based on Johnson's definition of non-conformal surfaces. The forces at the very end of the channel are ineffective in creating a deformation for the point of interest, thus leading to a convolution integral over the domain. This can be solved by the finite element method or boundary element method after the Green function is known.

Another interesting EHL case is when solid viscoelasticity is taken into account. In this case, the solid does not just deform independently of time but shows a memory effect. Thus, after deformation, the surface retaliates and tries to return to its original position, transiently changing the dynamics of the fluid. This case is called Viscoelastic EHL, shortly (VEHL). The deformation is described by the time-dependent creep function of the strain, whereas the surface-dependent pressure causes the deformation [47, 48]. For experimental work in VEHL, readers are referred to [49, 50].

1.2 Viscoelastic Fluid Models

Viscoelastic polymer fluid models are reviewed in this section. The viscoelastic models examined in this thesis diverge from shear-thinning effects caused by polymers. Despite shear-thinning being the crucial phenomenon at high-shear rate

flows, the thesis focuses purely on viscoelasticity, where the viscosity of the fluid remains the same. These fluids are generally referred to as Boger fluids, indicating that viscosity is independent of shear rate, named after David Boger's experimental studies on polymeric fluids [51].

Viscoelastic fluids exhibit both normal viscous behavior and the ability to relax, akin to springs within the fluid. In this context, polymeric additives, which consist of long chains of molecules connected via strong chemical bonds, behave like springs. Assuming each molecule acts as a bead, the chemical pulling and pushing of these beads relax compared to the fluid's time scale, thereby creating an elastic component within the fluid. The Fig.1.3 may represent a simple demonstration of a single fluid element possessing elasticity E along with viscosity η.

There are numerous theoretical and experimental studies aimed at fully understanding viscoelastic fluids in various areas of science and industry. Polymer melts, jet extrusions, manufacturing of rubber-like materials, and the discovery of new polymeric materials all require appropriate modeling to simulate polymeric substances alongside Newtonian fluids. While Newtonian fluids have been well-known for many decades, complex fluids suffer from a lack of a fully modeled theory. In the scientific community, theoretical advancements began developing after the Second World War with the introduction of synthetic rubber. The potential employment of polymeric substances in fluids accelerated research on constitutive relations. There are two main methods to construct constitutive equations: one relies on field theory, while the other is derived from kinetic theory [52].

An old but very common model is the Upper Convected Maxwell (UCM) model for describing viscoelastic materials. UCM is a general method applicable to materials that exhibit both viscous and elastic behavior, making it not limited to viscoelastic fluids alone. The UCM model is a simple framework consisting of two main parameters: E, the elasticity parameter, and η, the viscosity of the material [53].

The UCM formulation is based on a spring-damper model connected in series, as previously shown in Fig.1.3, which is named by Maxwell as it is a generalization of Maxwell material.

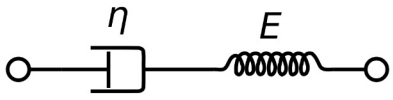

Figure 1.3: Spring damper model connected in series

The UCM model can be succinctly explained with equations to clarify how the system works. Consider the force applied to the two sides of the system, extending the line. The internal stress in the fluid of the damper is directly connected to the applied force in a Newtonian fluid relationship, in terms of η. However, there is a drawback for the force exerted by the spring during the time of extension, which is accounted for by E, the elasticity parameter, also known as the relaxation time for the fluid context and labeled with λ, representing the memory time for the system to return to its original position. The main characteristic of the elastic dumbbell turns out to be the relaxation time of a given material, represented by the spring. In polymer physics, the relaxation time (coefficient of the spring) is determined by the forces between internal bonds [54]. This is formulated by the following equation:

$$\boldsymbol{\tau} + \lambda \overset{\nabla}{\boldsymbol{\tau}} = 2\eta \boldsymbol{D} \tag{1.1}$$

where the right-hand side stands for viscous forces and $\boldsymbol{\tau}$ is elastic stress, $\overset{\nabla}{\boldsymbol{\tau}}$ is the upper convected time derivative of stress, also known as Oldroyd derivative. Eq.1.1 1D Maxwell material type version can easily derived with sufficient dynamic knowledge. Given that, another variation for UCM is the Oldroyd-B model, including

extra solvent viscosity or retardation time [55] making a more convenient and easier approach for viscoelastic fluid. With a small modification to the viscosity value, the Eq.1.1 can converted to the Oldroyd-B viscoelastic model which is also very common in modelling the polymer fluid flow and polymer melt. The main continuum description of the Oldryod-B equations can be found in Oldroyd's paper and his doctore thesis [56].

The time derivative that appears in UCM-type models requires further attention for explanation. Although it is derived in Sec.2.2.1, for introductory purposes, an intuition can be described as follows: The total time derivative gives the total rate of change of the given property for a fixed location. In fluid dynamics, most of the time, fluid particles are examined with translated locations, so the material derivative is introduced to observe the particle flow. This kind of location maintains its orientation but does not account for deformation or rotation. Furthermore, in this setup, the position vector of subsequent fluid is not connected to neighboring particles. Thus, a more convenient model is needed to account for co-deformations or co-rotational derivatives to capture fluids' memory effect during the flow and obtain a coordinate system which can deform and rotate in addition to translation. The upper convected time derivative, also known as the convected contravariant derivative, is used for the time derivative [57].

UCM and Oldroyd-B models provide simple yet effective formulations for viscoelastic fluids. However, over time, more complex models have been developed to address physical compatibility, as stress and relaxation time may nonlinearly link to velocity and shear rate. Hence, while preserving the structure of the equations, previous models can be modified by incorporating several physical relationships. For instance, the Giesekus model allows λ and η to be functions of the velocity gradient of flow [58].

To describe the rheology of long-chain polymers, Thien and Tanner developed

a nonlinear constitutive equation for the polymer stress tensor in the context of fluid motion, building upon Wiegel's formulation. Utilizing polymer network theory and the Boltzmann energy, they obtained a more accurate continuum model for the viscoelastic constitutive equation [59]. Despite several modifications over time, including the Phan-Thiner/Tanner (PTT) model, the original Thien and Tanner model remains well-accepted and common in the lubrication field due to its adequate fit with molecular considerations [60].

Another very common rheological model, introduced by Warner, is the finitely extensible nonlinear elastic (FENE) dumbbell model. This model formulates the force between two connected beads via an elastic spring in between a rigid dumbbell or an infinitely extendable Hookean spring dumbbell [61]. The complex mathematical layout of the FENE model was simplified by Peterlin's idea, as proposed by Bird, resulting in the construction of the FENE-P model, where the letter P refers to Peterlin [62]. The FENE-P model contains the same non-linear terms in stress as in PTT but includes extra variables and accounts for shear-thinning.

Another set of models, mainly referred to as Rivlin fluids, involve quadratic, cubic, and other expansions of the velocity gradient tensor and various combinations of the velocity gradient tensor with the stress field. For example, the Oldroyd-4 and Oldroyd-8 models are available to account for all combinations of shear rate. However, the Rivlin fluid model is mostly associated with second-order fluids in the literature [63]. Although attention to nonlinear constitutive equations is higher at the current stage, second-order fluid models are primarily comparable with the Oldroyd-B equations.

It's important to note that time effects are not considered in all non-Newtonian fluid cases. In several instances, viscoelasticity is too low for memory effects to be visible. However, in polymer solvents, as mentioned earlier, relaxation time is influenced by its internal structure and can exhibit memory effects on a continuum

scale. If this time scale λ becomes comparable to the time of the flow process, i.e., the time required for the flow characteristic length over fluid velocity, L/U, it can be assumed that memory effects play a crucial role in lubrication. To quantify this time dependence, the Deborah number, $De = \lambda U/L$, is used. For a Newtonian fluid, the Deborah number is zero. The De number can be related to another common quantity for describing fluid viscoelasticity, which is a measure of deformation rate in terms of elasticity, U/h, known as the Weissenberg number. This is the ratio of the relaxation time to the height of the contact over fluid speed, $Wi = \lambda U/h$, which accounts for the overall deformation rate of the lubricated contact with respect to the relaxation time.

1.2.1 High Wiessenberg Number Problem

There have been various solution approaches to the viscoelastic problem since its inception. Many of these solutions rely on numerical techniques and approximations using the constitutive equations discussed earlier. One direct approach involves using numerical methods to solve the Navier-Stokes equations with a non-Newtonian model. However, this approach has encountered challenges related to nonlinearity and what is known as the "High Weissenberg Number Problem" (HWNP) in the literature, which arises when the Weissenberg number becomes large [64].

It's important to note that the magnitude of the Weissenberg number leading to instability is problem-specific, and there is no universally defined threshold for HWNP. Throughout the history of addressing HWNP, research efforts have produced various solutions within the field of rheological computation. Owens & Philips have summarized these discussions, exploring the physical causes of the problem and presenting computational formulations developed up to the present [65].

To ensure stability in viscoelastic flows, direct numerical solutions have evolved

with various techniques summarized well in the review paper by Alves et al. [66]. One crucial and widely recognized problem is solving the contraction problem, which involves step-function changes in different ratios. The standard finite element method faces limitations due to strict time step requirements. As a result, the semi-Lagrangian finite volume method is commonly employed in such formulations. This method fixes grids using particle tracing techniques, as discussed by Phillips & Williams [67].

While increasing the number of grid points may appear to be a promising approach for capturing nonlinearities and steep derivatives, studies have shown that the High Weissenberg Number Problem (HWNP) remains independent of mesh configuration. This limiting Weissenberg number persists even with very fine mesh refinements, as demonstrated by Chakraborty [68] (also see Owens & Philips for additional insights).

Fattal & Kupferman raised a critical question concerning the loss of resolution of stress gradients developed within fluid elements. They pointed out that inappropriate approximations for the conformation tensor can lead to problems, particularly when conformation terms become exponential at high deformation rates [69]. To address this issue, they introduced the concept of log conformation representation (LCR). LCR involves representing stress in the logarithmic form to prevent negative-valued stress terms and reduce the impact of exponential increases and decreases. LCR has been shown to provide numerical stability at very high Weissenberg numbers, resulting in significantly improved performance compared to classical computational fluid dynamics (CFD). However, it's important to note that while LCR enhances stability, it can introduce accuracy challenges [70]. The LCR application by the finite volume method is applicable in OpenFoam for high Weissenberg numbers, stating the same observations about stability and accuracy [71].

The open-source DNS for viscoelastic fluids can be found in OpenFOAM, named as rheoFOAM, which contains several different models to solve, including log

conformation approaches. This rheotool has been under development for years, and the stability criterion improves over time [72]. Additionally, other commercial software such as Ansys - Polyflow and COMSOL have their own packages for rheological applications.

1.2.2 Reduced Numerical Models

Linearization provides a robust framework for addressing viscoelastic constitutive equations, particularly in scenarios involving constant shear viscosity. The Upper Convected Maxwell (UCM) and Oldroyd-B models are well-suited for this approach. The initial application of linearization (LIN), as based on the Deborah number, was pioneered by Tichy [57]. It was observed that in situations with lower Deborah numbers, such as those involving squeezed thin film flow, a correction factor must be introduced into the fluid field to account for viscoelasticity. Subsequent studies by Li challenged Tichy's linearization scheme, leading to an updated scheme that incorporates geometric expansion for correction [73]. This revised linearization scheme includes corrections to the velocity field, pressure, and conformation stress analytically, with pressure being calculated numerically [74]. The LIN approach is modified by expanding one more term in perturbation for correction at high Weissenberg numbers. This expansion provides quadratic correction compared to previous expansion theories [75, 76], mostly in thin film flows.

Linearization is a valuable tool for studying scenarios with low Deborah and Weissenberg numbers, mitigating the influence of highly nonlinear terms. However, it's crucial to understand the limitations of linearization, particularly in situations with highly nonlinear flow. Additional factors such as the Weissenberg number and contact eccentricity can serve as strong indicators of the nonlinearities present in polymer flow [77]. Therefore, the applicability of linearized models extends beyond polymer relaxation times to include specific characteristics of the contact of interest.

Another approach involves directly calculating pressure by solving the polymeric stress equations individually, accounting for the transient development of stress. This method, known as the Viscoelastic Reynolds (VR) method, is especially relevant in lubrication theory. It requires a coupled system solver for the stress equations. The VR method has been successfully applied in a 2D context and validated against Direct Numerical Simulation (DNS), particularly for low Weissenberg numbers. Interestingly, the 2D direct solver managed to handle instabilities that occurred at high Weissenberg numbers [78]. The VR method demonstrates good agreement with DNS results when using Olroyd-B and FENE models. When VR is compared to the LIN, the different models show alignment at low Weissenberg numbers with low eccentricity [77].

1.3 Cavitation Models

In flows, cavitation occurs when the pressure is not high enough to keep fluids in the liquid state. The fluid forms bubbles during the flow, leading to various natural phenomena like sea foams and man-made machinery such as refrigerator cycles where it depicted in Fig.1.4. In lubrication studies, cavitation plays a crucial role in performance, efficiency, and durability. Particularly in contacts with micro-regularities where most materials exhibit surface roughness, cavitation should be considered in calculations [21]. Additionally, when channels diverge, high-pressure squeezed film areas, pressure drops, and cavitation are likely to occur, unless external pressurized channels are present to prevent bubble formation. In elastohydrodynamic lubrication (EHL) contacts, cavitation is necessary to achieve a positive load.

Vapor bubbles form in the diverging parts of the channel, causing a pressure drop below the saturated pressure. The location of film rupture becomes a critical factor in lubrication problems where cavitation occurs. Initially, the Reynolds or Swift-Stieber

condition was employed to tackle this issue, setting the pressure to a predetermined cavitation pressure in the vapor-liquid mixture.

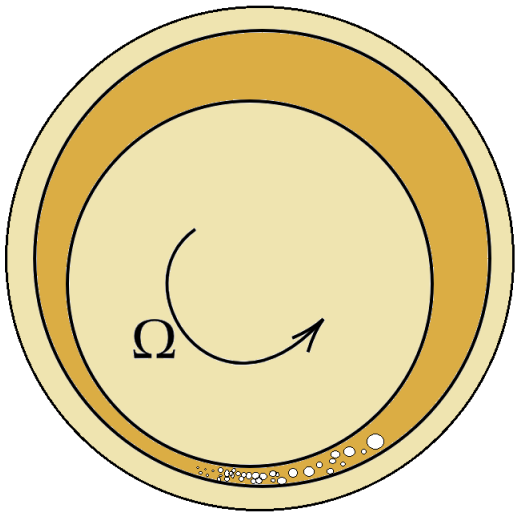

Figure 1.4: A Grapichal representation of cavitation for a journal bearing. Bubble forms after squeezing lubricant expanded. The inner rotor moves with angular speed Ω.

However, this model proves ineffective for film reformation and lacks mass conservation. To address these shortcomings, Jacobson [79] and Olsson [80] developed a mass-conserving model by applying appropriate boundary conditions, known as the Jacobson-Floberg-Olson (JFO) theory. Elrod further enhanced this model by solving a generalized Reynolds equation in conjunction with the JFO theory, introducing a non-linear operator switch function. This refinement led to the $p - \theta$ solution for cavitated lubrication [81].

The Elrod-Adams model, computationally convenient for implementation [82], introduces a density ratio, often denoted as θ, representing the fluid film fraction.

This phase change is depicted by the fluid film fraction, which is the ratio between the liquid portion of the fluid and the bubble portion. The model ensures conservative mass flow rates by accounting for the fluid film fraction in different pressure equations. Further advancements in methods include predicting film rupture, along with providing discretization of the numerical algorithm for unsteady flow problems [83].

Various cavitation algorithms have been developed to address different conditions. Ausas et al. compared the Reynolds condition with the Elrod-Adams model for a channel containing micro-regularities and found that the film can reform in a mass-conserving algorithm after it ruptures once [84]. This algorithm has also been validated for squeezing and dynamical problems. However, its computational speed is relatively slow due to the iterative scheme employed to overcome the nonlinearities introduced by the domain [85].

Giacopini et al. have further refined mass-conserving algorithms for finite element applications by translating thin film equations into a set of linear algebraic equations, thereby increasing time efficiency compared to iterative approaches [86]. Additionally, Woloszynski et al. developed a very fast cavitation algorithm known as the Fischer-Burmeister-Newton-Schur (FBNS) algorithm. This two-step algorithm first constrains the pressure and film fraction using Fischer-Burmeister equations and then manipulates the governing equations represented in matrix form using FB equations [87]. For further discussion on cavitation in soft lubrication scenarios, Allen's work compares several cavitation models in the context of parallel sliding bearings [88].

1.4 Problem Formulation

Our problem investigates the following question: What happens if we introduce polymers into elastically deformable contacts? There is neither an analytical answer to this question nor prior knowledge derived from polymeric melt flows. This is primarily because non-Newtonian polymeric fluid flows are typically studied in conformal surfaces. While numerous studies have been conducted on viscoelastic fluidic flows, the focus on viscoelasticity in soft or hard Elastohydrodynamic Lubrication (EHL) cases has been somewhat neglected. Indeed, there have been extensive studies on piezo-viscous effects and shear thinning in hard EHL cases, but when it comes to soft EHL, the studies are limited.

The approach to solving the problem starts with presenting a general perspective through the mathematical foundation. To gain sufficient knowledge about EHL, elastic contact theory is explored and then shaped towards non-conformal surfaces. Several numerical schemes are discussed, and suitable choices are selected. Then, starting from the Navier-Stokes equations, the Reynolds equation is revisited in terms of Cauchy transport equations. The validity of inserting the extra stress tensor exerted by the polymers in the Cauchy stress term is examined. As a polymeric stress model, the Oldroyd-B constitutive equations are described for polymers. Following the constitutive equation, the dimensionless numbers De and Wi are briefly discussed, considering the problem formulation.

The cavitation conditions are reviewed, and a suitable cavitation algorithm is established. As we are investigating soft lubrication, the pressure is insufficient to generate a compressible effect. Consequently, it may seem that the mass conservation law is quite evident for incompressible flow. However, the implementation of the mass conservation law can result in varied outcomes with different numerical approaches.

The numerical section encompasses the boundary element method. The

constructed elastic deformation kernel is introduced. Although the EHL problem is not solved with VR, for the sake of completeness, two methods—LIN and VR—are introduced for viscoelastic flow. LIN is comparatively simpler regarding VR formulation, but as a future work, VR is preferable for its high accuracy in handling highly nonlinear equations. VR also offers the possibility of selecting other polymer models such as FENE-P or FENE-CR. The general numerical schematic is provided at the end of the numerical section, encapsulating all aspects of the viscoelastic soft lubrication problem.

Following the soft lubrication, simple geomerties,contraction and expansion, are studied to elastic strees more detailly. The result for VR has validated by DNS for relatievly low and moderate Wi numbers. Lastly, primer studies on experiments to measure load increment is summerized. Despite experimental work is not the main deal, this chapter can be assumed as an beginner guide to experimental study and provide valuable references and lab-on-experience.

Chapter 2

Mathematical Model

In this section, we delve into the mathematical models used in the thesis, aiming to provide a comprehensive understanding of viscoelastic fluids in soft lubrication. While the mathematics employed in defining the problem are well-established, this section serves as a synthesis of existing literature and the integration of models to comprehensively grasp the behavior of viscoelastic fluids in soft lubrication scenarios.

We begin with an elementary explanation of linear elastic deformation calculations to lay the groundwork for understanding the deformation of solid surfaces in contact. This is followed by an introduction to the basic principles of the boundary element method, which is commonly used for solving problems involving elastic deformation.

Moving on from linear elasticity, we transition to the fluid description, starting from the micro-structure level and progressing to the continuum scale. The complex concept of the upper-convected time derivative is described in detail, as it forms the foundation of the Oldroyd-B model, which is a commonly used constitutive model for viscoelastic fluids.

The derivation of the constitutive Oldroyd-B model via kinetic theory is briefly outlined, providing insight into how the model captures the behavior of viscoelastic fluids. With the stress tensor constructed to account for the presence of polymers, we proceed to formulate the two-dimensional fluid momentum equations, which govern the behavior of the viscoelastic fluid in soft lubrication scenarios.

The thin film approximation has been applied to both the mass conservation and momentum equations to derive the Reynolds Equation, which governs the flow of the lubricant film. Additionally, the effects of polymeric stress have been incorporated into the formulation to account for the viscoelastic behavior of the fluid.

Reduced models for solving the thin film equations are then provided, taking into account additional necessary formulations for load and friction. These formulations are essential for evaluating the performance of lubrication systems, providing insights into factors such as film thickness, pressure distribution, and frictional forces within the contact interface.

2.1 Elastic Deformation

In that case, the displacement is given in the contact surface function as given in Fig.4.9 along with minimum height, h_o, and a predetermined surface function, $S(x)$.

In the subsequent sections, elastic deformation theory will be introduced for lubricated contacts. However, before delving into this, it is crucial to examine the underlying equations that explain contact mechanics. This exploration begins with Hertz, who emphasized the importance of determining the maximum pressure that a solid can endure [31]. He provided insights into calculating this pressure, which laid the foundation for understanding contact mechanics.

The concept of the elastic half-space and the maximum pressure between two bodies, often referred to as the Hertzian half-space and Hertzian pressure, respectively, were named after him. Various formulations exist for calculating these parameters for different types of contacts, such as point, line, and elliptic contacts. For the purposes of this thesis, lubricated contacts are assumed to be in contact with each other as line elements.

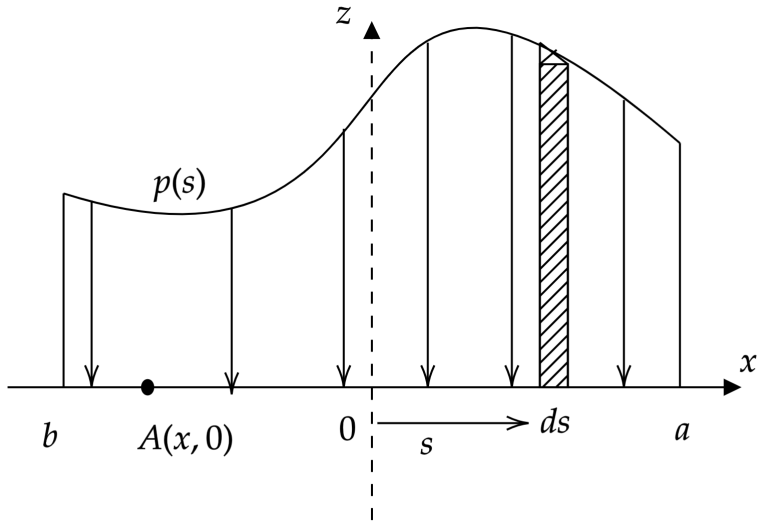

Figure 2.1: A pressure distribution on a surface

In lubricated contacts, the developed pressure is typically larger in orders of magnitude compared to tangential forces. As a result, tangential forces are often negligible. Consider a strip loaded with just a pressure distribution, as illustrated in Fig.2.1, and let's seek the displacement at point A in the body. The displacement can be expressed in its most general form [32]:

$$\bar{u}_z = \frac{2(1-\nu^2)}{\pi E} \int_{-b}^{a} p(s) ln|x-s| ds \tag{2.1}$$

Indeed, this equation represents a convolution integral of pressure along the surface for calculating the displacement at point A A. Essentially, it signifies that the point at A, experiences the least pressure from the farthest points. By constructing an integral for each point on the surface, one can determine the overall displacement field. This integral approach is fundamental for understanding the distribution of pressure-induced deformations in lubricated contacts.

It is possible to recognize the displacement equation in the other EHL cases when we regard the lubricated contacts. Another common presentation of displacement is:

$$\bar{u}_z = \frac{2}{\pi E'} \int_{-b}^{a} p(s) ln|x-s|^2 ds \tag{2.2}$$

where this case takes two surfaces deformation together, thus letting a square term at the logarithmic term. In this case, effective elastic modules need to be calculated. It is given for two bodies:

$$\frac{1}{E'} = \frac{1}{2}\left(\frac{1-\nu_t^2}{E_t} + \frac{1-\nu_b^2}{E_b}\right) \tag{2.3}$$

Another important parameter to depict the contact is the effective radius of curvature defined as:

$$\frac{1}{R'} = \frac{1}{R_t} + \frac{1}{R_b} \tag{2.4}$$

where subscripts denote the bottom and top surfaces. After obtaining these parameters, Hertzian line contact properties for semi-width and maximum pressure can be easily calculated by the stated equations given in Johnson:

$$b_H^2 = \frac{4W_o R'}{\pi E'} \tag{2.5a}$$

$$p_H = \frac{2W_o}{\pi b_H} \tag{2.5b}$$

Defining the Hertzian semi-width is essential for comprehending the scaling of the contact. Typically, it is utilized to non-dimensionalize the horizontal length. It's important to note that the semi-width varies with changes in the applied load since the contact length is assumed to be conformal. The Hertzian maximum pressure is then used to scale the generated pressure. However, in lubricated contacts, this pressure should be less than 1, as direct contact between the surfaces is prevented. This highlights the significance of proper scaling in lubrication studies, especially when considering the impact of pressure on the contacting surfaces.

While Finite Element Method (FEM) approaches are indeed common for solving equations like Eq.2.1, analytical solutions are often feasible for such integral equations. Analytical methods provide precise solutions without the computational overhead associated with numerical techniques. One common approach involves creating a uniform mesh and forming an influence coefficient matrix, a method extensively discussed in literature such as [15]. However, for this thesis, we adopt the Boundary Element Method (BEM) for numerical solution of the displacement equation. The BEM requires different formulations compared to FEM, offering its own advantages and considerations for solving boundary value problems efficiently.

2.1.1 Boundary Element Method

The Navier equation of elasticity for 2D problem for restrained plain strain problem can be formulated as [89]:

$$\nabla^2 \boldsymbol{u} + \frac{1}{(1-2\nu)} \nabla(\nabla \cdot \boldsymbol{u}) = 0 \tag{2.6}$$

where $\boldsymbol{u}$ is the elastic displacement vector field. The problem can be reduced to the Fredholm equation of the first kind, which can be solved with numerical procedures. The more detailed reduction from the Eq.2.6 to the Fredholm integral equation can be found in Carbone & Mangialardi [90]. This set in linear elasticity displacement field at the interface can be expressed in normal stress in 1D form [90, 91]:

$$u_z = \int_{\mathcal{L}} G(\boldsymbol{x} - \boldsymbol{s}) \sigma(\boldsymbol{s}) ds \quad \boldsymbol{x} \in \boldsymbol{\mathcal{L}} \tag{2.7}$$

where $G(\boldsymbol{x})$ is the Green function. The Eq.2.7 is translated to the linear set of equations by Fourier Transform given as:

$$u_z(q) = G(q)\sigma(q) \tag{2.8}$$

The rest of the derivation is followed by ref [92]. The Fouirer tronsformed spatial Green function, $G(q) = 2(1-\nu^2)S(q)/Eq$ with $S(q)$ is the correction factor which $S(q) = 1$ for half-plane. In the context of contact mechanics, it is usual to have a periodic interface such as a sinusoidal interfaces. In order to account for this, the Green function is represented by the wavelength of the periodicity. However, in this study, the interface is not periodic but complete. Still, the wavelength, Λ is kept in the equations. Periodic Green function $G_\Lambda(q) = G(q)\chi_\Lambda(q)$ is defined by the periodic pressure distribution χ_Λ and specifically given as [92]:

$$\chi_\Lambda(q) = \sum_{k=-\infty}^{+\infty} \frac{2sin(\frac{1}{2}kq_0a)}{kq_0} \delta(\frac{q}{q_0} - k) \tag{2.9}$$

where the wavevector equals $q_0 = 2\pi/\Lambda$ (for non-periodic surfaces $\Lambda = \mathcal{L}$ can be assumed). Now, we can take the inverse Fourier transform of the Green function, $G_\Lambda(q)$ by IFTT effectively. Lastly by inverse transform:

$$G_\Lambda(x) = \frac{q_0}{2\pi} \sum_{k=-\infty}^{+\infty} G(kq_0) \frac{2sin(\frac{1}{2}kq_0a)}{kq_0} e^{ikq_0x} \tag{2.10}$$

By obtaining Eq.2.10 we can have a solution for Eq. 2.7. The numerical procedure for solving is given in Sec.3.1. The displacement is then integrated with the height of the channel straightforwardly.

2.2 Reynolds Equation

In this section, we delve into the derivation of the Reynolds equation, considering the constitutive equation for polymeric stress. Since our primary focus is on understanding the impact of polymers on viscoelasticity in the flow, a substantial portion is dedicated to unraveling the underlying mathematics of polymers. Once we have obtained the constitutive equation, we integrate it with the Navier-Stokes equations and apply thin film approximation techniques to derive the Reynolds equation. Additionally, a separate subsection is allocated to discussing cavitation and its implementation across different models, highlighting its significance in lubrication dynamics. This comprehensive treatment ensures a thorough understanding of the mathematical framework underpinning the behavior of viscoelastic fluids in lubricated contacts, incorporating both polymeric effects and cavitation phenomena.

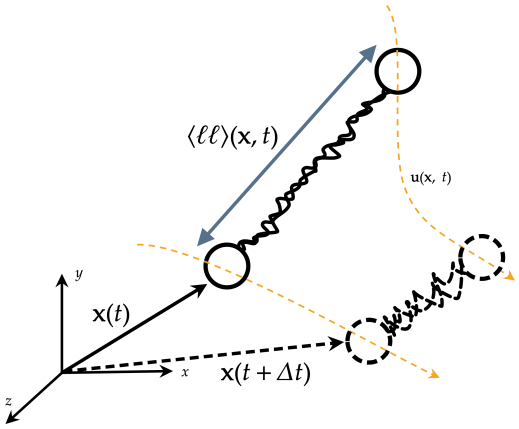

Figure 2.2: An elastic dumbbell model in a flow

2.2.1 Upper Convected Time Derivative

The choice of the Oldroyd-B constitutive equation is pivotal for elucidating the behavior of the complex fluid, as discussed in the introduction section. This model, akin to the upper convected Maxwell model, captures the microscopic dynamics of polymers through the representation of elastic dumbbells. These dumbbells undergo advection and stretching by the flow, exhibiting a linear restoring force due to the polymer structure, as illustrated in Fig.2.2. Unlike the Maxwell model, the Oldroyd-B formulation incorporates a retardation time, representing finite viscosity for the solvent [55].

The cornerstone of describing polymeric behavior during flow in Oldroyd-B equations lies in the upper convected time derivative, a powerful mathematical construct that accounts for both elastic and viscous contributions in a fluid medium. A deeper understanding of this derivative can be gained by examining the Lagrangian description of fluid particles, which sheds light on its invariances associated with vectorial and tensorial quantities. Further insights into the convected time derivatives in complex flows can be gleaned from the work of Stone et al., which

provides a comprehensive summary [93]. Additionally, Morozov & Spagnolie offer a continuum description for frame-variant systems, elucidating the coordinate frame transformation and its implications for covariant derivation [52].

In the Eulerian framework, the velocity field, $\boldsymbol{u}(\boldsymbol{x}, t)$ is defined for a position $\boldsymbol{x}$ and time t. The Eulerian frame is associated with the Lagrangian framework via a material derivative which is defined as:

$$\frac{D}{Dt} = \frac{\partial}{\partial t} + \boldsymbol{u} \cdot \nabla \tag{2.11}$$

So, for a fixed coordinate system, the total (material) time derivative connects the velocity field with the quantity of interest. In the Lagrangian setting, the rate of changing of a line segment $\boldsymbol{\ell}$, is expressed by material derivative in ref [94].

$$\frac{D\boldsymbol{\ell}}{Dt} = \boldsymbol{\ell} \cdot \nabla \boldsymbol{u} \tag{2.12}$$

where the line elements are transported by the flow field. Surprisingly, this material derivative differs, from the earlier definitions. In this case, one might think that the end-to-end segment is translated in time by the flow and hence it time rate of change in the Lagrangian setup is defined similarly to linear solid deformations described below.

The motion is told by Lagrangian trajectories, $\boldsymbol{x} = \boldsymbol{x}(t; \boldsymbol{X})$ where $\boldsymbol{x} = (0; \boldsymbol{X}) = \boldsymbol{X}$, the capital $\boldsymbol{X}$ is the initial position of the trajectory. The differential $\boldsymbol{X}$ is mapped to the displacement with

$$d\boldsymbol{x} = d\boldsymbol{X} \cdot \boldsymbol{F} \tag{2.13}$$

where $\boldsymbol{F}(t;\boldsymbol{X})$ is the deformation gradient tensor, $F_{ij} = \frac{\partial x_j}{\partial X_i}$ as represented in index notation. We might relate the deformation gradient tensor with the flow gradient showed in Eq.2.12 to gain more understanding of the definition.

Now, think of a conformation tensor $\boldsymbol{A}$ being vector $\boldsymbol{r}$ with equilibrium length r_{eq}, dyadic product. With its non-dimensional form, conformation tensor is, $\boldsymbol{A} = \langle \boldsymbol{rr} \rangle / r_{eq}^2 = \langle \boldsymbol{\ell\ell} \rangle$ where $\langle . \rangle$ is the ensemble average and dyadic product $\langle \boldsymbol{\ell\ell} \rangle$ characterizes *the state of deformation of a given microstructure* [93] might be shown in Fig.2.2. Ensemble average notation is dropped for simplicity. Take the material derivative of the conformation tensor with the product rule:

$$\frac{d\boldsymbol{A}}{dt} = \frac{d(\boldsymbol{\ell\ell})}{dt} = \frac{d(\boldsymbol{\ell})}{dt}\boldsymbol{\ell} + \boldsymbol{\ell}\frac{d(\boldsymbol{\ell})}{dt} \tag{2.14}$$

We can utilize the Eq.2.12 and proceed the derivative as:

$$\frac{D\boldsymbol{A}}{Dt} = \boldsymbol{\ell} \cdot \nabla \boldsymbol{u}\boldsymbol{\ell} + \boldsymbol{\ell\ell} \cdot \nabla \boldsymbol{u} \tag{2.15}$$

The first term at the right-hand side can be modified by tensor properties and the following expression is obtained:

$$\frac{D\boldsymbol{A}}{Dt} = \nabla \boldsymbol{u}^T \cdot \boldsymbol{\ell\ell} + \boldsymbol{\ell\ell} \cdot \nabla \boldsymbol{u} = \nabla \boldsymbol{u}^T \cdot \boldsymbol{A} + \boldsymbol{A} \cdot \nabla \boldsymbol{u} \tag{2.16}$$

A time derivative *for the change of the tensor (dyadic product) deforming in a fluid flow* is introduced:

$$\overset{\nabla}{\boldsymbol{A}} \overset{\text{def}}{=} \frac{D\boldsymbol{A}}{Dt} - \nabla \boldsymbol{u}^T \cdot \boldsymbol{A} + \boldsymbol{A} \cdot \nabla \boldsymbol{u} \tag{2.17}$$

The derivative $\overset{\nabla}{\boldsymbol{A}}$ is known as the upper convicted time derivative as it is mentioned in the introduction. If time derivative $\overset{\nabla}{\boldsymbol{A}}= 0$ by definition it is straightforward to conclude that the conformation tensors deform exactly as the line segments in the flow. However, if $\overset{\nabla}{\boldsymbol{A}}\neq 0$, the conformation tensor rate of change is not equal to the line elements deformation.

Indeed, the non-zero nature of the upper convective time derivative may seem perplexing at first glance. However, it can be understood by considering the disparity between the time scaling of the material derivative and the rate of change of the conformation tensor. This difference reflects variations in the microstructure of the fluid over time, particularly influenced by the viscoelastic properties and restoring forces inherent in polymeric structures. Consequently, we can infer that the time derivative is intricately linked to the relaxation time of polymers, highlighting the dynamic interplay between fluid behavior and polymer characteristics.

The relationship between conformation tensor and the constitutive equation has not presented in this thesis. In below section, the constitutive equation has derived by kinetic theory and conformation tensor has avoided. However, Snoeijer et. al. review the viscoelasticity and its relationship with elasticity [95].

2.2.2 Constitutive Relationship

The constitutive equation root for Oldroyd-B goes deep into the molecular dynamics of the polymeric substance. The same figure for expressing upper-convected time derivative can be used for explaining the constitutive relationship. The derivation is rough in terms of deep causation between the particle dynamics to continuum scale relationship. Those who want to get a comprehensive outlook for the equations should visit Owens & Philips, and more specifically Bird and Warner for molecular understanding of the underlying physics. For a specific interest in Oldroyd-B,

"Oldroyd B, and not A?" article by Hinch & Harlen profound the derivation with full historical context [96]. For continuum description further readings are available including constituvie relationships [97].

The beads in the dumbbell model pull and push each other with a connected Hookean spring. Thus, the force exerted by the spring to hold the beads together where beads' end-to-end distance is ℓ as discussed before in Sec.2.2.1. The full three-dimensional space distance average is shown by $\langle \boldsymbol{\ell\ell} \rangle$. After the brief introduction, we can state the extra stress tensor given for the solvent-polymer mixture as a result of the ensemble average of Hookean spring:

$$\boldsymbol{T} = -nkT\boldsymbol{I} + \eta_s \dot{\boldsymbol{\gamma}} + nH\langle \boldsymbol{\ell\ell} f(\ell) \rangle \tag{2.18}$$

This expression of stress is known as *Krammer's expression* of the stress. This equation contains a number of dumbells shown as n. The first term, accounts for the Brownian motion of the bead, given that k is for Boltman constant and T for temperature. The second term is solvent viscosity with the deformation rate of the solvent fluid motion. Lastly, the ensemble-averaged space by a factor of a special function f multiplied by the elasticity of the spring H. The derivation can be found in Bird [98] and Larson [53].

The upper convected time derivative defined in the previous section, equals:

$$\frac{D\langle \boldsymbol{\ell\ell} \rangle}{Dt} - \nabla \boldsymbol{u}^T \cdot \langle \boldsymbol{\ell\ell} \rangle + \langle \boldsymbol{\ell\ell} \rangle \cdot \nabla \boldsymbol{u} = \frac{4kT}{\zeta}\boldsymbol{I} - \frac{1}{\lambda_1}\langle \boldsymbol{\ell\ell} f(\ell) \rangle \tag{2.19}$$

where this equation is obtained by the space integral of *the Fokker-Plankl equation.* Unknown term ζ is the friction coefficient of the dumbbell bead and solvent fluid interaction, equals $\zeta = 6\pi\eta_s a$ where a is the radius of the bead. Secondly, a relaxation

time λ_1 is introduced by this equation which equals to $\lambda_1 = \zeta/4H$. Insert the Eq.2.19 in Kramers expression Eq.2.18 and get *Giesekus expresison* for stress tensor:

$$\boldsymbol{T} = \eta_s \dot{\boldsymbol{\gamma}} + \frac{n\zeta}{4} \overset{\nabla}{\langle \boldsymbol{\ell}\boldsymbol{\ell} \rangle} \tag{2.20}$$

Oldroyd-B model assumes the spring obeys the Hookean spring law, leading to $f(\ell) = 1$ seen in Kramer's expression. For FENE models $f(\ell) \neq 1$, preventing infinite extensibility of the spring. We can combine Kramers expression (Eq.2.18) and Giesekus expression (Eq.2.20) by taking the upper convected time derivative of Eq.2.18. Observe that, the Idendity tensor derivative is:

$$\overset{\nabla}{\boldsymbol{I}} = -\nabla \boldsymbol{u} - (\nabla \boldsymbol{u})^T = -\dot{\boldsymbol{\gamma}} \tag{2.21}$$

Eliminate $\overset{\nabla}{\langle \boldsymbol{\ell}\boldsymbol{\ell} \rangle}$ terms by rearranging equations, we obtain:

$$\boldsymbol{T} - \eta_s \dot{\boldsymbol{\gamma}} = -\frac{\zeta}{4H} \left[\overset{\nabla}{\boldsymbol{T}} - nkT\dot{\boldsymbol{\gamma}} - \eta_s \overset{\nabla}{\dot{\boldsymbol{\gamma}}} \right] \tag{2.22}$$

It is a good point to define polymeric viscosity, η_p and characteristics fluid retardation time, λ_2. They can be defined by appearing parameters in Eq.2.22.

$$\eta_p = \frac{nkT\zeta}{4H} \quad \text{and} \quad \lambda_2 = \frac{\eta_s \zeta}{4(\eta_p + \eta_s)H} = \frac{\eta_s \lambda_1}{4(\eta_p + \eta_s)}$$

Insert them in Eq.2.22 and get Oldroyd-B constitutive equation:

$$\boldsymbol{T} + \lambda_1 \overset{\nabla}{\boldsymbol{T}} = \eta_0 \left(\dot{\boldsymbol{\gamma}} + \lambda_2 \overset{\nabla}{\dot{\boldsymbol{\gamma}}} \right) \tag{2.23}$$

where $\eta_0 = \eta_p + \eta_s$ sum of polymeric and solvent viscosity, being the total viscosity of the fluid. One can separate the solvent extra stress by stating extra stress term with, $\boldsymbol{T} = \eta_s \dot{\boldsymbol{\gamma}} + \boldsymbol{\tau}$, where $\boldsymbol{\tau}$ is the elastic stress term. Substitute in Eq.2.23

$$\boldsymbol{\tau} + \lambda_1 \overset{\nabla}{\boldsymbol{\tau}} = \eta_p \dot{\boldsymbol{\gamma}} \tag{2.24}$$

As is mentioned in the introduction, UCM is strongly related to the Oldroyd-B equation, subsequently if $\eta_s \to 0$, UCM can be obtained, where elastic stress equals to stress tensor ($\boldsymbol{T} = \boldsymbol{\tau}$).

2.2.3 Thin Film Approximation

We can start to derive the Reynolds equation from Naiver-Stokes equations for incompressible and isoviscous flow. The body force of the fluid is also neglected. Then, the mass balance is

$$\nabla^* \cdot \boldsymbol{u^*} = 0 \tag{2.25}$$

Force balance equation

$$\rho \frac{D\boldsymbol{u^*}}{Dt^*} = \nabla^* \cdot \boldsymbol{\sigma^*} \tag{2.26}$$

where $\boldsymbol{u^*}$ is velocity vector and $\boldsymbol{\sigma^*}$ is the stress tensor. Stress tensor is represented in close form in 2.26 as it can include several different stress components. We define stress in the most general form

$$\boldsymbol{\sigma}^* = -p^* \boldsymbol{I} + \boldsymbol{T}^* \tag{2.27}$$

where p^* is the pressure of the fluid and $\boldsymbol{T}^*$ is the stress tensor we are familiar with from the previous section. Use same expension for stress, $\boldsymbol{T}^* = \eta_s \dot{\boldsymbol{\gamma}}^* + \boldsymbol{\tau}^*$, seperate solvent shear rate and elastic stress. Replace to Eq.2.27

$$\boldsymbol{\sigma}^* = -p^* \boldsymbol{I} + \eta_s \dot{\boldsymbol{\gamma}}^* + \boldsymbol{\tau}^* \tag{2.28}$$

By using Oldroyd-B relationship given in Eq.2.24 we can expand elastic stress $\boldsymbol{\tau}$ and get:

$$\boldsymbol{\sigma}^* = -p^* \boldsymbol{I} + \eta_0 \dot{\boldsymbol{\gamma}}^* - \lambda_1 \overset{\nabla}{\boldsymbol{\tau}^*} \tag{2.29}$$

In Eq.2.29, we combine solvent viscosity and polymer viscosity with $\eta_0 = \eta_s + \eta_p$, equals total viscosity of the fluid mixture, concluding a regular Newtonian stress which familiar to any Newtonian fluid. Realize that, one portion of polymeric stress depends on the shear rate of deformation whereas the other portion is the upper convected time derivative scaled with relaxation time. We drop one appearing at subscript of λ afterwards. Expanding the convected time derivative we obtain the surface stress of the fluid element.

$$\boldsymbol{\sigma} = -p^* \boldsymbol{I} + \eta_0 \dot{\boldsymbol{\gamma}}^* - \lambda \left(\frac{\partial \boldsymbol{\tau}^*}{\partial t^*} + (\boldsymbol{u}^* \cdot \nabla^*) \boldsymbol{\tau}^* - \boldsymbol{\tau}^* \nabla^* \boldsymbol{u}^* - \nabla^* (\boldsymbol{u}^*)^T \boldsymbol{\tau}^* \right) \tag{2.30}$$

Though, we have extra viscoelastic stress contribution, which is the non-Newtonian part of the fluid. Using Eq.2.26 and Eq.2.30 we have an alternative form of the momentum balance equation:

$$\rho\left(\frac{\partial \boldsymbol{u}^*}{\partial t^*} + \boldsymbol{u}^* \cdot \nabla^* \boldsymbol{u}^*\right) = -\nabla p^* + \eta_0 (\nabla^*)^2 \boldsymbol{u}^* - \lambda \nabla^* \cdot \left(\frac{\partial \boldsymbol{\tau}^*}{\partial t^*} + (\boldsymbol{u}^* \cdot \nabla^*)\boldsymbol{\tau}^* - \boldsymbol{\tau}^* \nabla^* \boldsymbol{u}^* - (\nabla \boldsymbol{u}^*)^T \boldsymbol{\tau}^*\right) \tag{2.31}$$

Until this point, each variable is used in its dimensional form. We introduce non-dimensional parameters to perform thin film simplification [30]. Thus non-dimensional parameters help to run scaling analyses of the variables. The main scaling parameter is ϵ which is the height over the length of the channel. If $\epsilon << 1$, it means that the film is thin and the main flow is along the channel direction. The parameters are given an accounting for the fact that ϵ is small:

$$\begin{array}{ccc} x = \frac{x^*}{L}, & y = \frac{y^*}{h_{max}}, & u = \frac{u^*}{U_o}, \\ v = \frac{v^*}{\epsilon U_o}, & \epsilon = \frac{h_{max}}{L}, & t = t^* \frac{U}{h_{max}}, \\ \tau_{xx} = \tau^*_{xx} \frac{h^2_{max}}{(\eta_s+\eta_p)U_o L}, & \tau_{xy} = \tau^*_{xy} \frac{h_{max}}{(\eta_s+\eta_p)U}, & De = \lambda \frac{U_o}{L} \\ \tau_{yy} = \tau^*_{yy} \frac{L}{(\eta_s+\eta_p)U_o}, & p = (p^* - p_0) \frac{h^2_{max}}{(\eta_s+\eta_p)UL}, & h = \frac{h^*}{h_{max}} \end{array}$$

where U_o is the reference velocity, h_{max} is the maximum height of the channel, L is the length of the channel. De is Deborah number responsible for the relaxation time of the polymer. A more detailed discussion of De is given later. Note that the viscosity ratio is defined to represent a mixture of solvent and polymer liquid, $\beta = \eta_s/(\eta_p + \eta_s)$. Thus, $\beta = 1$ means the mixture is fully solvent and $\beta = 0$ means the mixture is fully polymer. After substituting non-dimensional parameters into Eq.2.31, Eq.2.25 and Eq.2.24, one can eliminate $O(\epsilon^2)$ and higher terms in appearing equations. Subsequently, the classic Reynolds equation with the polymeric stress is obtained:

$$\frac{\partial u}{\partial x} + \frac{\partial v}{\partial y} = 0 \tag{2.32a}$$

$$\frac{\partial p}{\partial x} = \beta \frac{\partial^2 u}{\partial y^2} + \frac{\partial \tau_{xy}}{\partial y} + \frac{\partial \tau_{xx}}{\partial x} \tag{2.32b}$$

$$\frac{\partial p}{\partial y} = 0 \tag{2.32c}$$

$$\tau_{xx} + De \left(\frac{D\tau_{xx}}{Dt} - 2\tau_{xy} \frac{\partial u}{\partial y} - 2\tau_{xx} \frac{\partial u}{\partial x} \right) = 0 \tag{2.32d}$$

$$\tau_{xy} + De \left(\frac{D\tau_{xy}}{Dt} - \tau_{yy} \frac{\partial u}{\partial y} - \tau_{xx} \frac{\partial v}{\partial x} \right) = (1-\beta) \frac{\partial u}{\partial y} \tag{2.32e}$$

$$\tau_{yy} + De \left(\frac{D\tau_{yy}}{Dt} - 2\tau_{xy} \frac{\partial v}{\partial x} - 2\tau_{yy} \frac{\partial v}{\partial y} \right) = 2(1-\beta) \frac{\partial v}{\partial y} \tag{2.32f}$$

A very crucial outcome is that pressure is independent of the y axis, providing adequate formulation for the rest of the calculation including the velocity field and stress field. But, this set of equations is also to adhere because of coupling and non-linearity. One should solve both pressure, a velocity field and a stress field at the same time. The following section discusses how to handle viscoelastic stress before introducing the models. The discussion includes the reasoning behind building necessary tools to deal with viscoelasticity.

2.3 Viscoelastic Nondimensional Numbers

Viscoelasticity is described by two non-dimensional numbers as introduced in the introduction. Deborah number is the measure of the transient effects shown by the polymers in the flow. Larger De means the fluid extension and relaxation is comparable to flow time. The time scale of the fluid flow, in a channel flow L/U_o, is the required time for passing the channel. The ratio between the relaxation time of the polymer, λ, and the time scale is defined as Deborah number.

On the other hand, the Weissenberg number is the measure of the non-linear shearing effects created by the polymers. The general shear rate of the channel is expressed as U_o/h. When the shear rate is multiplied by the polymer's relaxation time, the Weissenberg number is obtained. However, the shear rate changes depending on where the h is located. Thus, it leads to defining localized Wiesssenberg number, $\tilde{Wi} = \lambda U_o/h_o$ to measure Wi at center [68].

Pipkin space is a term to describe a rheological map of fluid motion. Pipkin space is a way to show if the non-Newtonian effects are caused by the fluid non-linearities or linear viscoelastic effects [99]. Thus a comparison between Wi number and De number points out the non-Newtonian fluid behaviour. In this context, the numbers are not related to each other except for the relaxation time. In lubricated contacts, Ahmed & Biancofiore used the geometrical property, $\epsilon = h_{max}/L$ to relate two numbers to each other by $De = \epsilon Wi$. To use localized $\tilde{Wi}$, define a new center epsilon, $\epsilon_o = h(x = 0)/L$ and similar relationship is conserved.

The eccentricity of the contact is described as the surface curvature of the top surface while the bottom surface remains flat. The surface curvature is crucial for lubrication regimes as it controls the location of maximum pressure. If the contact point approaches more singular, we can say that eccentricity is large and lubrication occurs in a smaller area. Pressure develops from the entrance of the channel but the main contribution occurs at the narrowest section. This leads to very strong numerical instability for non-linear terms appearing in non-Newtonian contributions of polymers. In another sense, the second derivative of the height is crucial for polymeric elastic stress. Especially, normal stress which is non-available for Newtonian fluids, non-linearities may be very large [99] and tackling to handle at high eccentricity. EHL contacts, by definition, are regarded with high eccentricity and the top surface is usually very close to the bottom surface. Noting that particular interest is necessary while dealing with non-Newtonian fluids at high eccentricity contacts.

Linearization is a common technique in fluid mechanics usually used for instability cases. A perturbation of variables $\{\boldsymbol{u}, p, \boldsymbol{\tau}\}$ in terms of Deborah to eliminate non-linear terms depending on polymers relaxation time, provides a good estimation in low Deborah numbers and decouples constitutive equations (Eq.2.32a, 2.32f). It reduces the problem linear set of equations which can be separated into two parts. The unperturbed (Newtonian) solution for the variables remains exactly the same for the well-known Reynolds equation. The perturbed solution remains separate from the Newtonin variable set but it can vary by De number linearly. The quadratic terms, De^2, which may account for non-linear normal stress can be approximated as zero for small De. Thus, linearization, should into account, the magnitude of studied De.

On the other hand, one should not forget that Wi is also a strong indicator of the nonlinear elastic terms. Remember that, localized Wi is a must be defined for capturing proper shear rate time scale, especially for high eccentricity. Thin film parameter ϵ is defined by the maximum height of the channel but for a narrow section of the channel, ϵ_o is preferred, which in case of high eccentricity, can reduce ϵ in the order of $O(10^2)$. Thus, for the same transient effect (constant De), the magnitude of non-linear stress (variable Wi) can increase immensely at the maximum pressure location. Linearization suffers accuracy from the fact that high Wi is evidence of high polymeric stress even if, De is small and constant.

Direct numerical solution of the non-linear equations (Eq.2.32a, 2.32f) suffers from instability for high Wi as it is mentioned in the introduction. However, a reduced model can deal with this instability shown by Ahmed & Biancofiore even in large Wi. Viscoelastic Reynolds has a strong assumption for the velocity field to overcome the coupled equations. If the velocity field is a negligible function of the De number, the velocity field can be assumed to be corrected by the first-order linearization. Thus, we are able to solve transiently coupled stress equations (Eq.2.32d, 2.32f) and obtain stress to calculate pressure easily.

The advantage of using a reduced model over DNS is the power of separating the velocity field and stress field. After knowing the velocity field, the only issue is the 2D coupled transient PDE that needs to be solved. Subsequently, initial conditions for stress are estimated by the linearization, assuring faster convergence. However, VR also suffers from HWNP even if it is able to predict pressure accurately for a very large Wi numbers.

2.4 Thin Film Lubrication Models

In this section, two models are examined to address non-Newtonian stress. The first model is the linearized Reynolds model (LIN) which has been known for 20 years. The latter is the Viscoelastic Reynolds model (VR) which is recently developed.

Before starting the derivation of models, let's introduce the density variable for cavitation. When the flow is squeezed, the pressure is generated but while the flow leaving the channel, the pressure drops immediately and forms bubbles. This point is called as film rupture, its location is unknown before solving the problem. It is assumed that throughout the channel there is a vapor-liquid mixture with a specific ratio. Regarding this, Elrod [81], introduced fluid film fraction variable, θ. This is defined as:

$$\theta = \frac{\rho}{\rho_l} \tag{2.33}$$

where ρ is variable density and ρ_l is liquid density at full film. So, during full film $\theta = 1$ and at vapor-liquid mixture $0 < \theta < 1$. Regarding θ variable and running non-dimensional scaling, the mass flow rate turns into:

$$\frac{\partial(\theta)}{\partial t} + \frac{\partial(u\theta)}{\partial x} + \frac{\partial(v\theta)}{\partial y} = 0 \tag{2.34}$$

where the remaining equations stay exactly the same. If there is relative motion between two surfaces, the time derivative vanishes. The same procedure is applicable also in VR. However, VR is first introduced without the θ term.

2.4.1 Linearized Reynolds Model

The linearized solution starts with perturbation analyses of variables in terms of Deborah number to describe polymeric contributions to velocity, pressure, fluid film fraction and stress. The following terms are the correction factors for the leading order solution.

$$\boldsymbol{u} = \boldsymbol{u}^{(0)} + De\,\boldsymbol{u}^{(1)} + De^2\,\boldsymbol{u}^{(2)} + O(De^3), \tag{2.35a}$$

$$p = p^{(0)} + De\,p^{(1)} + De^2\,p^{(2)} + O(De^3), \tag{2.35b}$$

$$\theta = \theta^{(0)} + De\,\theta^{(1)} + De^2\,\theta^{(2)} + O(De^3), \tag{2.35c}$$

$$\boldsymbol{\tau} = \boldsymbol{\tau}^{(0)} + De\,\boldsymbol{\tau}^{(1)} + De^2\,\boldsymbol{\tau}^{(2)} + O(De^3), \tag{2.35d}$$

If $De << 1$ the second-order terms can be neglected and just first-order terms are required for correction [57]. Note that, first-order stress means regular surface stress occurring in the fluid. Substituting equations 2.35a-2.35d into the equations 2.32a-2.32f, we can collect zero order and first order terms separately by eliminating $O(De^2)$ and higher order terms:

$$\frac{\partial(\theta^{(0)}u^{(0)})}{\partial x} + \frac{\partial(\theta^{(0)}v^{(0)})}{\partial y} = 0, \tag{2.36a}$$

$$\frac{\partial p^{(0)}}{\partial x} = \beta\frac{\partial^2 u^{(0)}}{\partial y^2} + \frac{\partial \tau_{xy}^{(0)}}{\partial y} + \frac{\partial \tau_{xx}^{(0)}}{\partial x}, \tag{2.36b}$$

$$\frac{\partial p^{(0)}}{\partial y} = 0, \tag{2.36c}$$

$$\tau_{xx}^{(0)} = 0, \tag{2.36d}$$

$$\tau_{xy}^{(0)} = (1-\beta)\frac{\partial u^{(0)}}{\partial y}, \tag{2.36e}$$

$$\tau_{yy}^{(0)} = 2(1-\beta)\frac{\partial v^{(0)}}{\partial y}. \tag{2.36f}$$

The first-order terms are collected:

$$\frac{\partial}{\partial x}(\theta^{(0)}u^{(1)} + \theta^{(1)}u^{(0)}) + \frac{\partial}{\partial y}(\theta^{(0)}v^{(1)} + \theta^{(1)}v^{(0)}) = 0, \tag{2.37a}$$

$$\frac{\partial p^{(1)}}{\partial x} = \beta\frac{\partial^2 u^{(1)}}{\partial y^2} + \frac{\partial \tau_{xy}^{(1)}}{\partial y} + \frac{\partial \tau_{xx}^{(1)}}{\partial x}, \tag{2.37b}$$

$$\frac{\partial p^{(1)}}{\partial y} = 0, \tag{2.37c}$$

$$\tau_{xx}^{(1)} = 2\tau_{xy}^{(0)}\frac{\partial u^{(0)}}{\partial y}, \tag{2.37d}$$

$$\tau_{xy}^{(1)} = -\left(u^{(0)}\frac{\partial \tau_{xy}^{(0)}}{\partial x} + v^{(0)}\frac{\partial \tau_{xy}^{(0)}}{\partial y} - \tau_{yy}^{(0)}\frac{\partial u^{(0)}}{\partial y}\right) + (1-\beta)\frac{\partial u^{(1)}}{\partial y}, \tag{2.37e}$$

$$\tau_{yy}^{(1)} = -\left(u^{(0)}\frac{\partial \tau_{yy}^{(0)}}{\partial x} + v^{(0)}\frac{\partial \tau_{yy}^{(0)}}{\partial y} - 2\tau_{xy}^{(0)}\frac{\partial v^{(0)}}{\partial x} - 2\tau_{yy}^{(0)}\frac{\partial v^{(0)}}{\partial y}\right) + 2(1-\beta)\frac{\partial v^{(1)}}{\partial y}, \tag{2.37f}$$

The zero-order terms solution is exactly the same as the classic Reynolds solution. The θ is included in order to preserve consistency with the following sections.

Assuming no cavitation, $\theta = 1$ for each location of x making equation 2.36a the same with equation 2.32a. Note that, pressure does not depend on y as the Reynolds equation suggests so we can make use of the pressure equation with mass conservation to obtain a solution.

We start with the classical Reynolds solution without cavitation model. Boundary conditions are given as:

$$\begin{aligned} u(x,0) = U_o \ \ , u(x,h) = 0 \\ p(0) = 0 \ \ , p(1) = 0 \\ \theta(0) = 1 \ \ , \theta(1) = 1 \end{aligned}$$

Note that zero-order and first-order terms obey the same boundary conditions. The stress on the boundaries can be assumed to be zero as streamwise stress is much smaller than the pressure [77]. The solution phase can be divided into two parts. Realize that, stress coming from Oldroyd-B equations are given by the direct result of thin film approximation, can be used to simplify equation 2.36b, turning the problem into a classic Reynolds solution. The velocity is an expression of direct integrals of momentum equation:

$$u^{(0)} = \frac{y^2}{2}\frac{dp^{(0)}}{dx} + c_1 y + c2 \tag{2.38}$$

Apply boundary condition for u where for our case $u(x,h) = 0$ and $u(x,0) = 1$.

$$c_2 = 1 \tag{2.39a}$$

$$c_1 = -\frac{h}{2}\frac{dp^{(0)}}{dx} - \frac{1}{h} \tag{2.39b}$$

Replace the constant back into the equation and obtain velocity.

$$u^{(0)} = \frac{1}{2}\frac{dp^{(0)}}{dx}\left(y^2 - yh\right) + 1 - \frac{y}{h} \tag{2.40}$$

Use Eq.2.40 at mass flow without θ term for classic solution obtain v by taking integral for y:

$$\frac{\partial v}{\partial y} = -\frac{\partial u}{\partial x} = \frac{1}{2}\frac{d^2p^{(0)}}{dx^2}\left(y^2 - yh\right) - \frac{y}{2}\frac{dp^{(0)}}{dx}\frac{dh}{dx} + \frac{y}{h^2}\frac{dh}{dx} \tag{2.41a}$$

$$v = \frac{1}{12}\frac{d^2p^{(0)}}{dx^2}\left(2y^3 - 3y^2h\right) + \frac{y^2}{4}\frac{dp^{(0)}}{dx}\frac{dh}{dx} - \frac{y^2}{2h^2}\frac{dh}{dx} \tag{2.41b}$$

Utilizing 2.36a and Leibniz theorem [30] subjected to boundary conditions we can obtain pressure by Eq.2.40:

$$\frac{d}{dx}\left(h^3\theta^{(0)}\frac{dp^{(0)}}{dx}\right) = 6\frac{d(h\theta^{(0)})}{dx} \tag{2.42}$$

Until this point, Eq.2.42 is solution for Newtonain fluids. Following the same procedure to obtain viscoelastic pressure correction for first-order x-momentum equation (Eq.2.37b) can be stated after inserting equations 2.37d-2.37f and taking dobule y integral:

$$u^D = (yh - y^2)\left(\frac{\tilde{\beta}h^2}{8}\frac{dp}{dx}\frac{d^2p}{dx^2} + \frac{\tilde{\beta}h}{8}\frac{dh}{dx}\left(\frac{dp}{dx}\right)^2 - \frac{\tilde{\beta}}{4}\frac{d^2p}{dx^2} - \frac{\tilde{\beta}}{2h^3}\frac{dh}{dx} - \frac{1}{2}\frac{dp^D}{dx}\right) \tag{2.43}$$

$$
\begin{aligned}
v^D = {} & y^3 \left(\frac{\tilde{\beta} h^2 \frac{dp}{dx} \frac{d^3p}{dx^3} + \tilde{\beta} h^2 \left(\frac{d^2p}{dx^2} \right)^2 + \tilde{\beta} h \frac{d^2h}{dx^2} \left(\frac{dp}{dx} \right)^2 + \tilde{\beta} \left(\frac{dh}{dx} \right)^2 \left(\frac{dp}{dx} \right)^2}{24} \right) + \\
& y^3 \left(\frac{\tilde{\beta} h \frac{dh}{dx} \frac{dp}{dx} \frac{d^2p}{dx^2}}{6} - \frac{\tilde{\beta} \frac{d^3p}{dx^3}}{12} - \frac{\tilde{\beta} \frac{d^2h}{dx^2}}{6h^3} + \frac{\tilde{\beta} \left(\frac{dh}{dx} \right)^2}{2h^4} - \frac{\frac{d^2p^D}{dx^2}}{6} \right) + \\
& y^2 \left(- \frac{\tilde{\beta} h^3 \frac{dp}{dx} \frac{d^3p}{dx^3} + \tilde{\beta} h^3 \left(\frac{d^2p}{dx^2} \right)^2 + 5 \tilde{\beta} h^2 \frac{dh}{dx} \frac{dp}{dx} \frac{d^2p}{dx^2} + \tilde{\beta} h^2 \frac{d^2}{dx^2} h \left(\frac{dp}{dx} \right)^2}{16} \right) + \\
& y^2 \left(\frac{\tilde{\beta} h \frac{d^3p}{dx^3} + \tilde{\beta} \frac{dh}{dx} \frac{d^2p}{dx^2} - \tilde{\beta} h \left(\frac{dh}{dx} \right)^2 \left(\frac{dp}{dx} \right)^2}{8} + \frac{\tilde{\beta} \frac{d^2h}{dx^2}}{4h^2} - \frac{\tilde{\beta} \left(\frac{dh}{dx} \right)^2}{2h^3} + \frac{h \frac{d^2p^D}{dx^2}}{4} + \frac{\frac{dh}{dx} \frac{dp^D}{dx}}{4} \right)
\end{aligned}
\tag{2.44}
$$

The Eq.2.43 is the first order correction for the velocity field in most general expression. One can obtain the first order correction for vertical velocity Eq.2.44 by using Eq.2.37a.

First order velocity correction can be simplified for the channels where inlet and outlet heights are same. An usuful term used for describing the zero order pressure. The variable h_m is the maximum pressure location where $dp/dx = 0$ derived from Eq.2.36c [73].

$$
h_m = \frac{\int_0^1 h^{-2}}{\int_0^1 h^{-3}} \tag{2.45}
$$

If h_m is used for the rest of the derivation of pressure and velocity, the simplification is carried out for the parabolic type sliders. However, in different sets of geometry, the general u^D and v^D term is more suitable to employ. The simplified velocity with h_m is represented by $u^{(1)}$ to avoid confusion. Readers should care that Eq.2.43 is most general velocity term.

$$
\begin{aligned}
u^{(1)} &= \frac{h^2}{2}\frac{dp^1}{dx}\left(\frac{y^2}{h^2}-\frac{y}{h}\right)+ \\
&\frac{\tilde{\beta}}{h}\frac{dh}{dx}\left(1-3\frac{h_m}{h}\right)\left(2-3\frac{h_m}{h}\right)\left(\frac{y^2}{h^2}-\frac{y}{h}\right)
\end{aligned}
\tag{2.46}
$$

Considering simplified velocity in Eq.2.46 use Eq.2.37b to obtain first order pressure by using Leibniz theorem. The pressure neglecting cavitation is:

$$
\begin{aligned}
&\frac{d}{dx}\left(h^3\frac{dp^1}{dx}\right) \\
&= \tilde{\beta}\frac{d}{dx}\left(\frac{dh}{dx}\left(1-3\frac{h_m}{h}\right)\left(2-3\frac{h_m}{h}\right)\right)
\end{aligned}
\tag{2.47}
$$

and with the fluid flim fraction θ, it evolves:

$$
\begin{aligned}
&\frac{d}{dx}\left(h^3\theta^{(0)}\frac{dp^1}{dx}\right)+\frac{d}{dx}\left(h^3\theta^{(1)}\frac{dp^0}{dx}\right) \\
&= 6\frac{d(h\theta^1)}{dx}-2\tilde{\beta}\frac{d}{dx}\left(\theta^{(0)}\frac{dh}{dx}\left(1-3\frac{h_m}{h}\right)\left(2-3\frac{h_m}{h}\right)\right)
\end{aligned}
\tag{2.48}
$$

where both p and θ are unknown distributions. Starting from zero order equation one can sobtain pressure $p^{(0)}$ and fluid fraction $\theta^{(0)}$, and use them in Eqs. 2.37a-2.37f. To do so, we utilize the fact that the fluid fraction θ is prescribed $\theta = 1$ when $p > 0$, and $0 < \theta < 1$ when $p = p_{cav}$, where $p_{cav} = 0$ as gauge pressure for our case. The first order film fraction $\theta^{(1)}$ appearing on equation 2.48 carries significant importance in determining cavitation boundary. We can refer the equations 2.40, 2.42, 2.46, 2.48, as cavitated Linerized Reynolds Equations, which provide a steady-state solution to viscoelastic liquids first developed by Gamaniel et. al. [100].

2.4.2 Viscoelastic Reynolds Equation (VR)

By using equation 2.32b we can derive the Viscoelastic Reynolds equation. Take integral in y direction twice to obtain x-velocity u. This results as:

$$\beta u = \frac{y^2}{2}\frac{dp}{dx} + c_1 y + c2 - \int_0^y \int_0^h \frac{\partial \tau_{xx}}{\partial x} dy' dy - \int_0^y \tau_{xy} dy \tag{2.49}$$

After giving boundary conditions stated in the LIN section we can find c_1 and c_2 easily, the constant yields:

$$c_2 = \beta \tag{2.50a}$$

$$c_1 = \frac{1}{h}\int_0^h \int_0^h \frac{\tau_{xx}}{x} dy' dy + \frac{1}{h}\int_0^h \tau_{xy} dy - \frac{h}{2}\frac{dp}{dx} - \frac{\beta}{h} \tag{2.50b}$$

After replacing constants, the x-velocity is found:

$$\begin{aligned} u = & \frac{1}{2\beta}\frac{dp}{dx}(y^2 - hy) + \left(1 - \frac{y}{h}\right) + \frac{y}{\beta h}\left(\int_0^h \int_0^h \frac{\partial \tau_{xx}}{\partial x} dy' dy - \int_0^y \int_0^h \frac{\partial \tau_{xx}}{\partial x} dy' dy)\right) \\ & + \frac{y}{\beta h}\left(\frac{1}{h}\int_0^h \tau_{xy} dy - \int_0^y \tau_{xy} dy\right) \end{aligned} \tag{2.51}$$

After replacing equation 2.51 into the continuity equation 2.32a we can eliminate u by using Leibniz theorem and necessary boundary condition the following equation is obtained:

$$\frac{d}{dx}\left(\frac{h^3}{12}\frac{dp}{dx}\right) = \frac{\beta}{2}\frac{dh}{dx} + \frac{d}{dx}\left(\int_0^h \frac{y}{h}\int_0^h\int_0^y \frac{\partial \tau_{xx}}{\partial x}dy''dy'dy \quad - \int_0^h\int_0^y\int_0^y \frac{\partial \tau_{xx}}{\partial x}dy''dy'dy\right) + \frac{d}{dx}\left(\int_0^h \frac{y}{h}\int_0^h \tau_{xy}dy'dy - \int_0^h\int_0^y \tau_{xy}dy'dy\right) \tag{2.52}$$

Fluid film fraction, θ, can be integrated with VR by Eq.2.34 because it is more straightforward to take integral as θ is not separated as zero and first order. There is one general θ value that should be considered. θ does not depend on the y axis, thus it can leave outside of the integral. But it remains inside of the x-derivative. Then θ can be attached inside equation 2.52. The equation is very similar to the previous equation except for the fraction.

$$\begin{aligned}\frac{d}{dx}\theta\left(\frac{h^3}{12}\frac{dp}{dx}\right) = \frac{\beta}{2}\frac{d(h\theta)}{dx} + \frac{d}{dx}\theta\left(\int_0^h \frac{y}{h}\int_0^h\int_0^y \frac{\partial \tau_{xx}}{\partial x}dy''dy'dy\right. \\ \left. - \int_0^h\int_0^y\int_0^y \frac{\partial \tau_{xx}}{\partial x}dy''dy'dy\right) \\ + \frac{d}{dx}\theta\left(\int_0^h \frac{y}{h}\int_0^h \tau_{xy}dy'dy - \int_0^h\int_0^y \tau_{xy}dy'dy\right)\end{aligned} \tag{2.53}$$

Let's examine the appearing terms in Eq.2.53. The first term on RHS is the solvent pressure which remains the same. But remember that from Eq.2.29, we should able to combine the polymer viscosity with the solvent viscosity. Even without any effect of viscosity ($De = 0$), the Eq.2.52 should satisfy Eq.2.32b. Using Eq.2.36e we can state that τ_{xy} is attributed to Newtonian stress generated by the polymers. Noting that, the overall τ_{xy} can be separated:

$$\tau_{xy}^{total} = (1-\beta)\tau_{xy}^{polymer} + \beta\tau_{xy}^{lubricant} + \tau_{xy}^{viscoelastic}(De) \tag{2.54}$$

The section is concluded by the friction caused at the boundaries. Friction force (shear force) applied on the components of the lubrication contacts per unit length are given:

$$f_b = \int_0^1 (\tau_{xy})_{y=0}\ dx \tag{2.55a}$$

$$f_t = \int_0^1 (-\tau_{xy})_{y=h}\ dx \tag{2.55b}$$

With LIN approximation for shear stress expressed as:

$$f_b = \int_0^1 -(\frac{\partial u^{(0)}}{\partial y} + De\ \tau_{xy}^{(1)})_{y=0}\ dx \tag{2.56}$$

Lastly, one can calculate the generated load simply by taking the integral of the pressure over the length of the channel. Given as:

$$W = \int_0^1 p dx \tag{2.57}$$

Then friction coefficient is simply:

$$\mu = \frac{f_b}{W} \tag{2.58}$$

The next chapter talks about the numerical procedure to solve pressure and solid deformation equations.

Chapter 3

Numerical Algorithm

In this section, detailed numerical methodology is introduced for the given equations in Sec.2. First elastic deformation theory pretested separated from lubrication part. The numerical methods follow the combination of linear elastic theory and the solution of linear and non-linear Reynolds equations. Thus, the reader is directed to Sec.2 to revise the mathematical background.

The coupled problem is solved simultaneously, as the pressure required for determining both deformation and film thickness needs to be updated to calculate new pressure until both are converged and satisfy Eq.2.7, Eq.2.57 and Eqs.2.36c-2.37c.

The simulation schematic is shown in Fig.3.1. The problem starts by initializing the film thickness. Then pressure is obtained by solving lubrication equations and fed to the elastic kernel to compute deformation until film thickness and pressure are converged. Load balance checks if the generated load is the same as the applied load, if not this step continues by updating the minimum film thickness. All of the procedure continues until pressure, height and load requirements are satisfied.

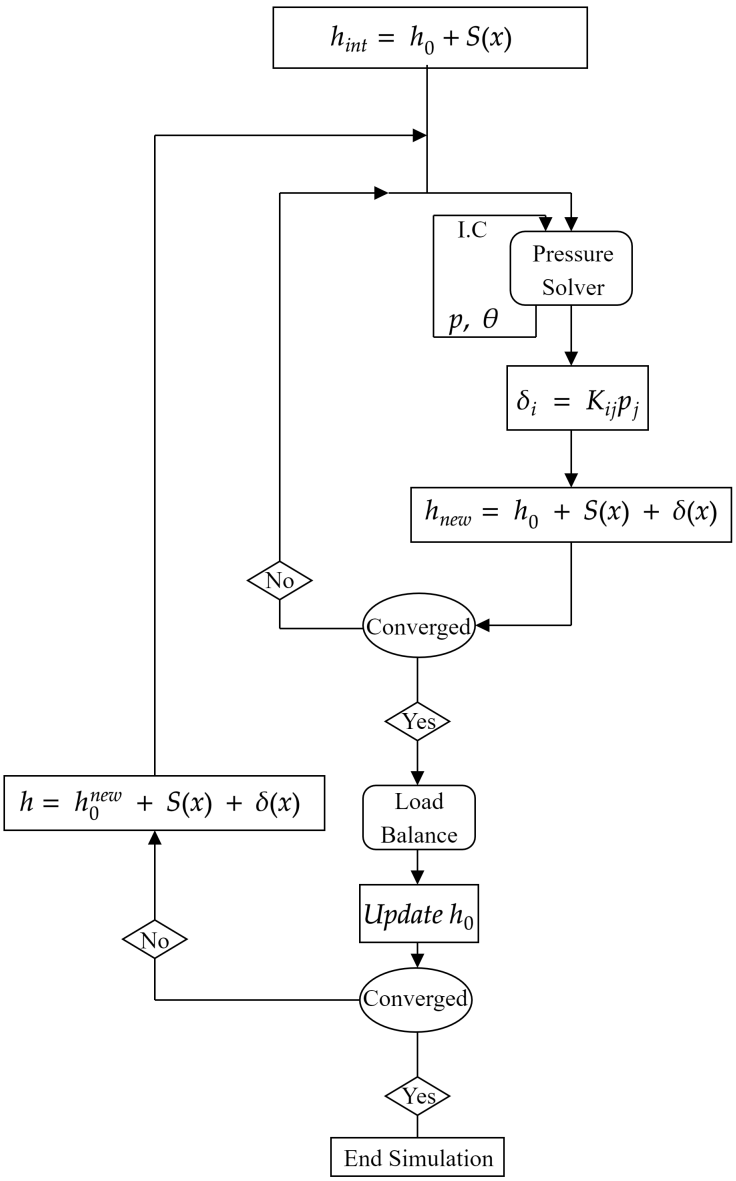

Figure 3.1: The EHL simulation flow schematic

All the fluid properties, the velocity field, stress field and pressure field are measured in the Pressure solver. The rest includes the requirements to run the EHL conditions. Therefore, one can solve a pressure solver for an HL case without dealing with elastic deformation.

A small note, cavitation is a must to generate a positive load due to cavitation, the pressure drop is limited by the zero gauge pressure and a positive load is created. As we are seeking a steady-state solution the transient effects, if exist, are eliminated. Thus, height change do not contribute to pressure equations by rate of change.

In the following Sec.3.1 a numerical procedure of obtaining an elastic kernel is told with the load balance equations. Then Secs.3.3.1,3.3.3 includes numerical procedures to obtain pressure. Lastly we combine them in Sec.3.4 with comprehensive outlook for the simulation.

3.1 Elastic Deformation

The procedure for solving Eq.2.7 for elastic materials is described by Putignano *et. al.* [91]. To discretize the equation, the contact domain is divided into N nodes. Within each domain cell, the pressure is assumed to be constant, denoted as $p_k = p(x_k)$, where x_k is the location of the center point of the cell D_k. The normal displacement δ_i is represented as follows

$$\delta_i = \sum_{j}^{N} G_\omega(x_i - x_j) \cdot p_j \tag{3.1}$$

In Eq.3.1, the integral term can be calculated by using Love's solution for elastic materials [91]. The solution is simply converted into a system of linear equations in

the form of

$$\delta_i = K_{ij} p_j, \tag{3.2}$$

where the response matrix K_{ij} is the condensed form of Eq.3.1 without stress term. For the theses, a procedure to obtain K will be shown for a sample case containing 4 nodes. Thus, we will obtain $(4x4)$ matrix at the end of the procedure.

The procedure for solving Eq.4 for elastic materials is described by Putignano [92]. To discretize the equation, the contact domain is divided into N nodes. Within each domain cell, the pressure is assumed to be constant, denoted as $p_k = p(x_k)$, where x_k is the location of the center point of the cell D_k. Thus, the deformation is just solved for one cell k.

Start by constructing discretization of Eq.2.9. Relaize that there is dirac delta which is one when $q = kq_0$, and zero for the rest of different q values. Thus, green function turns to be a function of integer k from minus infinity to plus infinity. Then

$$G(q) = \frac{q_0}{2\pi} \frac{1-\nu^2}{|kq|} \frac{2sin(\frac{1}{2}kq_0 dx)}{kq_0} \tag{3.3}$$

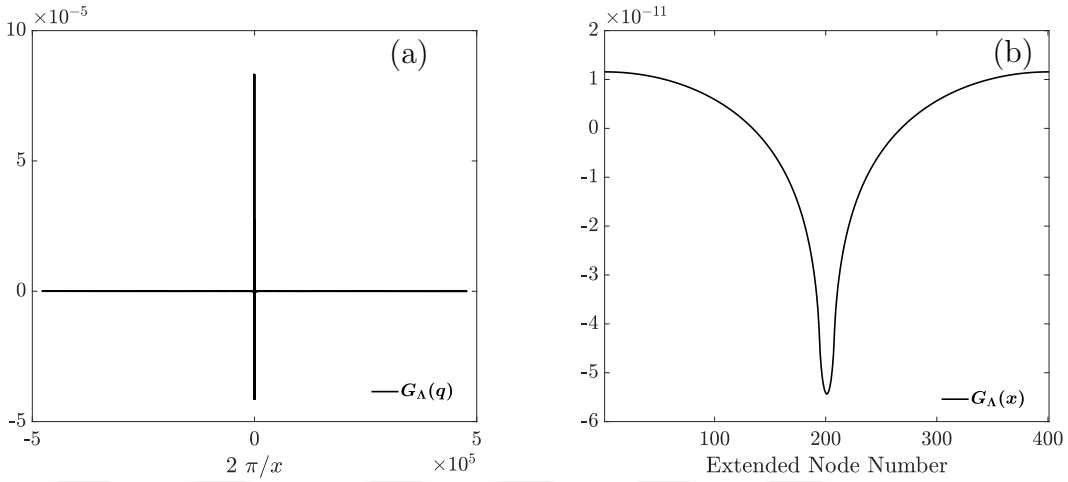

Figure 3.2: Green function (a) Fouirer domain (b) Real domain

The boundries of the Green function is consisting of the cell inner nodes. In order to do that, another fine mesh is required to solve cell problem. For instance, 4 nodes general mesh is transformed to 400 nodes to measure the effect of the pressure at that cell to other points of the surface. Thus, one cell contains extra 100 nodes. This numbers are numerically choosen similar to conventional mesh griding.

Grapichal representation of Eq.3.3 and its Fast Fourire Transformed function $G_\Lambda(x)$ are shown:

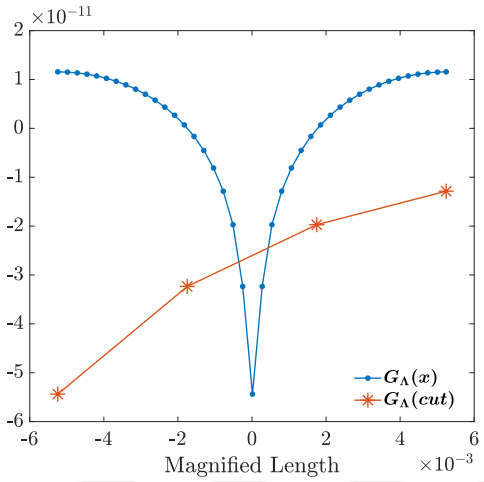

Figure 3.3: Green function cut

In Fig.3.2 the Fourire domain and real domain of Green function has shown. Question can be raised for obtaining the Green function. For this thesis, Love's solution is omitted. Thus, for further details readers should look at Love's formula. Observe in Fig.3.2(b), the center has the largest multiplier, meaning that pressure, p_k at location x_k elastically mostly deforms vicinity of the x_k and the deformation multiplier slowly diminishes at far locations. As $G(x)$ is obtained Eq.2.8, can be calculated.

Realize that $G(x)$ is built for increased number of nodes that, each general node has 100 nodes more. Select evenly distributed 40 nodes out of 400 to reduce Green function and select nearest 4 to the center. This is shown in Fig.3.3. Thus, for a system consisting of 20 nodes, G_{cut} would consist of 20 nodes instead of 4.

The elastic kernel then, is basically a matrix containing elastic multiliers for each location. Pressure, p_k, has the largest multiplier on location x_k and slightly less on x_{k-1} etc.

3.2 Linear Viscoelastic Model

In LIN the solution is separated into two parts; the zero-order terms and first-order terms. The zero-order solution is basically the same solution as the classic Reynolds equation.

Without cavitation, the LIN provides straightforward analytical solutions for pressure. However, the existence of the θ term in mass conservation leads to a more complicated solution scheme. The way of Elrod-Adams algorithm (or more generally $p-\theta$ algorithm) works with an unknown θ distribution which enables a switch function property. Some other cavitation models introduce a direct switch function along with the mass ratio term θ, [87] however, in $p-\theta$ it is not included. Instead of a switch function, an iterative approach is used to locate the cavitation position.

Regarding Eqs.2.36c-2.37c , Elrod and Ausas suggest using the backward difference in spatial derivative for computational purposes [85],[82]. Vijayaraghavan uses a half-step central difference scheme for the mass balance equation and Bayada also suggests using this form of differential form [101],[102]. With enough nodes, the pressure outcome comes out the same with both schemes. Using backward difference is said to be more appropriate as the data is not coming from a downwaard stream [103]. Mesh refinment can help to capture sharp derivatives better where it is fully explored in following Sec.4.

The numerical method is quite slow as each node is solved independently. Normally, without a switch function non-linearity, the equation can be solved by the TDMA method. However, with Gauss-Seidel, each location needed to be solved for checked by θ to capture cavitation location. If the fluid is full film pressure equation should be solved. If it is bubble-liquid mixture fluid fraction should be solved as we know $p = p_{cav} = 0$. The solution procedure is given in Fig.3.4 and

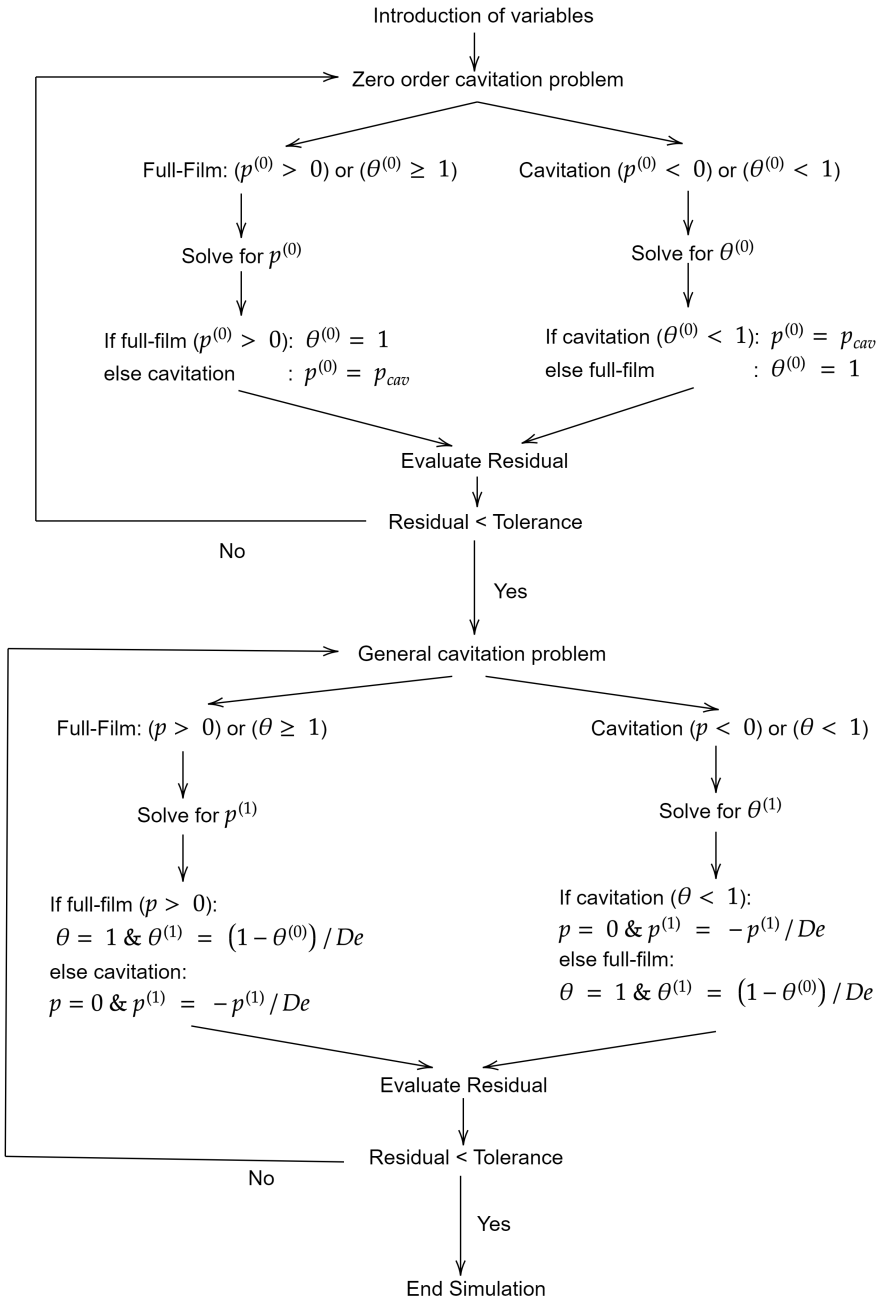

Figure 3.4: The EHL simulation flow schematic

followed by its discretization. Let's start with the zero-order pressure solution:

$$p_i^{(0)} = \frac{h_i^3\theta_i^{(0)}p_{i+1}^{(0)} + h_{i-1}^3\theta_{i-1}^{(0)}p_{i-1}^{(0)}\theta_i p_{i+1}^{(0)} - 6\Delta x(h_i\theta_i^{(0)} - h_{i-1}\theta_{i-1}^{(0)})}{h_i^3\theta_i^{(0)} + h_{i-1}^3\theta_{i-1}^{(0)}} \tag{3.4}$$

The θ solution is given as:

$$\theta_i^{(0)} = \frac{6\Delta x h_{i-1}\theta_{i-1}^{(0)} - h_{i-1}^3\theta_{i-1}^{(0)}(p_i^{(0)} - p_{i-1}^{(0)})}{6\Delta x h_i - h_i^3(p_{i+1}^{(0)} - p_i^{(0)})} \tag{3.5}$$

Convergence is assessed using the Euclidean norm for both the pressure denoted as $E_p = ||p_{new} - p_{old}||^2$, ensuring that it is smaller than 10^{-9}.

$$F_1 = h_i^3\theta_i^{(0)}p_{i+1}^{(1)} + h_{i-1}^3\theta_{i-1}^{(0)}p_{i+1}^{(1)} \tag{3.6a}$$

$$F_2 = h_i^3\theta_i^{(0)} + h_{i-1}^3\theta_{i-1}^{(0)} \tag{3.6b}$$

$$F_3 = h_i^3\theta_i^{(1)}(p_{i+1}^{(0)} - p_i^{(0)}) + h_{i-1}^3\theta_{i-1}^{(1)}(p_i^{(0)} - p_{i-1}^{(0)}) \tag{3.6c}$$

$$F_4 = 6\Delta x(\theta_{i-1}^{(1)}h_i - \theta_{i-1}^{(1)}h_{i-1}) \tag{3.6d}$$

$$F_5 = 4(1-\beta)(\theta_i^{(0)}(h_{i+1} - h_i) - \theta_{i-1}^{(0)}(h_i - h_{i-1})) \tag{3.6e}$$

$$F_6 = 18(1-\beta)h_m\left[\left(\frac{\theta_i^{(0)}(\frac{h_m}{h_i} - 1)(h_{i+1} - h_i)}{h_i}\right) - \left(\frac{\theta_{i-1}^{(0)}(\frac{h_m}{h_{i-1}} - 1)(h_i - h_{i-1})}{h_{i-1}}\right)\right] \tag{3.6f}$$

After getting discretization, combine them to obtain first-order pressure

$$p_i^{(1)} = -\frac{(F_4 - F_5 - F_6 - F_3 - F_1)}{F_2} \tag{3.7}$$

Now, for non-Newtonian $\theta^{(1)}$, we collect discritazion

$$F_1 = h_i^3(p_{i+1}^{(0)} - p_i^{(0)}) - 6\Delta x h_i \tag{3.8a}$$

$$F_2 = \theta_{i-1}^{(1)}(h_{i-1}^3(p_i^{(0)} - p_{i-1}^{(0)}) - 6\Delta x h_{i-1}) \tag{3.8b}$$

$$F_3 = h_i^3\theta_i^{(0)}(p_{i+1}^{(1)} - p_i^{(1)}) - h_{i-1}^3\theta_{i-1}^{(0)}(p_i^{(1)} - p_{i-1}^{(1)}) \tag{3.8c}$$

$$F_4 = 4(1-\beta)(\theta_i^{(0)}(h_{i+1} - h_i) - \theta_{i-1}^{(0)}(h_i - h_{i-1})) \tag{3.8d}$$

$$F_5 = 18(1-\beta)h_m\left[\left(\frac{\theta_i^{(0)}(\frac{h_m}{h_i} - 1)(h_{i+1} - h_i)}{h_i}\right) - \left(\frac{\theta_{i-1}^{(0)}(\frac{h_m}{h_{i-1}} - 1)(h_i - h_{i-1})}{h_{i-1}}\right)\right] \tag{3.8e}$$

combine them to obtain first-order fluid film fraction

$$\theta_i^{(1)} = \frac{(F_2 - F_3 - F_4 - F_5)}{F_1} \tag{3.9}$$

The convergance for first order is assed by norm with total θ and p, $E_p = ||\theta_{new} - \theta_{old}|^2 + |p_{new} - p_{old}|^2|$, ensuring that it is smaller than 10^{-9}.

3.3 Viscoelastic Reynolds Formulation

This method was developed by Humayun & Luca [78]. Instead of lingering the constitutive equations of Oldroyds-B viscoelastic equations, they use them in the momentum equation. In the linearized approach the advection of the τ_{xx} is totally missed. Thus resulting in underestimation of τ_{xx}.

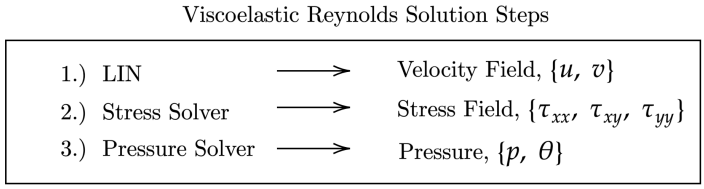

Figure 3.5: The VR Solution Schematic

Viscoelastic Reynolds is solved by 2 different approaches. One is using mesh for two dimensions. The other one is the polynomial approach which is more broadly discussed in [78]. In the polynomial approach the stress of $\{\tau_{xx}, \tau_{xy}, \tau_{yy}\}$ are the polynomials for y direction. They have a common point for initial conditions. Both of the method takes the velocity field and initial stress field from the LIN solution. Thus the starting point is the same for both methods. The numerical differences are discussed in the below section.

3.3.1 Stress Solvers

The height profile is a parabola, cosine most of the lubrication study. Thus, the curve should be reflected by the grid. It can be easily applicable by changing δy in each x_i location. If it is uniform mesh and node number does not change by x, for a height $h(x)$, we can say that δy at initial position x_1 will be divided by $h(x_i)$ to node number N_y. This is reflected in the whole domain. But for computational purposes, we need to find the Jacobi transformation of the mesh in order to take derivatives. This is also easily accomplished due to easy geometry.

Adaptive Mesh

First we introduce the adaptive mesh for stress solver latter a polynomial

approach. Take an initial configuration $\bar{X}$ for a domain. The domain is 2D for our cases and the selected direction are x and y. The y-axis depends on the x for the construction adaptive mesh and x direction is free. Thus we can connect computational y in this form:

$$y_i = h(x_i) \quad \text{and} \quad \Delta y_i = \frac{h(x_i)}{N_y} \tag{3.10}$$

We want to convert y to a new coordinate system to run the simulations easier and get rid of complexities at boundaries. For this thesis, no-slip condition is used. Thus, it is known that velocity on the top (no sliding) is zero and stationary. But this should be reflected in derivatives too. Taking the derivative in the x direction at top is problematic for finite difference as the nodal point lies outside of the mesh. The first conversion is the main coordinates:

$$\boldsymbol{\chi'} = \begin{bmatrix} x' \\ y' \end{bmatrix} = \begin{bmatrix} x \\ \frac{y}{h(x)} \end{bmatrix} \tag{3.11}$$

Jacobi of this configuration can be taken by the derivative for the position vector. The resulting Jacobi is given as:

$$\boldsymbol{J} = \frac{d\boldsymbol{\chi'}}{d\boldsymbol{x}} = \begin{bmatrix} \frac{\partial x'}{\partial x} & \frac{\partial x'}{\partial y} \\ \frac{\partial y'}{\partial x} & \frac{\partial y'}{\partial y} \end{bmatrix} = \begin{bmatrix} 1 & 0 \\ -y\frac{1}{h^2}\frac{dh}{dx} & \frac{1}{h(x)} \end{bmatrix} \tag{3.12}$$

When taking the derivative in the x direction we have obtained one more direction towards y which is expected. An example of using Jacobi is given in the below derivative.

$$\frac{d(.)}{dx} = \frac{\partial(.)}{\partial x'}\frac{\partial x'}{\partial x} + \frac{\partial(.)}{\partial y'}\frac{\partial y'}{\partial x} \tag{3.13}$$

$$\frac{d(.)}{dy} = \frac{\partial(.)}{\partial y'}\frac{\partial y'}{\partial y} + \frac{\partial(.)}{\partial x'}\frac{\partial x'}{\partial y} \tag{3.14}$$

After replacing Jacobi values to the 3.13 and 3.14 we obtain following exact derivatives:

$$\frac{d(.)}{dx} = \frac{\partial(.)}{\partial x'} - \frac{\partial(.)}{\partial y'}\frac{y}{h(x)^2}\frac{dh(x)}{dx} \tag{3.15}$$

$$\frac{d(.)}{dy} = \frac{\partial(.)}{\partial y'}\frac{1}{h(x)} \tag{3.16}$$

In the current case, derivatives with respect to new coordinates are complete. And following should be considered while raking derivative or defining a variable. Consider a quantity of ϕ is generated for the field. This can be done in two distinct ways, The first is defined by giving each nodal point a value for the quantity on the non-transform coordinate y. Thus, the computational matrix y is defined by changing δy for each x_i and ϕ is stored on top of it. One can first make a grid transform and store value for new coordinate y'. Both should be regarded while implementing to numerical algorithm. I preferred storing each quantity on the y and directly using it for whole physical quantities. Partial derivative is also taken with respect to it, meaning that in derivative calculations dependent δy is considered. Making 3.16 equal mathematically by using $y' = y/h$:

$$\frac{d\phi}{dy} = \frac{\partial\phi}{\partial y'}\frac{1}{h(x)} = \frac{\partial\phi}{\partial y}\frac{h(x)}{h(x)} = \frac{\partial\phi}{\partial y} \tag{3.17}$$

By using same relationship, 3.15 can be utilized and also $x = x'$ is regarded:

$$\frac{d\phi}{dx} = \frac{\partial\phi}{\partial x} - \frac{\partial\phi}{\partial y}\frac{y}{h(x)}\frac{dh(x)}{dx} \tag{3.18}$$

For each derivative, this scheme is applied. Oldroyds-B constitutive equations are computed directly by using these features.

Solution of equations 2.32a, temporal part is solved with explicit Euler and 4th order Runge-Kutta schemes, the spatial part is expanded through by the upwind downwind and central differencing scheme. Realize that the pressure is strictly dependent on the stresses created by the polymers. First stress is calculated by the given scheme, then outcomes are used in order to find pressure by a tri-diagonal system. The challenge is to address coupled Oldroyd-B constitutive equations. The stress must be calculated at the same time step, meaning that instability of any directional stress has an effect on another.

First, define some operators to conduct derivatives for any matrix $\mathbf{\Phi}$ in x and y direction for all i and j. A derivative of any node in matrix (i, j) demonstrated by central differentiating scheme

$$\boldsymbol{\psi}_{\boldsymbol{x}}^{\boldsymbol{CD2}}(\Phi_{i,j}) = \frac{\Phi_{i+1,j} - \Phi_{i-1,j}}{2\Delta x} - \frac{\Phi_{i,j+1} - \Phi_{i,j-1}}{2\Delta y_i}\frac{y_{i,j}}{h_i}\frac{h_{i+1} - h_{i-1}}{2\Delta x} \tag{3.19}$$

$$\boldsymbol{\psi}_{\boldsymbol{y}}^{\boldsymbol{CD2}}(\Phi_{i,j}) = \frac{\Phi_{i,j+1} - \Phi_{i,j-1}}{2\Delta y_i} \tag{3.20}$$

For any matrix, this operation can repeated for all nodes and can be extended to other differentiating schemes such as first order forward or backwards difference. As in simulations upwind is never used for both velocities the upwind scheme can be shown as:

$$\boldsymbol{\psi}_{\boldsymbol{x}}^{\boldsymbol{UW}}(\Phi_{i,j}) = \frac{\Phi_{i,j} - \Phi_{i-1,j}}{\Delta x} - \boldsymbol{\psi}_{\boldsymbol{y}}^{\boldsymbol{CD2}}(\Phi_{i,j})\frac{y_{i,j}}{h_i}\boldsymbol{\psi}_{\boldsymbol{x}}^{\boldsymbol{CD2}}(h_{i,j}) \tag{3.21}$$

$$\boldsymbol{\psi}_{\boldsymbol{y}}^{\boldsymbol{UW}}(\Phi_{i,j}) = \frac{\Phi_{i,j} - \Phi_{i,j-1}}{\Delta y_i} \tag{3.22}$$

if user want to use upwind scheme for y-velocity, should change the central differencing in UW scheme in x-velocity (Eq.3.21) to UW. Then, we can proceed with the time integration of the equations in coupled form. For time integration, as a explicit scheme, 4th-order Runge-Kutta is employed where Runge-Kutta provides good accuracy and easy to implement. On the other hand, employing implicit scheme is cumbersome due to coupling of the stress terms. This problem can be over taken by using semi-implicit schemes. The appropriate choice for implementing semi-implicit scheme is Crank-Nicolson which has advantage over implicit Euler scheme in accuracy and stability.

Runge Kutta

Starting from Runge-Kutta formulations we simplify some terms to have an overlook of the numerical scheme, in a complete matrix form where selection of scheme is just optional but terms without advection speed can be just used $CD2$. Higher order schemes are mostly create instabilities in solver:

$$\boldsymbol{\tau} = \begin{bmatrix} \boldsymbol{\tau_{xx}} \\ \boldsymbol{\tau_{xy}} \\ \boldsymbol{\tau_{yy}} \end{bmatrix} \tag{3.23}$$

$$\boldsymbol{M_{ex}} = \begin{bmatrix} (\frac{-1}{De} + 2\boldsymbol{\Psi}_{\boldsymbol{x}}^{(*)}(\boldsymbol{u})) & 2\boldsymbol{\Psi}_{\boldsymbol{y}}^{(*)}(\boldsymbol{u}) & 0 \\ \boldsymbol{\Psi}_{\boldsymbol{x}}^{(*)}(\boldsymbol{v}) & \frac{-1}{De} & \boldsymbol{\Psi}_{\boldsymbol{y}}^{(*)}(\boldsymbol{u}) \\ 0 & 2\boldsymbol{\Psi}_{\boldsymbol{x}}^{(*)}(\boldsymbol{v}) & (2\boldsymbol{\Psi}_{\boldsymbol{y}}^{(*)}(\boldsymbol{v}) - \frac{1}{De}) \end{bmatrix} \tag{3.24}$$

$$\boldsymbol{D} = \begin{bmatrix} 0 \\ (1-\beta)\boldsymbol{\Psi}_{\boldsymbol{y}}^{(*)}(\boldsymbol{u}) \\ 2(1-\beta)\boldsymbol{\Psi}_{\boldsymbol{y}}^{(*)}(\boldsymbol{v}) \end{bmatrix} \tag{3.25}$$

Thus, in closed and complete form, explicit discretization is shown:

$$\boldsymbol{\tau^{t+\delta t}} = \boldsymbol{\tau^{t}} + \delta t \left\{ \boldsymbol{M_{ex}}\boldsymbol{\tau}^{t} + \boldsymbol{D} - \boldsymbol{u}\boldsymbol{\Psi_{x}}(\boldsymbol{\tau^{t}}) - \boldsymbol{v}\boldsymbol{\Psi_{y}}(\boldsymbol{\tau^{t}}) \right\} \tag{3.26}$$

In this closed form, matrices $\{\boldsymbol{M_{ex}}, \boldsymbol{D}\}$ can be predefined as the velocity field is independent of time. The stress terms, however, should be computed in each time step. Call $\{\boldsymbol{M_{ex}}(.) + \boldsymbol{D} - \boldsymbol{u}\boldsymbol{\Psi_{x}}(.) - \boldsymbol{v}\boldsymbol{\Psi_{y}}(.)\}$ function as $OB()$, short name for Oldroyd-B and takes stress as an input. Runge-Kutta formulation then proceed as follows

$$K_1 = OB(\boldsymbol{\tau^{t}}) \tag{3.27a}$$

$$K_2 = OB(\boldsymbol{\tau^{t}} + K_1 \cdot \delta t/2) \tag{3.27b}$$

$$K_3 = OB(\boldsymbol{\tau^{t}} + K_2 \cdot \delta t/2) \tag{3.27c}$$

$$K_4 = OB(\boldsymbol{\tau^{t}} + K_3 \cdot \delta t) \tag{3.27d}$$

$$\boldsymbol{\tau^{t+\delta t}} = \boldsymbol{\tau^{t}} + \frac{\delta t}{6}(K_1 + 2K_2 + 2K_3 + K_4) \tag{3.27e}$$

Before starting time integration, we need to spot the initial value of the stress field. The initial value is determined by the Newtonian solution of stress coming

from Eq.2.36d-2.36f. Similarly, the velocity field is taken from the LIN solution, by Eq.2.40 and Eq.2.46. The $\boldsymbol{v}$ can be obtained by using mass conservation after taking the derivative of $\boldsymbol{u}$ in x and integrating it with respect to y.

The initialized Eqs.2.32d-2.32f with suitable boundary conditions are ready to be solved. The time interval is selected by tuning after several runs. Large-time steps cause instability in solving the equations. Thus, small time steps are required to reach a stable solution. In order to improve the stability, an implicit solution of the Oldroyd-B is required which is a tough problem to solve. Arranging a suitable time step is crucial not just for stability but the solution time. For very small time steps solution time can reach very high time durations, the maximum possible time step should be selected to prevent time overflow. Runge Kutta 4th order is respectively easy task to implement for the Oldroyd-B equations compared to implicit schemes. Thus, RK4 gives a mostly stable and good range of time steps to work with.

Another crucial aspect of the problem is the discretization of advection terms. The upwind scheme can be implemented to provide more stable solutions even if the A.1a shown in the central difference scheme, it is possible to use Upwind and downwind schemes. This requires a logical map of the velocity in the domain to ensure the flow direction. For a positive value of velocity, a backward difference scheme should be implemented and for a negative value, a forward is required.

Crank-Nicolson

Now, semi implicit Crank-Nicolson is introduced. We use same template but slightly changing coupling matrix $\boldsymbol{M_{ex}}$ and present new matrix that fits semi-implicit approach where spatial schemes are shown explicitly as up-wind is must for CN, the specific location of UW is highlighted. Ofcourse for negative x-speeds, downwind scheme is used.

$$\boldsymbol{M_{im}} = \begin{bmatrix} 0 & 2\boldsymbol{\Psi}_{\boldsymbol{y}}^{CD2}(\boldsymbol{u}) & 0 \\ \boldsymbol{\Psi}_{\boldsymbol{x}}^{CD2}(\boldsymbol{v}) & 0 & \boldsymbol{\Psi}_{\boldsymbol{y}}^{CD2}(\boldsymbol{u}) \\ 0 & 2\boldsymbol{\Psi}_{\boldsymbol{x}}^{CD2}(\boldsymbol{v}) & 0 \end{bmatrix} \tag{3.28}$$

The main diagonal is transferred to next time step, thus resulting 0-main diagonal matrix. We crate another matrix with the main diagonal components:

$$\boldsymbol{D_{im}} = \begin{bmatrix} \frac{-1}{De} + 2\boldsymbol{\Psi}_{\boldsymbol{x}}^{CD2}(\boldsymbol{u}) \\ \frac{-1}{De} \\ \frac{-1}{De} + 2\boldsymbol{\Psi}_{\boldsymbol{y}}^{CD2}(\boldsymbol{v}) \end{bmatrix} \tag{3.29}$$

$$\begin{aligned} \boldsymbol{D_{im}}\boldsymbol{\tau}^{\boldsymbol{t+\delta t}} + \frac{1}{2}\boldsymbol{u}\boldsymbol{\Psi}_{\boldsymbol{x}}^{UW}(\boldsymbol{\tau}^{\boldsymbol{t+\delta t}}) + \frac{1}{2}\boldsymbol{v}\boldsymbol{\Psi}_{\boldsymbol{y}}^{CD2}(\boldsymbol{\tau}^{\boldsymbol{t+\delta t}}) = \\ \boldsymbol{\tau}^{\boldsymbol{t}} + \frac{\delta t}{2}\left\{\boldsymbol{M_{im}}\boldsymbol{\tau}^{t} + \boldsymbol{D}\right\} + \frac{\delta t}{2}\left\{\boldsymbol{M_{ex}}\boldsymbol{\tau}^{t} + \boldsymbol{D} - \boldsymbol{u}\boldsymbol{\Psi}_{\boldsymbol{x}}^{UW}(\boldsymbol{\tau}^{\boldsymbol{t}}) - \boldsymbol{v}\boldsymbol{\Psi}_{\boldsymbol{y}}^{CD2}(\boldsymbol{\tau}^{\boldsymbol{t}})\right\} \end{aligned} \tag{3.30}$$

In this form, the implicit part has five-unknowns for each cell location (i, j), due to the incoming information by neighborhood cells. This leading to create (N_x^2)x(N_y^2) matrix where just 5 diagonals are full filled. There are strong methods to solve 5 diagonal systems which can found in literature or direct iterative solvers can be used optimized for 5 diagonal matrix systems [77]. Although strong methods are available, due to simplicity alternating direction implicit method (ADI) is employed to overcome this difficulty. In ADI one of the implicit terms are regarded as explicit and the rest of the implicit terms are solved with TDMA for each column for explicit term. In order to avoid extra terms appearing in x derivative, starting from y derivative the computation is carried out:

$$\boldsymbol{D_{im}\tau^{t+\delta t/2}} + \frac{1}{2}\boldsymbol{v\Psi_y^{CD2}(\tau^{t+\delta t/2})} = \boldsymbol{\tau^t} + \frac{\delta t}{4}\left\{\boldsymbol{M_{im}\tau^t + D - u\Psi_x^{UW}(\tau^t)}\right\} + \tag{3.31a}$$

$$\frac{\delta t}{4}\left\{\boldsymbol{M_{ex}\tau^t + D - u\Psi_x^{UW}(\tau^t) - v\Psi_y^{CD2}(\tau^t)}\right\}$$

$$\boldsymbol{D_{im}\tau^{t+\delta t}} + \frac{1}{2}\boldsymbol{u\Psi_x^{UW}(\tau^{t+\delta t})} = \boldsymbol{\tau^{t+\delta t/2}} + \frac{\delta t}{4}\left\{\boldsymbol{M_{im}\tau^{t+\delta t/2} + D - v\Psi_y^{CD2}(\tau^{t+\delta t/2})}\right\} + \tag{3.31b}$$

$$\frac{\delta t}{4}\left\{\boldsymbol{M_{ex}\tau^t + D - u\Psi_x^{UW}(\tau^t) - v\Psi_y^{CD2}(\tau^t)}\right\}$$

Note that upwind or downwind is more critical to use in implicit schemes where central difference do not work most of the time with high time-step values. Crank-Nicolson provides very fast solutions without stability problems although, at least time-step down to $0.01s$ which is still below what Humayun & Luca employed with iterative solver [77]. Several modifications are also possible to obtain faster solution like using the first stress in second set of calculations. After obtaining $\boldsymbol{\tau_{xx}^{(t+\delta t)}}$ it is used directly in the calculation of $\boldsymbol{\tau_{xy}^{(t+\delta t)}}$ and $\boldsymbol{\tau_{yy}^{(t+\delta t)}}$.

The convergence is guaranteed by taking the Euclidean norm for each location. The residual is calculated $\boldsymbol{r} = |\boldsymbol{\tau^{t+\delta t} - \tau^t}|$. The tolerance has parametric selection by the time step. The tolerance $Tol = 10^{(-7+log(dt))}$ is arranged after empirical studies.

The method to solve VR with polinoms is given in App.A. This method directly reflects Humayun & Luca paper [78].

3.3.2 Boundary conditions

Boundary condiations should be well defined to solve the given PDE's in this thesis. In this section, the numerical methods to employ boundary conditions are shown. Most of the time for the channel flow used in this work has Dirichlet for pressure and Neumann for stress equations. Both Diriclet and Neumann B.C are set to zero as the stress is quite small compared to pressure and does not have effective contribution to pressure value. Also, when polymers leave the channel zero gradient is reasonable choice [77, 69].

The zero Neumann is applied at the one end of the channel and one of the walls. Numerically is shown as:

$$\boldsymbol{\tau_{(N-1,y)}} = \boldsymbol{\tau_{(N,y)}} \tag{3.32}$$

$$\boldsymbol{\tau_{(x,M-1)}} = \boldsymbol{\tau_{(x,M)}} \tag{3.33}$$

The other end is calculated by the same order of the central differencing for forward difference.

Periodic B.C is also required for several applications. If the micro-stress state of the polymers leaves channel with zero-gradient and reenters the channel periodic B.C should be applied. Espically, in modelling journal bearings, the fluid leaving the squuzed part, travels through journal and squuzed again [29]. Other application might be the channel profile which has periodic height change. Considering the cavitation, the fludi film fraction should also changed by periodically, leading to solve stress, fluid film fraction and pressure periodically.

The periodic stress can easliy given similar to the zero-gradient stress:

$$\boldsymbol{\tau_{(1,y)}} = \boldsymbol{\tau_{(N,y)}} \tag{3.34}$$

Tri-diagonal pressure is also required to be solved periodically as mention in [77]. In parabolic slider the pressure is relatievly small and close to zero but for different type of channel pressure might translated for the next cell. Periodic tri-diagnol systems for non-cavitatied models are solved by the alterations for existing classical TDMA algorithm in [104, 105]. Eventough, the pressure is solved periodically by employing the given algorithms, a reference atmospheric pressure should inserted as a reference pressure. Otherwise, pressure can take any value in solution space while the pressure derivative are same every point. This reference usullay selected as 0 for consistancy with Dirichlet B.C.

In cavitation case, starting or ending point should be selected as a reference to fixed the quantities in solution space. The other point is solved for both θ and p. Thus, if the fluid leaves the channel vaporized phase, the inlet should start in vaporized phase. In fact the existing algorithm given in Gamaniel et. al. [100] preassumes the leaving film is full film and this leads to sudden increase of θ not obeying mass conservation for that point. Another interesting point of the algorithm is pressure profile strongly depends on different values of θ Dirichlet B.C. Periodic B.C eliminates this depence and for any given reference θ the solution converges the same solution.

Periodic assured by

$$\begin{aligned} \theta_{(1)} &= \theta_{(N)} \\ p_{(1)} &= p_{(N)} \end{aligned} \tag{3.35}$$

and solving $\theta_{(N)}$, $p_{(N)}$ in elimination method. As upwind diffrance is used for θ and p, zero gradient is avoided. But the height node h_1 might be used for solving node N. This method for cavitation can be empolyed both in solving LIN and VR.

3.3.3 Pressure Solver

The requirement to solve pressure is to know height and stress integrals shown in Eq.2.52. Stress is computed and steady state solution employed to carry out the integrals and eliminate y depence of the pressure. A standard procedure is to use tri-diagnol matrix algorithm (TDMA) for second order derivative with forcing terms being the height derivative and the stress integrals. The forcing term of TDMA is for Eq.2.52:

$$\begin{aligned} f = \frac{\beta}{2}\frac{dh}{dx} + \frac{d}{dx}\left(\int_0^h \frac{y}{h}\int_0^h\int_0^y \frac{d\tau_{xx}}{dx}dy''dy'dy \quad - \int_0^h\int_0^y\int_0^y \frac{d\tau_{xx}}{dx}dy''dy'dy\right) \\ + \frac{d}{dx}\left(\int_0^h \frac{y}{h}\int_0^h \tau_{xy}dy'dy - \int_0^h\int_0^y \tau_{xy}dy'dy\right) \end{aligned} \tag{3.36}$$

With the introduction of cavitation, Gauss-Seidel iterative method is employed with switch function θ. One can use same finite difference scheme given for LIN equations. Calling τ_{xx} and τ_{xy} integrals as $I^{(11)}$ and $I^{(12)}$ respectively one can obtain pressure at node i by:

$$p_i = \Big\{ h_i^3\theta_i p_{i+1} + h_{i-1}^3\theta_{i-1}p_{i-1} \\ - 6\Delta x[(1-\beta)(h_i\theta_i - h_{i-1}\theta_{i-1}) - 2(\theta_i(I_i^{(11)} + I_i^{(12)}) - \theta_{i-1}(I_{i-1}^{(11)} + I_{i-1}^{(12)}))] \Big\} \\ \Big/ \left(h_i^3\theta_i + h_{i-1}^3\theta_{i-1}\right) \tag{3.37}$$

The θ solution is given as:

$$\theta_i = \frac{h_{i-1}^3\theta_{i-1}(p_i - p_{i-1}) - 6\Delta x h_{i-1}(1-\beta)\theta_{i-1} - 12\Delta x\theta_{i-1}(I_{i-1}^{(11)} + I_{i-1}^{(12)}))}{h_i^3(p_{i+1} - p_i) - 6\Delta x h_i(1-\beta) - 12\Delta x(I_i^{(11)} + I_i^{(12)})} \tag{3.38}$$

Similar convergence rate is used, $E_p = ||\theta_{new} - \theta_{old}|^2 + |p_{new} - p_{old}|^2|$, it is smaller than 10^{-12}.

3.4 Simulation of EHL

The elastic kernel is constructed and ready to be used by the computed pressure. The pressure solvers are introduced. It is time for combining elastic solver and fluid solver. Start the procedure regarding Fig.3.1, by initializing the height, with a given minimum height. First loop is the displacement solver to obtain a displacement distribution. It is straightforward to apply Eq.3.2 as elastic kernel and pressure is known, so displacement is $\delta = Kp$. At this point relaxation is used as $\gamma^D = 0.1$ to accelerate the simulation. Another relaxation procedure is applied known as Aitken acceleration [106]. The residual is calculated as $r_{new}^d = |\delta - \delta_{old}|/\delta_{old}$ for all nodes. A new relaxation parameter is constructed by following expression:

$$\gamma_t^D = \gamma^D \frac{(\boldsymbol{r}_{old}^d(\boldsymbol{r}_{old}^d - \boldsymbol{r}_{new}^d)')}{(\boldsymbol{r}_{new}^d - \boldsymbol{r}_{old}^d)(\boldsymbol{r}_{new}^d - \boldsymbol{r}_{old}^d)'} \tag{3.39}$$

where transposes are required to carry out the computation and use new relaxation parameter with predefined $\gamma_{min}^D = 10^{-2}$ and $\gamma_{max}^D = 10^{-3}$:

$$\gamma_t^D = min[max[\gamma_t^D, \gamma_{min}^D], \gamma_{max}^D] \tag{3.40}$$

This relaxation parameter is used for that loop and the displacement is updated by $\boldsymbol{\delta}_{new} = (1-\gamma_t^D)\boldsymbol{\delta}_{old} - \gamma_t^D\delta$ and subsequently the height is $h_{new} = h_o + \delta_{new} + S(x)$. One should care the sign of the displacement where it can change by the direction of y axis. The new height is given as initial condition to pressure solver along with the earlier computed pressure p and fluid film fraction θ which accelerates the convergence of pressure solver extremely faster. Saying that, relaxation for pressure is not employed as it is fast enough with given I.C of earlier results and γ^D can be changed for very high loads or low speeds to prevent oscillations. Lastly, the error convergence of the displacement loop is 10^{-6} being enough for the most of the time.

The second loop is the load balance to ensure that the generated load is satisfies the applied load. A new minimum height is defined by with relaxation procedure $h_o^{new} = (h_o + \delta_o)(\frac{F_{new}}{F})^{\gamma^L} - \delta_o$ where $F_{new} = \int pdx$ and "o" donates the center of the channel for the displacement. The relaxation parameter $\gamma^L = 0.5$ for this simulation and the error bound is limited by 10^{-3} which is good approximation. The loop end with defining new height with a new minimum height h_o and a displacement vector δ to start a new loop until the pressure, the displacement and the load are converged.

The numerical methods we require for a isoviscous HL and EHL regime is told in this section where numerical schematic is depict in Fig.3.1. Elastic kernel construction is shown by a small example with figures. The kernel can be expanded

for larger systems easily, for our simulation setup, up to 501 nodes. Then two pressure solvers are examined for non-Newtonain viscoelastic fluids. LIN is easy to implement thanks to linearization and employed with basic finite difference schemes. VR requires to solve transient problem of the polymeric stress in two dimensions. First approach is to create 2D mesh and mesh transform to proceed derivatives. Second approach is to estimate stress as a polynomial in height direction and carry out the calculations just in across the channel. Lastly, the methods are combined to get a full EHL solver.

Chapter 4

Results

4.1 Validation of Numerical Methods

In this section, validation of the developed numerical models are presented before introducing the primary results. First, in Sec.4.1.1 cavitation model is compared with Gamaniel et. al. for multi pocket channel as a benchmark problem. The second section Sec.4.1.2 validation will be the examining mass conservation for a typical EHL contact and grid test is conducted. Thirdly, the LIN algorithm is tried without non-Newtonian effects and compared by the regular Newtonian flow with elastic deformation in Sec.4.1.3.

4.1.1 Cavitation Model

The cavitation LIN algorithm is proofed with other studies and showed by Gamaniel et. al [100]. Thus, in the theses a multi pocket channel validation is studied. The

channel profile and pressure given such:

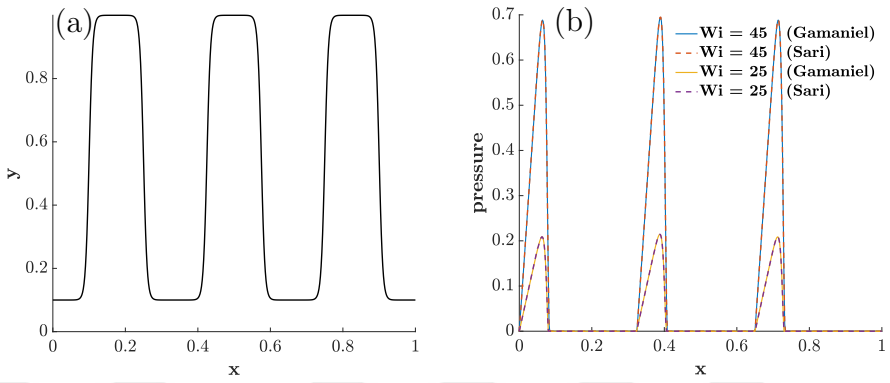

Figure 4.1: (a) Multi-Pocket channel profile (b) results for $Wi = 45$, $Wi = 25$ and $\beta = 0$ with Gamaniel half-step backwards, Sari full-step backwards finite difference scheme

The simulation is applied for different Deborah numbers. The results are compared in the Fig.4.1(b), and observed that the curves matches. Small note that, a half step is used by [101], [100] in height discretezation different than Eq.3.4. However, the pressure and cavitation locations are calculated same. In fact, in the paper, Gamaniel presents results with $Wi = 50$ but it is incorrect. It should be $Wi = 45$ to match the pressure curves similar to Gamaniel et. al..

VR cavitation is also compared with the LIN for smaller De/Wi numbers as the linear theory valid, tough, it is expected that LIN overshoots pressure. Another regular profile is selected to compare VR cavitation with LIN.

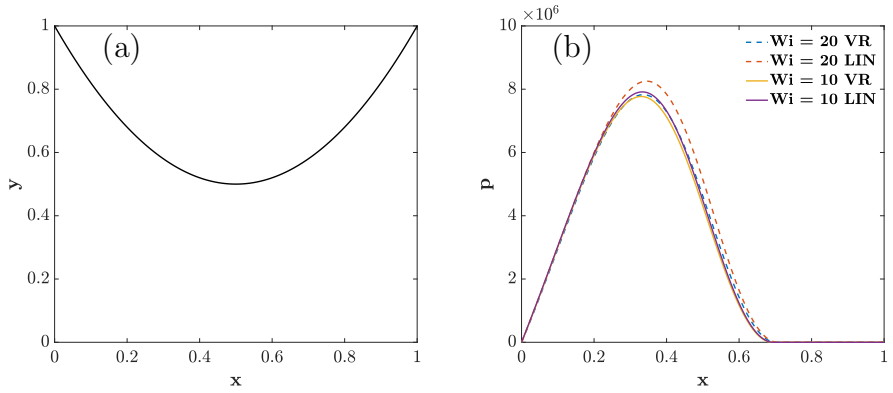

Figure 4.2: (a) the height geometry (b) VR-LIN comparison for $Wi = 10$ and $Wi = 20$ with $\beta = 0.6$

Observing Fig.4.2 we see that for smaller Wi , VR and LIN solutions are quite similar and cavitation location is same, validating VR cavitation. For $Wi = 20$, LIN peak pressure continues to increase whereas VR peak pressure tends to increase less which is expected.

4.1.2 Mass Conservation

The claim of Elrod-Adams to be providing mass conservative numerical algorithm where reforming film accounted for. The mass balance is required to test the validation of the discretezation of pressure equations. The mass balance is specifically calculated for EHL contact and grid dependence is measured.

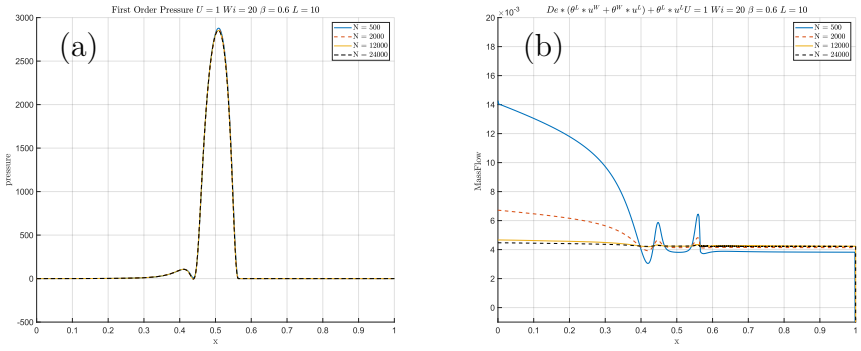

Figure 4.3: The grid test of the mass balance and pressure for an EHL contact

In Fig.4.3, four different grid used to calculate grid dependence. The grid dependence is measured with the change of the pressure. In Fig.4.3a, the peak pressure are slightly changes but for inlet and outlet pressure pressure remains nearly same. Checking Fig.4.3b we can see the mass balance for different grid points. The mass should be conserved and be a linear line in theory. As we increase grid points mass balance gets closer to the theoretical mass flow. However, decreasing mass balance error has no clear effect on pressure calculation. Thus, we are ensure that, the numerical scheme is correctly applied. Regarding grid study, we stick to use 501 nodes for the remaining work.

The mass balance has the error at the inlet of the channel due to small pressures amplifies the difference. However, the mass balance difference is not quite effective for changing the pressure. In deep calculations, I obtained 1 percent error that mass balance is approximately equivalent of 0.01 percent error in pressure. Thus, mass balance is more sensitive to the grid whereas the pressure can assumed to be have grid independence after reaching 500 nodes.

4.1.3 EHL Validation

Last step in validation is to compare Newtonian results obtained from regular Newtonian pressure with Reynolds condition and cavitated LIN algorithm. By setting $\beta = 1$ we can ensure that there is no polymer in the flow or we can set $De = 0$ to eliminate relaxation effects for any β. The obtained results for a setup $\Gamma = 3.75 \cdot 10^{-11}$ and $W = 0.014$ is given with comparison:

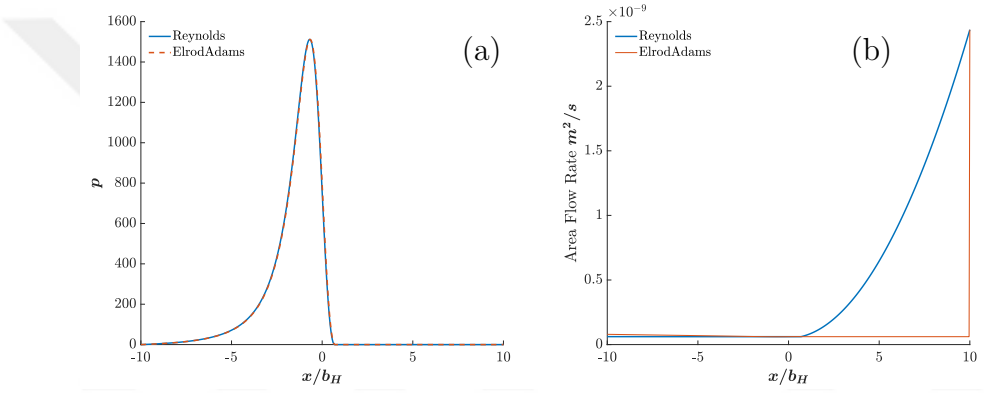

Figure 4.4: The EHL validation with Reynolds condition and LIN (a) for pressure (b) for mass flow rate with De = 0

The obtained results for pressure and mass balance is shown in Fig.4.4. We can observe that pressure is exactly same for both of the case and cavitation location is same. Fig.4.4b, there is a slight difference in the inlet of the channel where Reynolds condition shows better performance but this has a negligible effect on pressure. After cavitation due to θ term appearing in LIN, mass continued to conserve until the end node. At the end node, pressure boundary condition and θ boundary condition are not match but this do not effect solution as pressure B.C is set by Dirichlet.

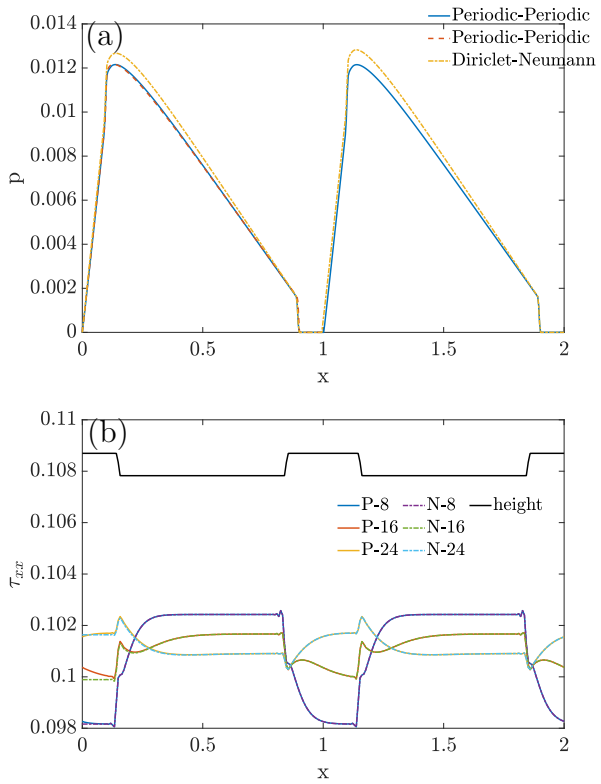

Figure 4.5: (a) Pressure compared for various cases. First column of legend is for pressure and second column represent stress B.C. (b) Normal stress τ_{xx} at various heightes and scaled channel profile.

4.1.4 Periodic Boundary Condition

The periodic boundary condition introduced in numerical methods Sec.3.3.2, is validated by using in cavitation case in pocket-like channel. The correct calculation for fluid film fraction is the critical as the variation of θ can postpond the loacation of full film reformation. The numerical method is validated by manually coping the channel in x-direction periodically. Dirichlet (D) B.C for pressure and zero gradient Neumann (N) to stress is applied for periodicity of two and the results is compared with the both periodic B.C on pressure and stress.

Observe Fig.4.5(a), for solid blue line and dotted orange line matches quite well for both periodic condition applied on pressure and stress. Blue curve is the solution for the channel of periodicity two where orange curve is just solved for one channel. The yellow curve is the result for Dirichlet pressure and zero gradient Neumann B.C. The reason of higher pressure for yellow line can be explained due to the periodic stress. The polymeric stretching is keeped consistent at the inlet of channel that tends to decrease pressure. Fig.4.5(b) shows that normal stress continiues to decrase at inlet for periodic B.C. The gradient of normal stress is a strong indicator of pressure rise or decrease refering to Eq.2.52. Conserving polymeric stress at the inlet has an also effect on refilm location. Realize that in Fig.4.5(a), blue curve reforms later than the yellow curve due to preservation of relaxation of stresses.

4.1.5 Runge Kutta and Crank Nicolson

There are two methods for solving VR, semi-implicit or explicit. This section evaluates the performance of the two methods and also compare the accuracy. There is no well comparison for measuring accuracy in literature except for Humayun & Luca's work. The model needs to be match with results of De (or Wi) numbers computed by LIN. Thus, the models are validated on low viscoelasticity, then the accuracy is tested by comparing two methods by theirselves. The discussion about Pipkin space and eccentricity is covered in following chapters.

An exact parabolic slider used in Humayun & Luca is used for this setting with $\beta = 0.8$ whete the parabolic slider height and the boundary conditions can be obtained. In Fig.4.6 the results are provided for Linear solver, regular Reynolds Solution, Runge Kutta with (512x32) nodes, Crank-Nicolson with (512x32) nodes and polymeric solver granted from Humayun. In their study, ϵWi is used for De, where the result is shown for Wi.

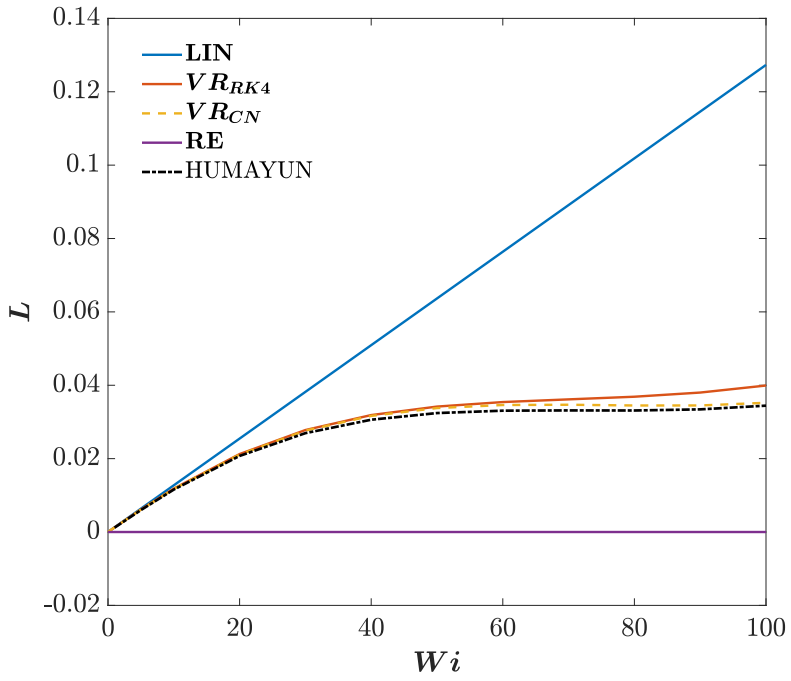

Figure 4.6: The generated load for various numerical approaches and comparison with (Ahmed&Biancofiore 2021)

The load figure can provide us with validation for both pressure and stress solvers. Checking the VR lines we observe that the lines match with LIN for small Wi. Around $Wi = 20$ we expect an exact separation of LIN and VR. Until $Wi = 50$ the lines are matching and the errors seem small. However, for even larger Wi, Runge Kutta loses accuracy compared to the other solvers. This might not be the accuracy problem of the RK4 due to fact of HWNP. The solvers can mesh dependent for large Wi numbers and the lose of accuracy cannot be avoidable.

Thus, we can conclude that semi-implicit method is superior in terms of calculation speed and accuracy even large Wi. The other case we should think of is the high eccentricity parabolic curves for testing numerical methods. However, one should note that time step is need to be well-tuned for superior speeds by CN solver. For several geometries (i.e steep parabola), RK can show better performance.

4.1.6 High Eccentricity and Deviation of LIN

In context of lubrication eccentricity is defined by the position of the bearings in closed bear cap. Call the R_i as the radius of the inner cylinder and R_o is the other cylinders radius where there is a distance difference Δe between their center points. Then, eccentricity is defined:

$$e = \frac{\Delta e}{R_o - R_i} \tag{4.1}$$

In mathematical context, eccentricity is the measure of a curvature, ∞ represents a straight line, 0 being a dot. Using this logic and combining with lubrication context, eccentricity is defined how the surface curved for a limited domain. IN this study, the bottom surface is always flat. The upper surface can be cosine-slider, parabolic slider etc. The appropriate way of defining eccentricity, thus rely on the difference between the minimum height and maximum height ratio for any curved surface. Because the

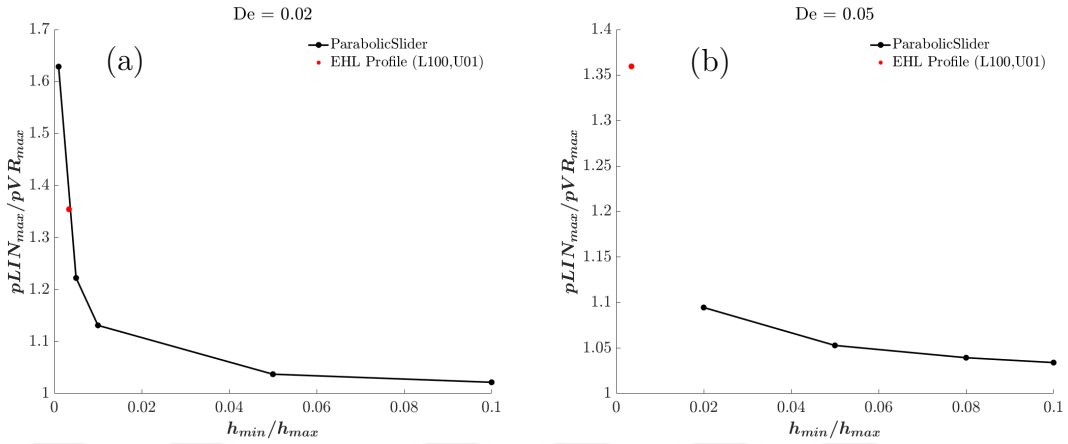

Figure 4.7: The deviation of maximum pressure between LIN and VR for different eccentricity ratios, the EHL eccentricity is indicated by red dot for specific parameters (a) De = 0.02 (b) De = 0.05

bottom surface fixed in length, this ratio indicates the eccentricity of the top surface.

$$e = \frac{h_{min}}{h_{max}} \tag{4.2}$$

By taking into consideration Eq.4.2, the EHL surface eccentricity is measured by $e = h_0/(1/R + h_0)$ where R is being the radius of the top surface and h_0 is the minimum height. For $R = 0.02$ the minimum eccentricity evolves as $e = 50$ and for a minimum height defined blow 1 increases the ratio immensely. Considering this in mind, there need a validation of our numerical methods for high step surfaces. Thus, a comparison between LIN and VR is a necessary to determine an error inbound. For a parabolic slider with different eccentricities, this is tested for different Deborah numbers. The results are shown in Fig.4.7

We can compare the accuracy of EHL by following parabolic slider curve. For Fig.4.7(a),expected deviation between VR and LIN peak pressures are below 10 percent down to the $e = 0.05$. For decreasing eccentricity, the deviation is increases

very quickly and the difference can reach to 70 percent difference for $e = 0.001$. For the eccentricity given in EHL case, the difference between VR and LIN about 35 percent difference. In Fig.4.7(b), for higher De, we do not observe any significant change in the deviation more than slight increase. Though, it is not possible to get solution for more curved surfaces due to strict limitation in stability of the numerical methods.

As a conclusion of this section, the LIN has a good approximation for the eccentricities below $e = 0.01$ for a large range of Deborah numbers. In case of EHL surface, LIN overestimates the pressure and generating more load. We can claim that LIN approximation for the EHL configuration include severe accuracy problems as the high load estimation changes minimum thickness. Minimum thickness is the crucial aspect for measuring the performance of the lubricant in EHL. However, LIN solvers is the adequate preference due to speed in EHL. If a numerical stability is ensured, VR can obtain solution in hours of calculation for one pressure solver loop thus, EHL solver cannot utilize the direct solution of stress. The possible recommendations and comments for employed numerical solvers are given in Sec.4.2.

4.1.7 Validation of VR in steep geometries

The contraction and the expansion geometries include high gradients in the vicinity of the step. This abrupt change in height violets the mass conservation, subsequently Reynolds equations. Instead of using direct step, to apply thin film approximation $tanh$ function with curvature is selected. Using $tanh$ do not alter the outcome pressure and abrupt height change shows affects in the flow. However, the $tanh$ needs validation due to high gradients at contraction location.

The VR results is validated by rheoFoam for several different De/Wi numbers in $tanh(60)$ height profile at different locations of contractions. By DNS result it is also

observed that for $\epsilon = h/l = 0.004$ the thin film approximation holds for $tanh(60)$ but when the curvature is increased to $tanh(120)$, local pressure gradients forms.

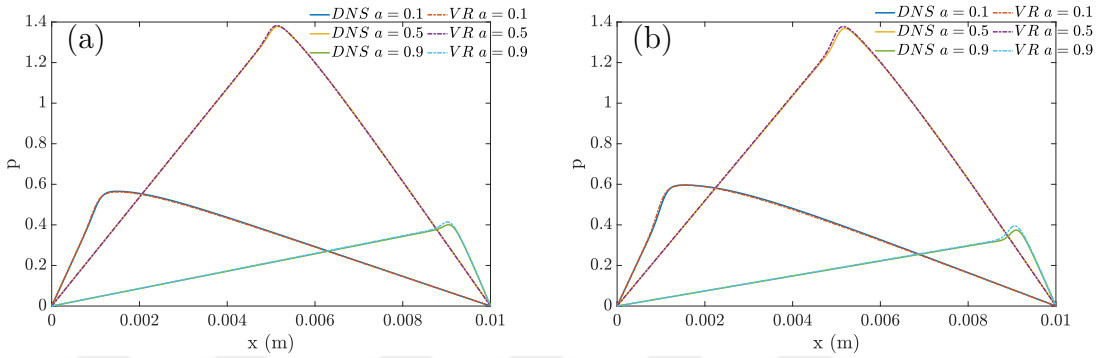

Figure 4.8: The pressure lines for (a) De = 0.1, Wi = 25 (b) De = 0.15, Wi = 37.5, a is the contraction location, the generated load is same under % 1 error

In Fig.4.8, the $tanh(60)$ lubrication profile pressure outcome is shown for DNS and VR. The channel is Coutte flow with bottom part is sliding with constant speed and the top body rigid. The pressure at boundaries are zero ambient pressure where stress is zero-gradient at both sides. Oberserving the figure, the DNS and VR pressures are quite well-matched even for High-Weissenbergs. Despite of small differences shown in contraction locations (espically at $a = 0.9$ peak), the generated load are same.

4.2 Elastohydrodynamic Lubrication Results

The following findings has published in by Sari et. al. [107]. A usual contact geometry for studying EHL is given in Fig.4.9. The initial film thickness is parabolic and given by $h^*(x^*) = S(x^*) + h_0^* + d^*(x^*)$ where $S(x^*)$ is determined via the radius of curvature R of the upper body $S(x^*) = x^{*2}/(2R)$ (a typical EHL profile), h_0^* is the

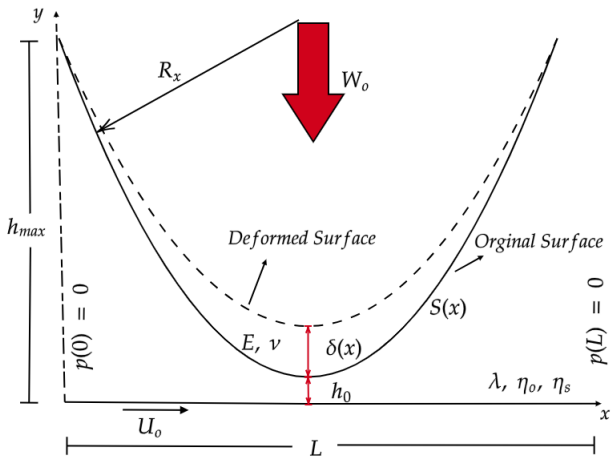

Figure 4.9: The defined contact by given properties

initial central gap, and $d^*(x^*)$ is the deformation. The bottom surface slides with constant speed U_o and the upper surface does not move horizontally. The upper body has a finite elastic module (i.e., a soft surface), while the bottom surface's elastic module is assumed to be infinity (i.e., the surface is non-deformable).

Input Parameters	Definition
L	Length of the channel
U_o	Sliding speed in x direction
V_o	Surface speed in y direction
W_o	Applied load
η_o	Total viscosity
η_s	Viscosity of the solvent
R_x	Reduced radius of curvature
E'	Effective elastic modules
ν'	Effective Poisson's ratio
p	Pressure
λ	Relaxation time of the polymer

Table 4.1: Set of the parameters used in our work

In order to fully define the problem, one needs to know boundary conditions and material conditions. The set of parameters is provided in Table.4.1, to define the problem. In Non-conformal contacts, the length of the channel may vary due to the different loading conditions. Thus, the length is preset with the information about the surface speed and applied load. We assume only the bottom surface moves with speed U_o and the top surface is stationary and there is no relative motion between the surfaces. The inlet and outlet pressure are given as ambient pressure and assumed to be zero. An effective radius of curvature is needed to define the height of the channel. There is no pre-requirement to define polymeric stress in the domain.

For the representation of our results, the domain length and generated pressure are normalized by the Hertzian semi-length b_H and the Hertzian pressure p_H, respectively. Also, the film thickness is normalized with the Newtonian solution

center height, annotated as h_{ref}. Note that, in our study of EHL, $\beta = 0.6$ if it is not stated otherwise.

The other non-dimensional numbers describing EHL are (i) Γ, the speed parameter, which is the ratio between viscous forces and elastic forces, $\Gamma = \eta_o U_o / ER$ and (ii) W, the load parameter, which compares the applied load to the elastic forces, $W = W_o / ER^2$. Lastly, another non-dimensional parameter, i.e., the Hersey number $He = \Gamma / W$, will be introduced in Sec. 4.2.2, which is typical of lubrication problems [108].

In the first Sec.4.2.1, the pressure and film thickness are compared for different W and Γ by different Deborah numbers. Afterwards in the same section, we evaluate the friction and the friction coefficient defined as in Eqs. 2.55a and 2.58. Our discussion continues in Sec.4.2.2 by examining the viscoelastic effects in the function of the Hersey number.

4.2.1 Film thickness and pressure distribution

Fig.4.10a illustrates the film thickness for different De, where the x-direction is scaled with the Hertzian semi-width. As the Deborah number increases, the gap height also increases, and the deformation distribution changes. In the Newtonian case ($De = 0$), the deformation is not symmetric, and the minimum point is located at the end of the narrow gap. However, when viscoelasticity is introduced into the fluid, the minimum point shifts towards the center, with a subsequent increase in the minimum thickness.

Fig.4.10b shows the pressure distribution for the same cases of Fig.4.10a in the middle of the domain (i.e., between $[-3b_h, 3b_h]$) where the deformation occurs. There is a clear change in the cavitation boundary since it shifts towards the outlet of the channel as viscoelastic effects become stronger. This is consistent with the

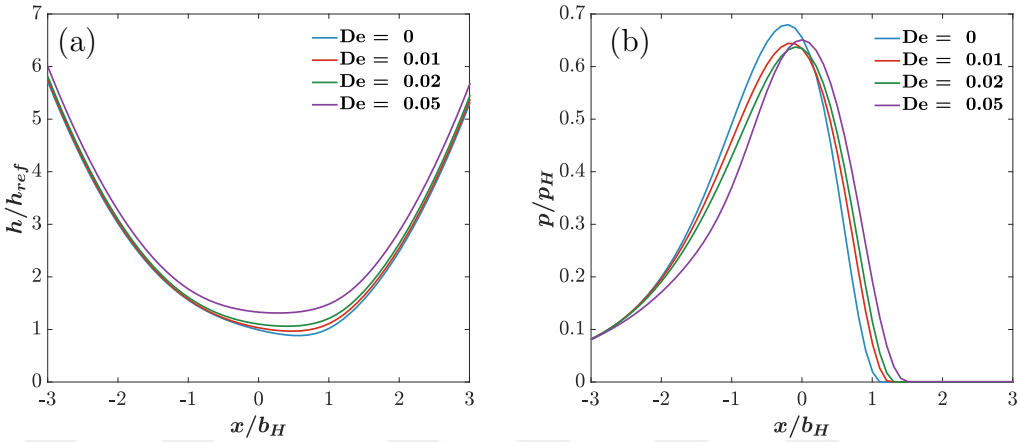

Figure 4.10: (a) The gap between the solid surfaces and (b) the pressure for different De for $\Gamma = 3.75 \cdot 10^{-8}$ and $W = 1.7 \cdot 10^{-2}$.

results of Gamaniel's *et. al.* [100]. Since the cavitation boundary expands, the peak pressure location shifts downstream allowing for more symmetrically distributed deformation on the solid. As viscoelasticity strengthens, the peak pressure slightly decreases initially, while at high De there is a change in trend since it starts to increase. The change in deformation observed in Fig.4.10 can be explained by analyzing the contributions of the Newtonian and non-Newtonian pressures. In Eq.2.42, the Newtonian pressure builds up in the converging part of the channel, and the solution is consistent with the classical lubrication problems. However, in Eq.2.48, the derivatives of the profile may play a significant role in determining the first order pressure generation, leading to strongly profile derivative-dependent non-Newtonian pressure. Additionally, increasing the film thickness reduces (reinforces) the contribution of the Newtonian (viscoelastic) to the total pressure. Further details of the underlying physics will be discussed in Sec.4.2.3.

Fig.4.11 displays the ratio of the peak of the non-Newtonian pressure ($De\ p^{(1)}$) to the peak of the total pressure (p^T) for various Deborah numbers. The upper figures (Fig.4.11a-b) represent large-scale conditions corresponding to high speed

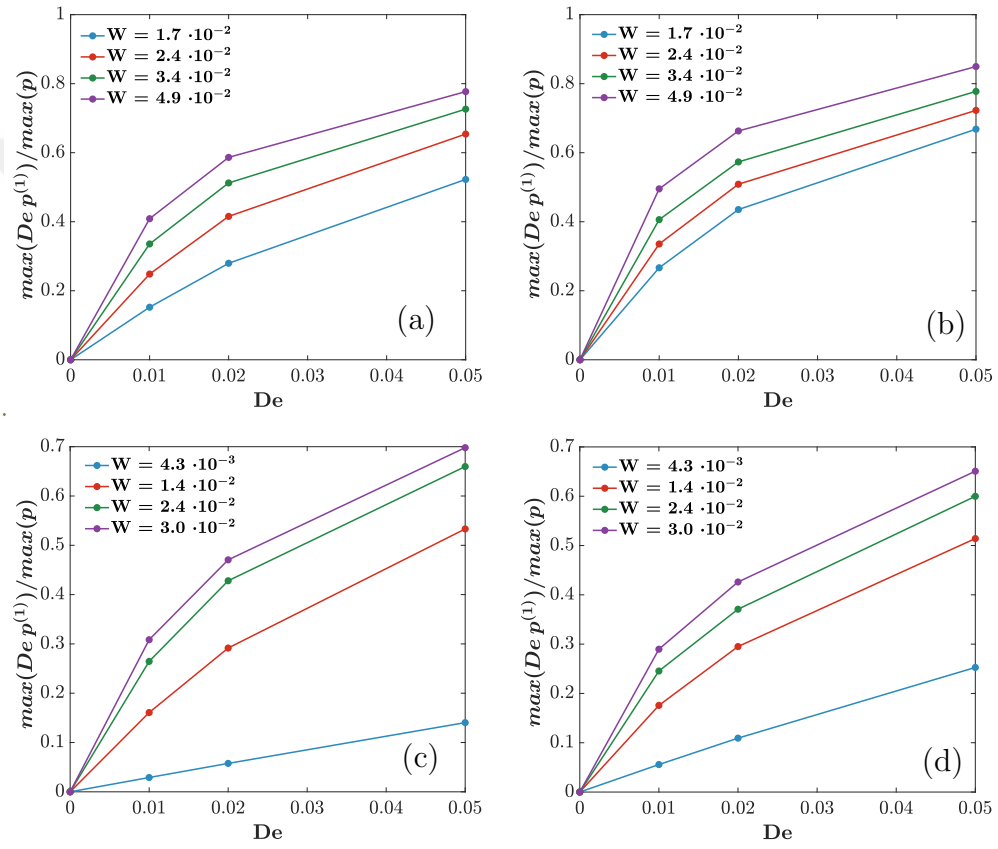

Figure 4.11: Ratio of the viscoelastic peak pressure to the total peak pressure for (a) $\Gamma = 3.75 \cdot 10^{-7}$, (b) $\Gamma = 3.75 \cdot 10^{-8}$, (c) $\Gamma = 1.19 \cdot 10^{-9}$, and (d) $\Gamma = 3.75 \cdot 10^{-11}$.

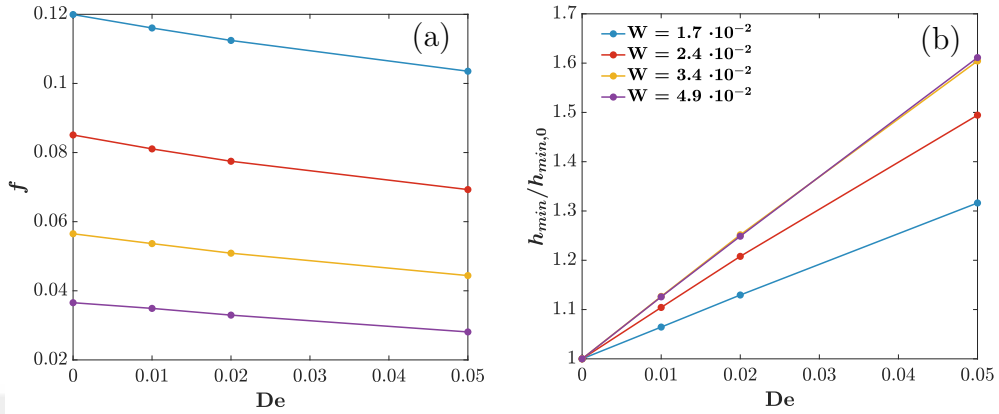

Figure 4.12: For fixed $\Gamma = 3.75 \cdot 10^{-7}$ the effect of different W with increasing Deborah number where (a) friction coefficient (b) the scaled minimum height scaled with $De = 0$.

and load parameters, while the bottom figures (Fig.4.11c-d) correspond to small-scale conditions with relatively low speed and load parameters. In the small-scale analyses, it can be observed that the viscoelastic pressure increases linearly for smaller loads. However, as the load increases, the viscoelastic effects become more pronounced, leading to a significant jump in the ratio between the peak non-Newtonian pressure and the peak total pressure. It is important to note that the effect of the load on viscoelasticity cannot be directly formulated. A similar observation can be made for the speed parameter. An increase in entrainment speed also leads to an increase in viscoelasticity. However, this relationship is not directly linear. Instead, the effect of the speed parameter on viscoelasticity is more complex and depends on other factors that will be discussed later in Sec.4.2.3.

In Fig.4.12, (a) the friction coefficient and (b) the ratio between the non-Newtonian and the Newtonian minimum film thickness ($h_{min}/h_{min,0}$) is depicted for different load parameters in function of the Deborah number. The friction coefficient consistently decreases for each load parameter as De increases. In Fig.4.12b, the minimum film thickness ratio is shown. The film gap increases by up to 60% at the highest Deborah number ($De = 0.05$). It is evident that at higher loads - for a fixed

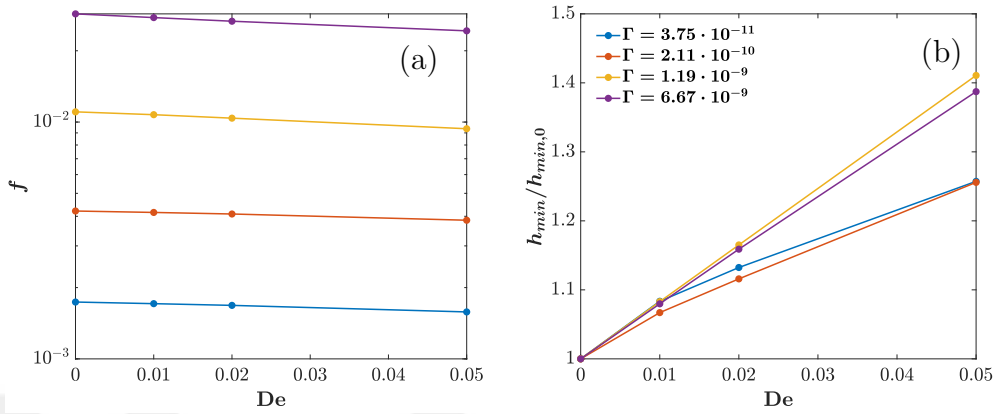

Figure 4.13: For fixed $W = 2.4 \cdot 10^{-2}$ the effect of different Γ with increasing Deborah number where (a) friction coefficient (b) the scaled minimum height scaled with $De = 0$.

speed parameter - there is a more pronounced viscoelastic effect compared to low loads, at least up to a certain load value. Beyond this point, the curves tend to match, indicating that the influence of the load on the viscoelastic effect saturates. This behaviour suggests that there might be an optimal load value for which the viscoelastic effect on the film thickness is maximized.

In Fig.4.13, (a) the friction coefficient and (b) the minimum height ratio are shown in function of the Deborah number at different values of Γ. As previously observed, the friction coefficient consistently decreases regardless of the value of Γ. In Fig.4.13b, the curves exhibit a non-linear trend for low-speed parameters. For small Deborah numbers, all curves show a similar increment, but as Γ decreases, the degree of the viscoelastic effect also diminishes. It is important to note that the curves are highly dependent on the load parameter, as demonstrated in Fig.4.12. The influence of viscoelasticity on the friction coefficient and the film thickness depends on both the load and speed parameters in a complex manner and different combinations of these parameters can lead to various outcomes.

In Fig.4.14, the effect of the (a,b) load ((c,d) speed) parameter on the friction

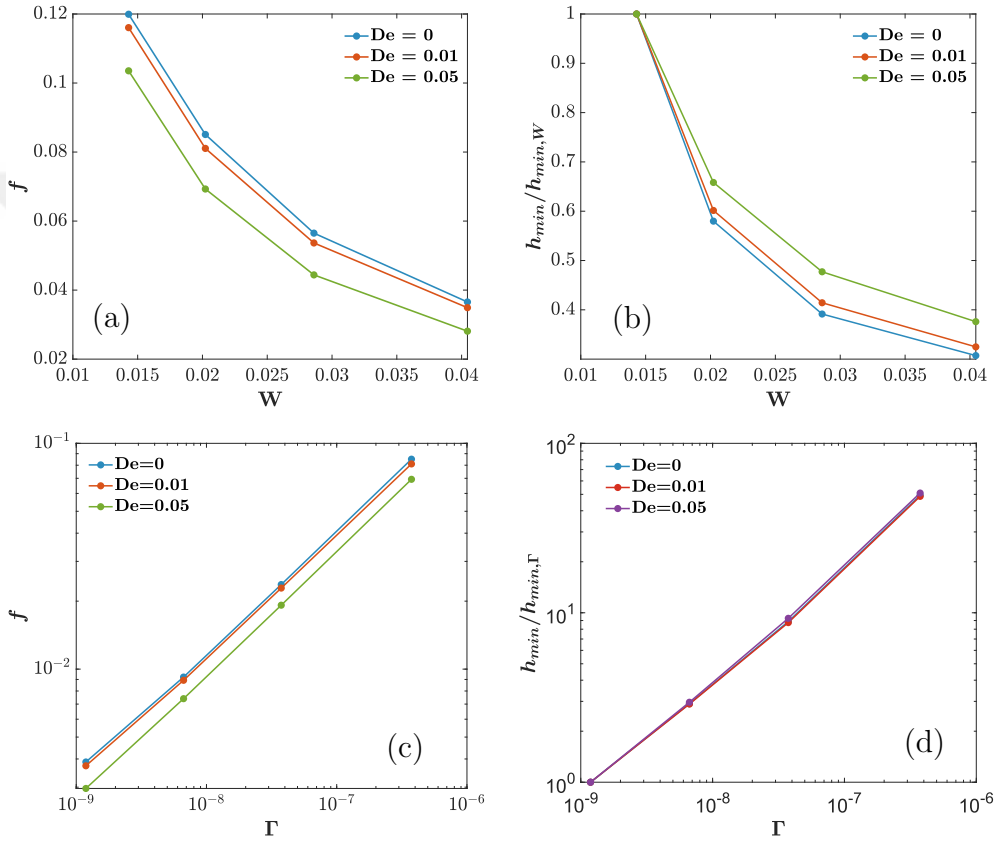

Figure 4.14: (a) Friction coefficient and (b) the minimum height for increasing speeds for fixed $\Gamma = 3.75 \cdot 10^{-7}$ where $h_{min,W}$ is the minimum height taken for $W = 1.41 \cdot 10^{-2}$ (c) Friction coefficient and (d) the minimum height for increasing speeds for $W = 2.4 \cdot 10^{-2}$ where $h_{min,\Gamma}$ is the minimum height taken for $\Gamma = 1.18 \cdot 10^{-9}$.

coefficient and minimum height are observed while setting the speed (load). Starting with Figs.4.14a,b, we note that an increase in the load decreases the friction coefficient as expected in EHL cases. In general, the friction coefficient decreases until the mixed regime starts and then suddenly increases, while transitioning to boundary lubrication [15]. With the presence of viscoelasticity, a clear decrease in the friction coefficient is observed for all the examined loads, coupled with an increase in the minimum film thickness. As the load increases, the upper surface approaches the bottom one and the film thickness decreases as expected. The increment of the film thickness due to viscoelasticity can explain the lower degree of friction.

By varying Γ (Fig.4.14c), viscoelasticity plays a significant role in modifying the value of the friction coefficient with respect to the Newtonian case. The trend of decreasing friction coefficient seems to continue for high Deborah numbers. On the other hand, there is no clear evidence of viscoelastic effects on the film thickness, because the variation of the speed parameter has already a strong influence on the film thickness (Fig. 4.14 d). The minimum gap at the lowest speed (for all De, including $De = 0$) increases up to 60 times for the highest speed parameter (i.e., $\Gamma = 3.75 \cdot 10^{-7}$), where the bodies are fully separated. Thus, we also observe that the presence of viscoelasticity does not always help in increasing the film thickness for the same load value. The effect of viscoelasticity should not be confused with the increment of viscous force in this case. The polymeric contribution does not change the magnitude of the viscous force but shows additional stretching which De measures this additional effect.

4.2.2 Hersey number

In Sec.4.2.1, we discussed the friction coefficient for different load and speed parameters at both small and large scales. To observe the degree of influence of viscoelasticity on the friction coefficient, we need to consider W, Γ and De at the

same time because viscoelastic effects cannot be directly formulated by speed or load alone. To combine all these parameters, we divide the speed parameter by the load parameter for each Deborah number. The ratio of the speed parameter to the load parameter results in the Hersey number ($He = \Gamma/W$), which is another non-dimensional parameter widely used in the context of the Stribeck curve, where it describes the viscous force over the carried load [109].

In Fig.4.15, (a) the minimum height of the channel, (b) the friction coefficient, and (c) the percentage difference is illustrated in the function of the Hersey number. The speed parameter is specifically indicated in the figures to follow the same Γ but with a different W. As the Hersey number increases, both the minimum height and the friction coefficient increase as expected (see Figs 4.15a and b, respectively). A high Hersey number implies a hydrodynamic regime rather than an EHL regime, where solid deformation will not occur. Checking Fig.4.15a, we observe that the values of the minimum film thickness get closer to each other as the load decreases. In fact, the load parameter is the one controlling the thickness of the film. Higher values of W squeeze the channel more, and the load balance is more critical than in hydrodynamic cases because, in the HL regime, the film thickness remains nearly the same. Concluding that, the sensitivity of the film thickness at high W increases the amplitude of the viscoelastic effects. From Fig.4.15b, we can see that even if the Hersey number is similar between two configurations, the different combinations of load and speed parameters can still influence the friction coefficient.

By increasing De, we see an improvement in both film thickness and friction coefficient in each case, where its percentage difference is given in Fig.4.15c. We observe that an increase in He results in damping the viscoelastic effects on the friction coefficient. It is clear that for the case of $\Gamma = 1.19 \cdot 10^{-9}$, where the load parameter is small and, thus we are close to hydrodynamic lubrication, viscoelasticity does not significantly affect the friction coefficient. In fact, previous studies have shown that for hydrodynamic lubrication cases, friction does not significantly change

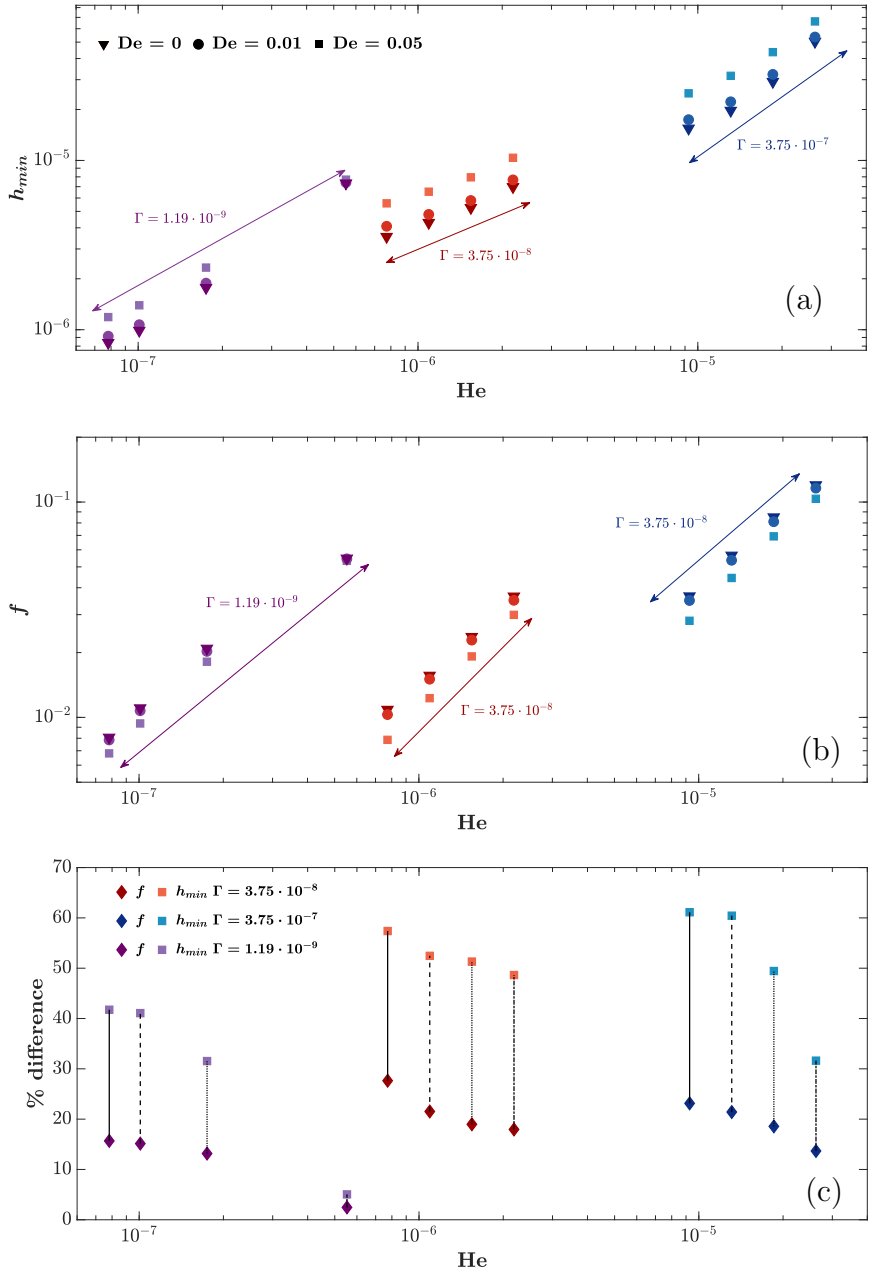

Figure 4.15: (a) Minimum height of the film thickness, h_{min} (b) friction coefficient, f and (c) percentage difference between $De = 0$ and $De = 0.05$ in function of the Hersey number. Each data set is indicated with its speed parameter.

with De [100]. Thus, the decrease in the friction coefficient is directly related to the increase in load carrying capacity caused by viscoelasticity. The increment in the load capacity is an observed phenomenon for hydrodynamic lubrication cases in which the film thickness is fixed [100, 77]. A larger thickness results in a decrease in the friction coefficient, as expected.

4.2.3 Discussions

In this section, a possible physical explanation is provided for the obtained results. The addition of polymers leads to a significant reduction in the friction coefficient, particularly at high Deborah number values, in those cases where the elastic deformation of the solid is dominant. However, this reduction in the friction coefficient becomes less pronounced as lubrication approaches the hydrodynamic lubrication regime, which aligns with previous findings [100]. Notably, the overall load-carrying capacity increases when polymers are introduced, whether cavitation is present or not in hydrodynamic lubrication. This increase in the load-carrying capacity is reflected in the elastohydrodynamic lubrication (EHL) case as an increment in the film thickness, resulting in a higher minimum height. On the other hand, the increase in minimum height leads to a substantial decrease in the contribution of the Newtonian pressure, as evident in Fig.4.11. Although the pressure is primarily generated by the non-Newtonian part of the fluid, the main source of friction is attributed to the Newtonian case. The larger gap created by the polymer elasticity, therefore, contributes significantly to the friction reduction.

To focus more on this point we show in Fig.4.16a, the friction together with the Newtonian friction or zeroth order friction $F^{(0)}$(dashed line), while in Fig.4.16b, the viscoelastic friction or first order friction $DeF^{(1)}$ for different values of W and $\Gamma = 3.75 \cdot 10^{-8}$. In Fig.4.16a, one can see that the order of magnitude of the Newtonian friction is much higher than the non-Newtonian friction. The viscoelastic friction

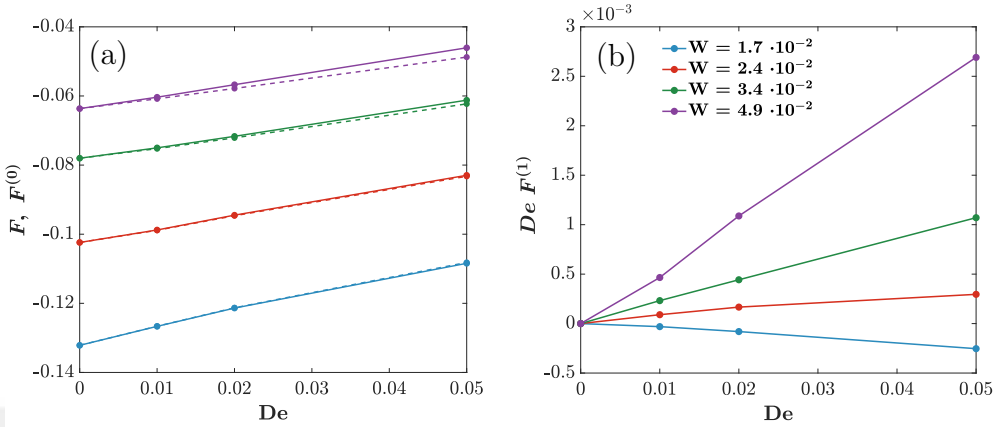

Figure 4.16: (a) Non-dimensional total friction (solid line) and Newtonian contribution to the friction (dashed line) and (b) viscoelastic contribution for different loads with increasing Deborah number at $\Gamma = 3.75 \cdot 10^{-8}$.

is nearly negligible but slightly decreases the friction force. For all but the lowest load, the viscoelastic shear stress shows a positive force. This positive force slightly decreases the overall friction force. Thus, there is also a positive contribution to coefficient of the friction due to the positive effect of shear stress caused in the polymers in higher loads along with the thickness increment.

In Fig.4.17, the Pipkin space for our configuration is presented for $\Gamma = 3.75 \cdot 10^{-8}$. Four distinct load parameters are depicted in the plot. We observe that, as the surfaces get closer due to the higher load, the value of ϵ_0 decreases, leading to higher Wi for the same De. It is also evident that a large De results in a thick gap (i.e., in a large ϵ_0) leading to non-linearity in the Pipkin space. This nonlinearity is indicative of the influence of viscoelasticity on the flow behaviour. Therefore we can conclude that the higher viscoelastic effects noted at high load are due to the larger values of Wi caused by the higher strain rates typical of a thinner gap.

As it is preivously discussed in Sec.2.3 and Sec.4.1.6, high Wiessenberg number is problematic for the accuracy of the models avaible to us. In this high eccentricity, LIN

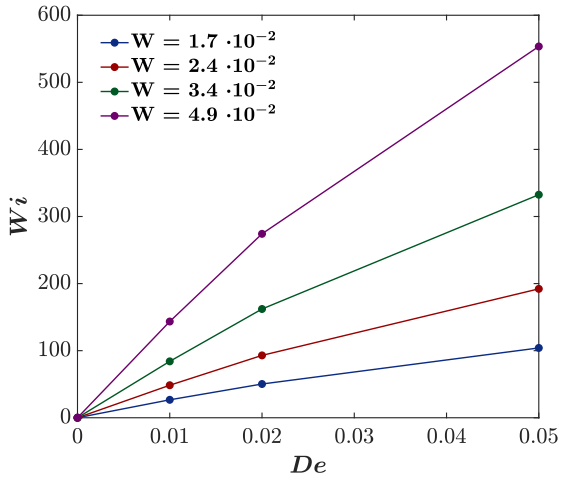

Figure 4.17: The Pipkin space (Wi vs De), for $\Gamma = 3.75{\cdot}10^{-8}$ for different load parameters.

has diffuculties to calculate accurate pressures. However, Fig.4.17 provides crucial information about the De-Wi releationship and sufficient range to use VR.

Another important reveal is that the viscoelastic effects has really impact when elasticity (deformability), W, of the surfaces are high which is visible in Fig.4.15. Also considering the surface curvatures at high W, one may think of the surface curvature due to high deformation, amplifies the relaxation of the polymers. More closer look to the high deformation surface curvature in Fig.4.10. The surface, at the middle turns to a flat channel, $dh/dx = 0$ and expansion of the fluid has postponded. This stage of the channel where the height derivative is zero could be the main reason for enhancing the polymeric elastic stress due to zero exicment forced by surface. In order to examine the effect of the flatness, step like channels are studied to hightlight flatness.

4.3 Contraction Expansion Results

Studies addressing viscoelasticity often entail simplifying models to mitigate nonlinearities or developing numerical techniques to tackle the numerical instabilities induced by its complex nature [110, 111].

The behaviour of viscoelasticity in abrupt contractions and expansion channels is particularly studied to assess model accuracy and computational efficiency, given their simplistic geometries. Such studies often focus on the viscoelasticity effect on changes in pressure and mass flow rate [112, 111]. Additionally, there is attention given to the vortex formation caused by the step change in flow at the lip with increasing Deborah number. Despite numerous studies on pressure drop and vortex formation at contractions or expansions, less attention has been paid to the channel entrance or exit, often assuming fully developed flow conditions [113, 114].

An extended investigation has been conducted to address the entrance problem with Newtonian, shear-thinning, and viscoelastic fluids both experimentally and numerically [115]. Nevertheless, polymer stretching post-contraction and relaxation to its relaxed state prompt further discussion on additional pressure drop. The downstream length significantly contributes to pressure drop, known as the Coutte correction, owing to the relaxation of normal and shear stress. Particularly for larger Deborah numbers, polymer stretching extends towards the exit downstream, necessitating a sufficiently long downstream length to ensure accurate Coutte correction for pressure drop. This extension can disrupt the numerical stability and accuracy of lip vortex predictions [116, 117, 118].

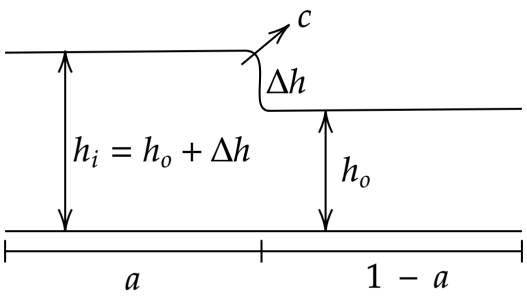

Figure 4.18: The step geometry for variable lengths of a and Δh with curvature c

The comprehensive examination of overall pressure drop throughout the channel has not been explored extensively. Instead, downstream stress relaxation is often addressed through Coutte correction rather than solving for full-scale pressure-velocity coupling. Generally, there is a lack of consensus regarding determining exit channel length for contraction-expansion geometries, except for ensuring fully developed exit conditions. It is also noteworthy that in the assumption of creep flow, discussions about the contraction location for viscoelastic fluids are absent. Particularly, the significant impact of viscoelastic stress on flow dynamics in various thin film contacts and shear flows has not been addressed in earlier studies.

The particular focus of this study lies in examining a thin, straight channel with a small contraction or expansion, as depicted in Fig. 4.18 where a bottom slides with constant velocity and the top surface is not moving. This simple geometry enables the elimination of the Couette term throughout the channel, except at the location of the step. The analytical solution for Newtonian fluids is well-known and provided in the literature [15], resulting in a constant pressure gradient across the channel. By employing a constant mass flow rate, q, the pressure gradients can be solved without considering the impulse induced by the contraction. The same approach will be applied to the non-Newtonian elastic term to observe polymer relaxation and its correlation with the step location.

This simple geometry might help to understand the behaviour observed in Fig.4.15. Higher deformability enables polymers to create more load owing that straight channel ($dh/dx = 0$) at the middle of the lubricated contact. By varying the contraction location the polymer relaxation and its overall effect on load can be observed.

Other studies focuses on contraction consider the inlet effect and ensuring enough length before the step for fully developed flow. We also assume the flow enters the channel fully developed with zero stress gradient. The pressure is set to zero ambient pressure.

We use the mass flow rate of the direct triple integral of the $x-$ momentum equation. The first and second constants are calculated after applying boundary condition for velocity. The overall mass flow rate, q, expressed as:

$$q = -h^3\frac{dp}{dx} + 6\beta h + 12\left(\int_0^h \frac{y}{h}\int_0^h\int_0^y \frac{\partial \tau_{xx}}{\partial x}dy''dy'dy \quad - \int_0^h\int_0^y\int_0^y \frac{\partial \tau_{xx}}{\partial x}dy''dy'dy\right) + 12\left(\int_0^h \frac{y}{h}\int_0^h \tau_{xy}dy'dy - \int_0^h\int_0^y \tau_{xy}dy'dy\right) \tag{4.3}$$

For straight channel, the fully developed inlet stress can be simplified and simply placed by 0 shown in Owens & Phillips [65]. The transported mass flow rate by pressures can also be simplified and separated as viscoelastic and Newtonian for inlet channels.

$$q^n = -h^3\frac{dp^n}{dx} \qquad q^{ve} = -h^3\frac{dp^{ve}}{dx} \tag{4.4}$$

4.3.1 Numerical Results

In this section, the numerical results for Newtonian and VR have shown for different ranges of $\{\boldsymbol{a}, \boldsymbol{\Delta h}\}$. We start from the pressures to observe the effect of polymeric elastic stress on pressure for various contaction locations. Sec.2. Viscolelatic Reynolds has been implemented to solve Olroyd-B equations by the semi-implicit approach Crank-Nicolson.

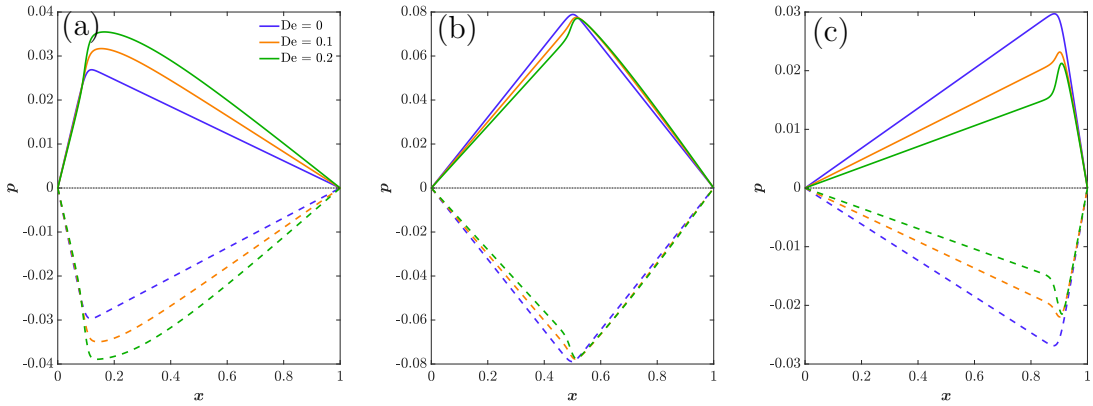

Figure 4.19: The pressures for different locations, $De = 0.1$ and (a), (b), (c) for $\Delta h = 0.03$, (d), (e), (f) for $\Delta h = -0.03$

In Fig.4.19, there are the pressure lines for different methods. The top figures are for contracting geometry (positive Δh) thus, positive pressure is generated where the below plot belongs to a channel that is expanding, leading to negative pressure.

Pressure only generated by viscoelastic stress is given in Fig.4.20. Similar to Fig.4.19 top plots are for contributing geometry whereas bottom plots are for expanding geometry. (b)-(e) contribution of elastic normal stress τ_{xx} to pressure called as p_{xx}, (c)-(f) contribution of elastic shear stress $\tau_{xy} - \tilde{\beta}\frac{\partial u}{\partial y}$ called as p_{xy}, lastly (a)-(d) the summation. For contracting geometry, p_{xx} is linearly decreasing until the step then the polymers extending and changes pressure profile. The same behaviour is also observed for the expanding channel with opposite signs.

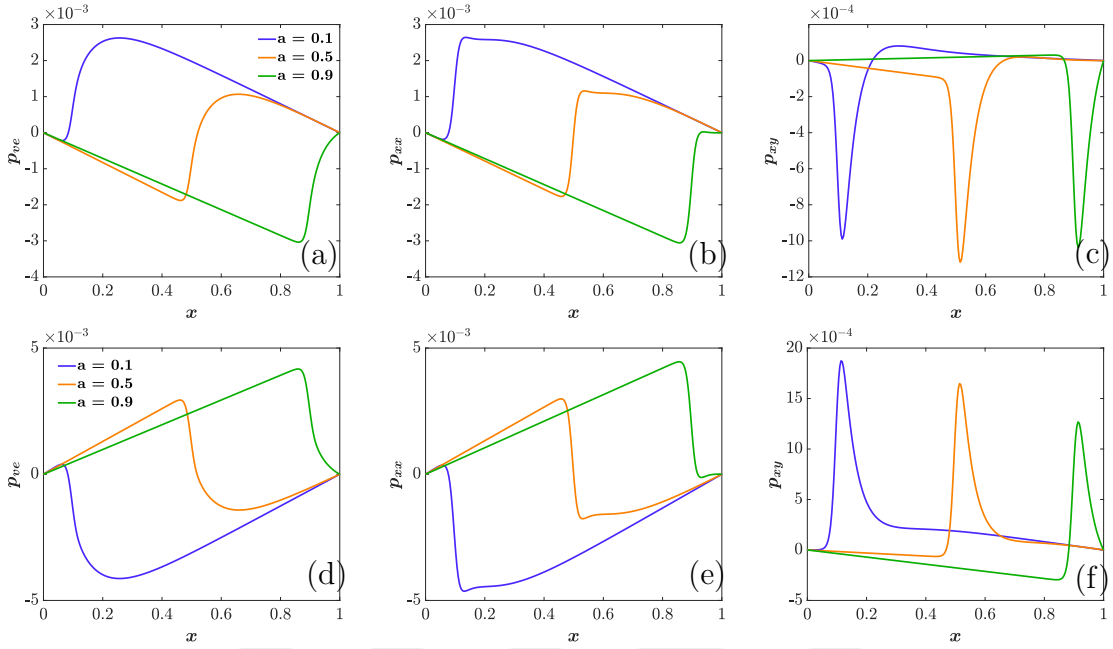

Figure 4.20: The numerical results of pressure contribution by stresses with for different locations a, with ($De = 0.1$) (a) p_{ve} (b) p_{xx} (c) p_{xy} for $\Delta h = 0.05$ and (d) p_{ve} (e) p_{xx} (f) p_{xy} for $\Delta h = -0.05$

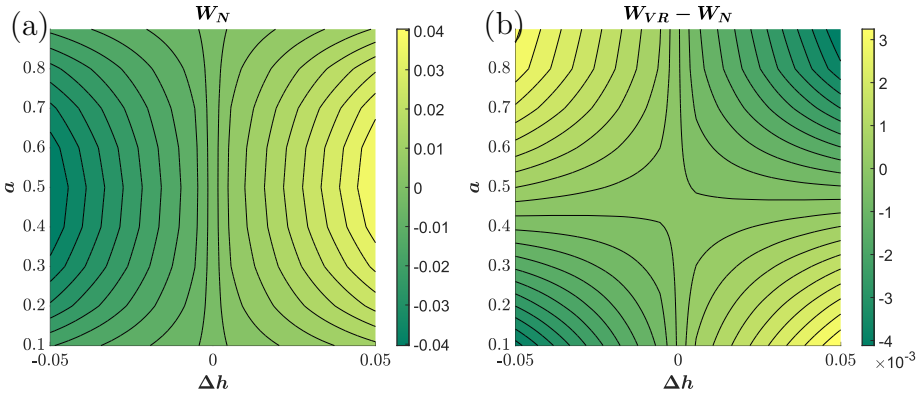

Figure 4.21: The map of load for different a and e values where $\beta = 0.5$ for non-Newtonian cases, ($De = 0.1$), (a) the load by Newtonian (b) the load by VR(c) difference between Newtonian to VR

Our analyses continue with the load map for different step locations a and height differences Δh for Newtonian output Fig.4.21(a) and polymer mixture ($\tilde{\beta} = 0.5$) with $De = 0.1$ Fig.4.21(b) calculated by VR and the difference between loads Fig.4.21(c). Realize that viscoelasticity considerably depends on the step location which can also be spotted by Fig.4.19. Recent studies by Boyko et. al. [119] and Hinch et. al. [120] call attention to the exit and entrance lengths of the channels and their effect on polymer relaxation. This is reflected in the pressure and eventually pressure integrals. Leading to more load when the step is close to the inlet and less load when it is close to the outlet in contraction. Just the opposite in expanding channels.

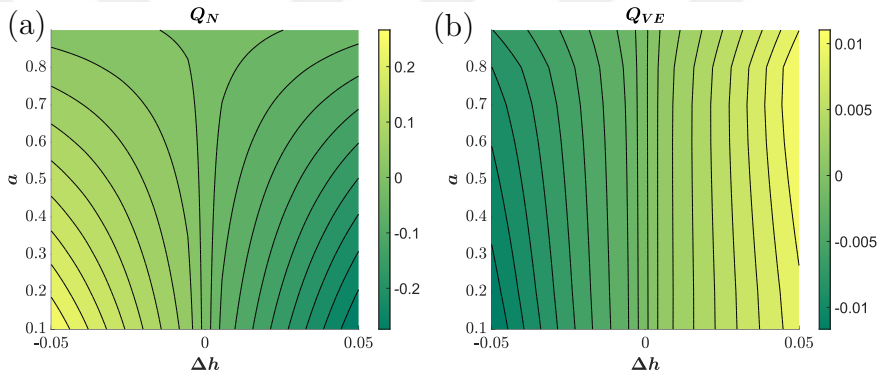

Figure 4.22: Mass flow rate for different locations of steps and height difference, ($De = 0.1$), (a) is Newtonian mass flow rate (b) viscoelastic mass flow rate calculated by Eq.4.4

The step location is crucial for considering the effect of viscoelastic stress on flow. The stress relaxes only when there is a disturbance in the flow, thus the pressure gradients caused by stress remain constant until the step. High velocity gradients at the step impact stress and we see the jumps in pressure and the expansion, compression etc. slowly decay for the rest of the channel. In order to gain more insight into constant pressure gradients caused by viscoelastic pressure, the mass flow maps are given in Fig.4.22.

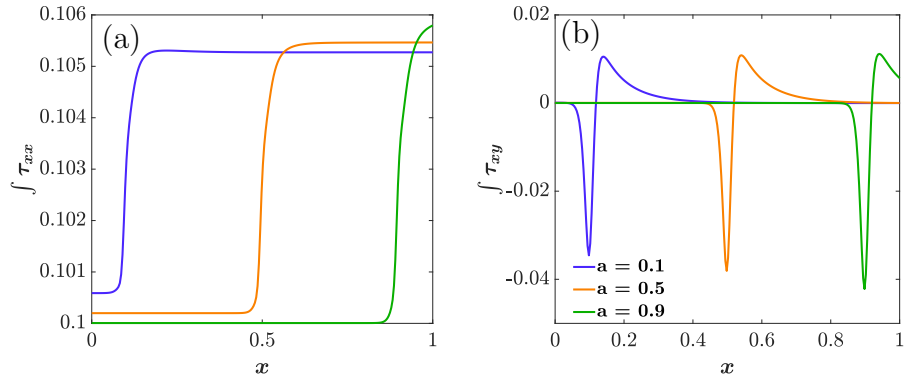

Figure 4.23: (a) $\int_0^y \tau_{xx}$ (b) $\int_0^y \tau_{xy}$ for different locations $De = 0.1$ and the gap is $\Delta h = 0.05$

Fig.4.22 contains the Poissele effect on mass flow and excludes the Coutte part. The Newtonian pressure has a negative transport, so pushing back the fluid in contraction and opposite in expansion. The transportation slowly decays when the step is located at the end of the channel. However, Fig.4.22(b) shows us the viscoelastic transportation and we observe that it is constant for every step location and opposite sign of Newtonian mass contribution. Thus, the elastic stress transports more fluid to the channel in contraction. This aligns with the findings of Boyko et. al. [119]. The transported fluid by the stress is the main factor in decreasing the pressure gradient and vice versa in expansion cases.

The elastic normal stress is analyzed for different channel locations for two different step locations. In Fig.4.23(a), there is enough space for the polymer relaxation after the disturbance. Towards the end of the channel, the normal stress is fully relaxed and during relaxation it has a positive effect on the pressure seen in Eq.2.52. In Fig.4.23(b), the normal stress has not enough time to relax and polymers leave the channel, thus the relaxation has a limited effect on fluid pressure.

Using the outcome of *tanh* profile, we can mimic EHL like channel to validate our assumption. If the height derivative is zero after contraction and delaying the

expansion, elastic stress has sufficient time/length for relaxation and subsequently, alter the generated pressure. This hypotheses is examined for a simple EHL-like channels. The channel inlet has a constant negative dh/dx, zero dh/dx in middle and positive dh/dx at outlet.

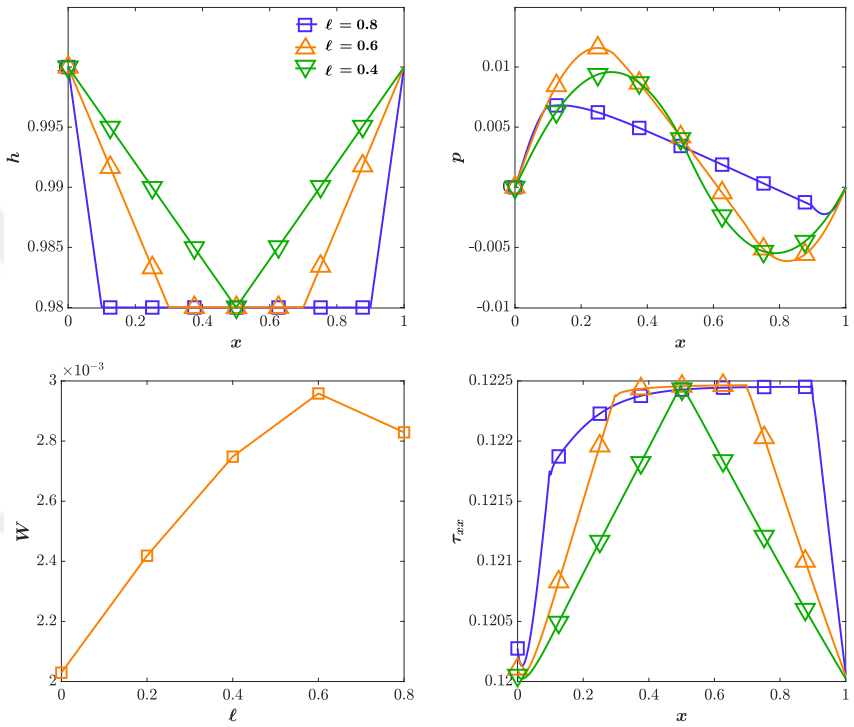

Figure 4.24: (a) channels (b) the pressure (c) the generated load (d) the normal stress, the same color represent same setup

In Fig.4.24(a), the different channels for increasing flat length, Fig.4.24(b) the obtained pressure, Fig.4.24(c), the generated load, Fig.4.24(d) normal stress are shown. The load increases when $dh/dx = 0$ region is expaned aligning our expectations.

Chapter 5

Experimental Work

Despite experiments not being the main goal of this thesis, the three-month study covers viscoelastic fluid theory and measurement techniques. The experimental findings might also reveal the required numerical methods to engage measurement instruments and provide a realistic foundation for theoretical work. Moreover, the three-month study can provide basic information about experimental tools and experience for future work.

5.1 Scope of work and aim

The project aims to compare the effect of polymeric additives on load-carrying capacity due to viscoelasticity in fully film-lubricated contacts, both experimentally and using novel numerical models developed in the last decade. Polymeric additives change the behavior of lubricants, such as shear-thinning, viscosity, heat capacity, etc. This study specifically aims to measure the effect of viscoelasticity exhibited by the polymers on load-carrying capacity in the full film by eliminating other factors.

The objective of the experiment:

- To gain knowledge and experience in preparing polymeric additive lubricants for the objective of experiments
- To gain knowledge and experience on characterizing the fluid properties i.e. relaxation time and zero-shear viscosity
- To measure normal load in lubrication for several different samples with available tools i.e rheometer

To ensure validation of numerical methods, $Wi < 100$, Wi number should lower than 100 because of inaccuracy of models at high Weissenberg number. This is quite known problem called as High Wiessenberg Number Problem (HWNP) [65]. Thus, for speed range which the tools are capable to give stable results are noted as at least 0.01 m/s. A suitable relaxation time than turn out about in the order of maximum 100 ms and lower is accepted at higher speeds.

5.2 Methods

After determining the required relaxation time of the fluid, lubricants can be prepared accordingly. The chosen lubricant might not be well-represented in industrial applications, as the literature often insists on solutions that are easier to prepare in a laboratory setting. Early studies focused on PIB/PB/C14 mixtures for relatively large relaxation times of up to 2 seconds with thicker fluids [121, 115, 113]. In the 2000s, polyethylene oxide (PEO) became a popular polymer choice due to its water solubility and ability to induce relaxation times on the order of 1 ms. Thus, PEO is selected as the polymer of choice, having been validated and used in the literature for 20 years [122, 123, 124, 125].

PEO solutions are mostly prepared with a water/glycerol mixture. The reason for adding glycerol is to increase the viscosity of the solvent. Since water has very low viscosity, (i) the lubrication performance might not be sufficient to observe the net load, and (ii) characterizing the low viscosity fluid is much harder in a rheometer due to Taylor instabilities and high Reynolds number. Glycerol helps increase viscosity without disturbing the PEO-water mixture, thereby eliminating inertial effects.

5.2.1 Sample Preparation

An example solution consists of 85% water, 15% glycerol, and 0.075% PEO coded as (WG15PEO075). For 50 grams of fluid: 42.5 grams of water, 7.5 grams of glycerol, and 0.038 grams of PEO:

- Mix water and PEO first with low-speed stirring [126] for at least 12 hours [127, 124]
- Add the required glycerol
- Stir the mixture for long hours [124] before conducting experiments.

It is reported that PEO solutions are very sensitive to degradation over time due to light and polymeric instability. Over days, PEO degrades, causing the solution's viscosity to decrease considerably [128]. It is also observed in our solutions that the viscosity is quite dependent on the preparation stage and time. Therefore, the solutions should be stirred well and used immediately without waiting.

5.2.2 Viscosity Characterization

In literature, steady shear rate measurement in rheometer [122, 129] and Ubblehodde viscometer [123, 125] are popular choice for measuring viscosity. We used (i) rheometer cylinder steady shear test (ii) Stabinger viscometer. Note that, provided data here is without stirring the solution in pre-use. The present results are prepared with $2 \cdot 10^6 M_W$ PEO by Sigma Aldrich in white powder form.

Rheometer (Anton Paar 312-M) Test

- Rheometer data is available at 25C for: DI Water, WG15, WG15PEO075, WG85, WG85PEO075 with critical Taylor number. There is also a critical line for low shear rates where motor torque limits measuring viscosity at low shear rates [122].

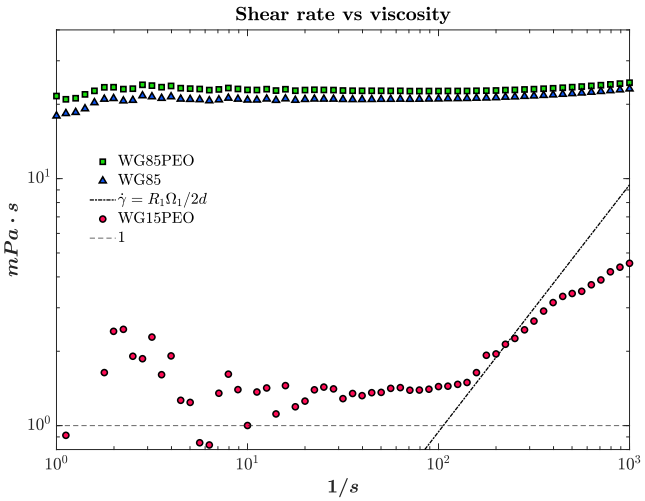

Figure 5.1: Viscosity of several solutions with high glycerol

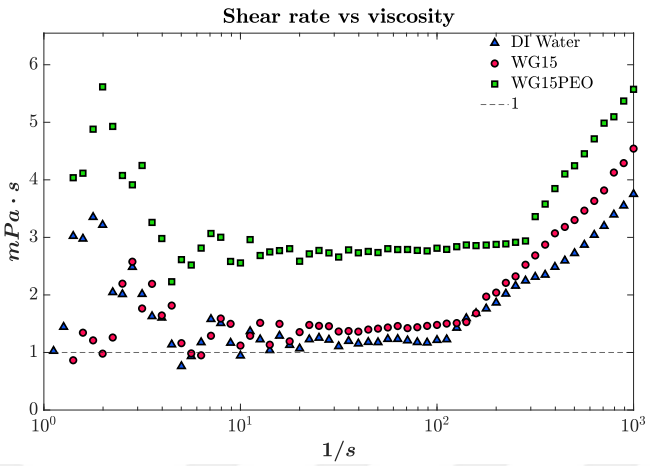

Figure 5.2: Viscosity of several solutions with low glycerol

- 1. Observation: The measured viscosities (Fig.5.1 & Fig.5.2) do not match with Rodd 2007. Also, for DI Water at 25°C the expected viscosity is 0.9 mPa.s whereas in rheometer it is 1.1 mPa.s.

  2. Observation: Adding polymers to the solution increased the viscosity by twice which is expected. However as the fluid is not well stirred before usage polymers might behave like particles flowing inside the fluid. However, more or less, Rodd 2007 has nearly doubled the viscosity by adding polymers for WG15.

  3. Observation: For WG85, as the water is quite limited the fluid appeared cloudy by naked eye. It may indicate that polymers have not mixed at all. Thus, for WG85PEO, the increment of viscosity is sufficiently low and probably not correct. Stabinger test also proves it.

  4. Observation: Low shear rate measurements are limited by motor torque but Anton Paar 312-M motor capabilities are not included.

Stabinger Test

- The Stabinger viscometer is quite feasible method to measure viscosity and density of the liquid. It is fast and easy to use. As a benchmark, DI water at 25°C is measured as (0.903 mPa.s) and the result is matched with known viscosity of DI water at given temperature.

- Yellow paintings are representing the fluid without PEO so they are Newtonian fluids in Table.5.1. We used these values in Table.5.2 for measuring intrinsic viscosity which is explained in detail in the following section.

- The intrinsic viscosities are placed in Table.5.2. The linear interpolation is used to calculate the limit for zero concentration. More points imply better interpolation for concentration independent intrinsic viscosity.

Solution Code	Probencode	T [°C]	$\eta\ (mPa \cdot s)$	η_s	η_p
WG15	M3110-000	23	1.423	1.423	0.000
WG15PEO075	M3110-001	23	2.520	1.423	1.097
WG15PEO15	M3110-002	23	4.117	1.423	2.694
WG15PEO30	M3110-003	23	8.427	1.423	7.004
WG30	M3111-000	23	2.247	2.247	0.000
WG30PEO075	M3111-001	23	3.965	2.247	1.718
WG30PEO15	M3111-002	23	6.062	2.247	3.815
WG30PEO30	M3111-003	23	12.685	2.247	10.438
WG45	M3112-000	23	4.080	4.080	0.000
WG45PEO075	M3112-001	23	6.872	4.080	2.792
WG45PEO15	M3112-002	23	10.408	4.080	6.328
WG45PEO30	M3112-003	23	18.404	4.080	14.324

Table 5.1: Viscosity of several solutions with Stabinger, results are without proper stirring. For proper mixture results check table.5.3.

5.2.3 Relaxation Time Characterization

Two main methods are available to find relaxation time. (i) using oscillatory test in rheometer for a range of different frequency and fit the data to a model (ii) calculating intrinsic viscosity to obtain Zimm relaxation time.

Rheometer test

- A oscillatory deformation test take place for different deformations ($\%\gamma$) , for a range of $[0.1\%\gamma - 10\%\gamma]$, G' (storage modules) and G" (loss modules) are measured. This procedure done to ensure to make oscillatory test in stable cases. It is observed that the modules values are quite stable above $0.5\%\gamma$ magnitude.

- Measurements take place for different shear rates (ω or γ), for a range of [0.001 Hz - 100 Hz] in one deformation value (1% γ), G' (storage modules) and G" (loss modules) are measured. This procedure should be done for both base lubricant (Water + Glycerol) and mixture (Water + Glycerol + PEO).

- For ($\omega \rightarrow 0$) the viscosity is shown as zero shear rate viscosity η_0 but for this experiments, the zero subscript is omitted because it represents mixture viscosity. Instead just, η is shown for zero shear rate and η' is shown for dynamic viscosity. The relationships are shown [130, 121] where λ is relaxation time:

$$\eta = \eta_s + \frac{\eta_p}{1 + (\lambda\omega)^2} \tag{5.1}$$

Its relationship with G" is given [121]:

$$\eta' = \frac{G''}{\omega} \tag{5.2}$$

And by Quinzani et. al. dynamic rigidity is:

$$\eta'' = \frac{G'}{\omega} = \frac{\eta\lambda\omega}{1 + (\lambda\omega)^2} \tag{5.3}$$

The first normal stress difference is depending on storage modules:

$$N_1 = 2\frac{G'}{\omega} \tag{5.4}$$

For Olroyd-B model the loss modules is related to relaxation time via when $(\omega \to 0)$:

$$N_1 = 2\eta_p\lambda \tag{5.5}$$

- The test is applied on DI water, WG15, WG15PEO, WG85, WG85PEO. However, it is noted that for low relaxation time it is nearly impossible to measure G' with oscillatory test [122, 124]

- Fig.5.3 shows the storage modules (G') for Newtonian water, low viscosity PEO solution and high viscosity PEO solution. The fit for Oldroyd-B relaxation time is also plotted.

- 1. Observation: The collected data quite unstable for frequency range [0.1 - 0.6] Hz as it can be seen from Fig.5.3. For lower frequency values unstable data points continues. This can be related to the very low torque values. It is already knownn that at low viscosities measuring relaxation time is cumbersome .

  2. Observation: Increasing viscosity changes the readable G' values but adding PEO seems does not affect the storage modules. Check the water storage modules in Fig.5.3 to observe that water has shown very similar storage modules to solution containing PEO. This leads to the conclusion that PEO does not exhibit any memory effect.

3. Observation: The solutions are not well mixed before the experiments. It might be the case that PEO just create a particle cluster in the fluid without memory effect.

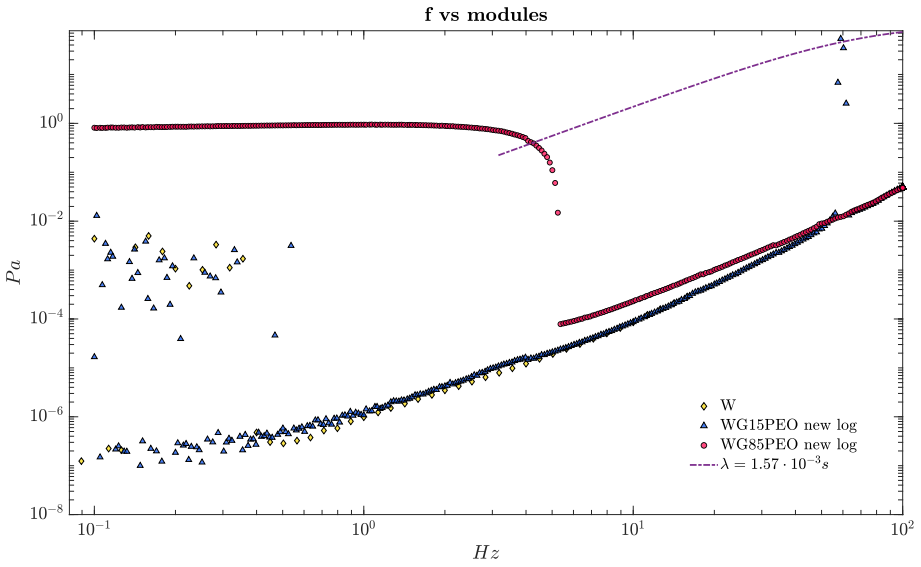

Figure 5.3: G' for a frequency sweep in oscillatory test. Different measuring methods such as linear sweep, log sweep, time between each data point, total data point in a sweep end up in similar results.

Intrinsic Viscosity test

- Intrinsic viscosity is a common quantity used in chemistry to measure the effect of additional substance to fluid on the viscosity of solvent. Increasing concentration of the additive increases the viscosity. Intrinsic viscosity is the measure of this increment factor. It is shown as $[\eta]$ and the unit is (mL/g).
- To calculate intrinsic viscosity, first viscosities of solvent and polymer should be measured. Let's call viscosity of solvent η_s and viscosity of polymers η_p. The

Solution Code	β	$\tilde{\beta}$	ρ [g/cm^3]	η_p/η_s	c [wt. %]	c [g/ml]	$[\eta]$ [ml/g]	$\lim_{c\to 0}[\eta]$
WG15	1.00	0.00	1.0329	0	0	0	-	811
WG15PEO075	0.56	0.44	1.0334	0.770625	0.075	0.000775	994.2913	-
WG15PEO15	0.35	0.65	1.0334	1.893113	0.15	0.00155	1221.285	-
WG15PEO30	0.17	0.83	1.0339	4.922089	0.3	0.003102	1586.901	-
WG30	1.00	0.00	1.0702	0	0	0	-	752
WG30PEO075	0.57	0.43	1.0707	0.764397	0.075	0.000803	951.8969	-
WG30PEO15	0.37	0.63	1.0706	1.697626	0.15	0.001606	1057.118	-
WG30PEO30	0.18	0.82	1.0709	4.645453	0.3	0.003213	1445.965	-
WG45	1.00	0.00	1.1091	0	0	0	-	762
WG45PEO075	0.59	0.41	1.1099	0.68433	0.075	0.000832	822.0922	-
WG45PEO15	0.39	0.61	1.11	1.551062	0.15	0.001665	931.5688	-
WG45PEO30	0.22	0.78	1.11	3.510866	0.3	0.00333	1054.314	-

Table 5.2: Intrinsic Viscosity Calculations

ratio of them is called $\beta = \frac{\eta_s}{\eta_o}$ (it is also called relative viscosity in chemist for ($\eta_{rel} = \frac{1}{\beta}$) earlier. Lets define $\tilde{\beta} = \frac{\eta_p}{\eta_o}$ for polymeric case. The specific viscosity is defined as then: $\eta_{spe} = \frac{\tilde{\beta}}{\beta} = \frac{\eta_p}{\eta_s}$. If this specific viscosity is divided by concentration intrinsic viscosity is obtained in the limit of concentration goes zero. It is logical that, increasing concentration increases viscosity contribution of additive. This increase is somewhat related to the solvent property.

$$[\eta] = \lim_{c\to 0} \frac{\eta_{spe}}{c} \tag{5.6}$$

The concentration unit is [g/mL]. So, the additive weight should divide by the volume of the full solution. Thus, x % wt. concentration turns out to be $(x \cdot \rho/100)$ where ρ in units of [g/ml]. The limit for zero concentration might be calculated by linear fit to several difference concentrations of additives in solvents.

- Stabinger viscometer is feasible to calculate intrinsic viscosity as it can provide density and viscosity quite accurately and fast. Then, the intrinsic viscosity is used in Zimm's theory for relaxation time:

$$\lambda_{Zimm} = F\frac{[\eta]M_W\eta_s}{N_A k_B T} \tag{5.7}$$

where M_W is the molecular weight, N_A is Avogadro's constant, k_B is the Boltzmann's constant, T is the absolute temperature, η_s is the solvent viscosity, and $[\eta]$ is intrinsic viscosity. The prefactor F is estimated by the Riemann Zeta function $(3\nu)^{-1} = \sum_{i=1}^{\inf} = 1/i^{3\nu}$, ν being the solvent quality exponent given as 0.55 by Rodd et. al. [123].

- The initial results for intrinsic viscosity without stirring the solutions are plotted against Rodd et. al. 2005.

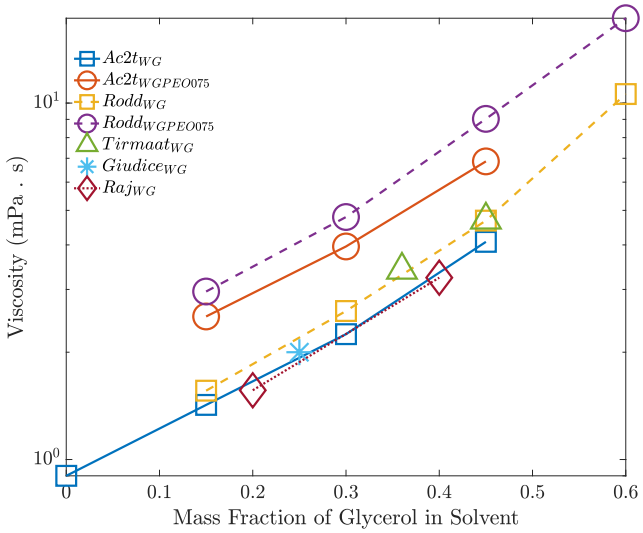

Figure 5.4: Viscosity values compared to literature literature (Rodd et. al. 2007), (Tirmaatmadja et. al. 2006), (Giudice et. al. 2016) and (Raj&Sen 2016) at 23°C

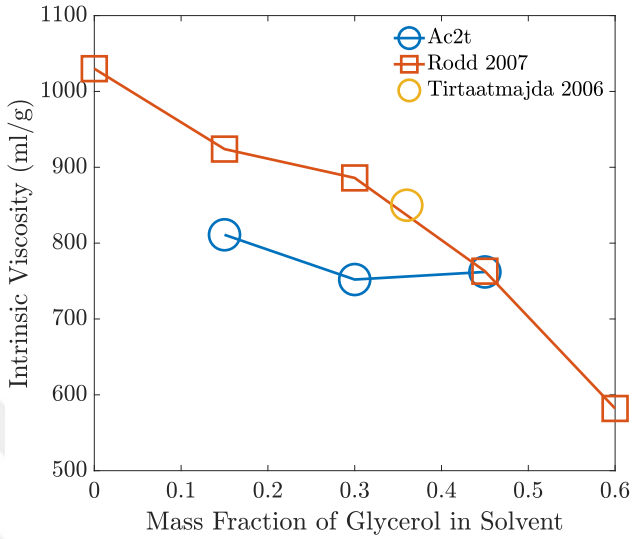

Figure 5.5: Viscosity values compared to literature literature (Rodd et. al. 2007), (Tirmaatmadja et. al. 2006), (Giudice et. al. 2016) and (Raj&Sen 2016) at 23°C

- We cannot be sure why Rodd water/glycerol solutions are different than our intrinsic viscosities in Fig.5.5. However, it is available us that the proper mixture of the PEO with water will slightly increase the viscosities which converges to Rodd's results. These findings are supported in Table.5.3 where the proper mixture showed an increment of viscosity compared to previous mixtures. Moreover, observe Fig.5.5 for different papers WG mixture viscosity values. There is no well known benchmark in the literature for WG mixture viscosities. These differences can be caused due to (i) different glycerol manufactures, (ii) poor mixture before measurements. The PEO solutions unfortunately can be just compared with Rodd as researchers might prefer different molecular weight of PEO. For instance, Casanellas et. al. uses $4 \cdot 10^6 M_W$ PEO for WG mixture [131].

Solution Code	T [°C]	η $[mPa \cdot s]$
WG15PEO30 (Bad mixture)	23	8.427
WG30PEO30 (Bad mixture)	23	12.685
WG15PEO30 (Proper mixture)	23	9.020
WG30PEO30 (Proper mixture)	23	13.974

Table 5.3: Viscosities of proper mixture compared to the previous viscosity results. Proper mixture is prepared by obeying the rules given at Sec.5.2.1 Sample Preparation. Bad mixtures are older compared to proper mixtures and not well mixed during preparation

5.2.4 Normal Load Measurements

Normal load measurements are very common for characterizing viscoelasticity. In order to magnify the effect of normal stress difference caused by polymers, simple shear cone-plate, plate-plate configuration is used [52]. However, in our study, as we cannot observe the relaxation time in oscillatory test, we could just test cone-plate configuration similar to literature [131]. The measurements were limited to several days but measurement are shown for sharing experience for experiments.

The force due to polymer elasticity is expressed as:

$$F_{polymer} = -(\pi R^2)/2N_1 \tag{5.8}$$

The normal stress difference $N_1, (\tau_{\phi\phi} - \tau_{\theta\theta})$, difference of stress in direction of rotating and the azimuthal direction, crates a pressure gradient towards to center, dp/dr, and this pressure is able to generate normal load. The inertial effect on normal force is:

$$F_{inertia} = -0.075\pi\rho\Omega^2 R^4 \tag{5.9}$$

Inertial force caused by high rotation speed might be included for normal force calculations to seperate elastic forces and inertial forces.

4° angle cone and flat plate measurments

1. Observation: Surface tension provides a baseline load for load sensors in the rheometer. Therefore, surface tension should be accounted for in all total force measurements. During rotation, the load increases, but the reason for this increment is unclear. This indicates that the fluid might overflow the cone, creating different surface forces dependent on the motor's speed. This aspect is worth considering.

2. Observation: For 2.5 mL of WG30PEO30 and 300um gap initial surface tension is measured 0.11N on the led display of rheometer. Adding (just touching) soap-water solution to the surface of the WG30PEO30, reduced to the load 0.07N in led display.

3. Observation: Another observation is that compressing the fluid increases the surface tension load. To neutralize the surface tension, slowly move the test cone upwards after setting the initial gap. When the load reads 0.00 N, it indicates that the surface tension has been neutralized. Ensure that there is contact between the cone and the fluid. Once contact is confirmed, if the gap shows a load very close to 0.00 N, you can start the measurement. Reducing the gap further can cause the fluid to rise above the cone and create surface tension again.

4. The measurements were conducted following the shear rate protocols outlined in the paper by Casanellas et al. [131]. They investigated the normal stress difference in WG25 with varying concentrations of PEO using a cone and plate configuration. For Newtonian fluids, shear rates of 400 (1/s) were applied for 400 seconds and 500 (1/s) for another 400 seconds. Non-Newtonian fluids were

subjected to shear rates of 400 (1/s) for 400 seconds, 500 (1/s) for 400 seconds, and 600 (1/s) for 200 seconds. These experimental conditions were tabulated and can serve as reference for future cone-plate experiments, providing concise information for further research.

#	γ (1/s)	Δh (mm)	V (mL)	I. Force (mN)	M. Force (mN)	L. Force (mN)	t (s)
Initial	0	1.050	3	-10			0
1	400	1.050	3	-250	-260	-270	400
2	500	1.050	3	-340	-330	-320	400
After	0	1.050	3	30			-

Table 5.4: Force Measurements at Various Shear Rates for WG15, 23°C, Notes: soup added after gap adjusted

#	γ (1/s)	Δh (mm)	V (mL)	I. Force (mN)	M. Force (mN)	L. Force (mN)	t (s)
Initial	0	1.100	3	-10			0
1	400	1.100	3	-250	-260	-270	400
2	500	1.100	3	-340	-330	-320	400
3	600	1.100	3	-520	-	-530	200
After	0	1.100	3	-10			-

Table 5.5: Force Measurements at Various Shear Rates for WG15PEO30,23°C, Notes: 2 days old PEO mixture, soup added before height adjustment

1. Result: Table.5.4 and Table.5.5 contains the resulted force for given shear rates. The initial force due to surface tension and last force after the rotation is noted. For 400 seconds of rotation, the initial force of and last force measurement is noted. The differences between the forces are negligible. It can be deduced that for the given shear rates the solution reach to steady state in minutes.

2. Result: Table.5.4 and Table.5.5 are measurements of Newtonian and non-Newtonian liquids. According to the theory normal force should be zero in Newtonian fluids. Thus, the measured force at table.5.4 might be the result of the inertia, surface tension etc. In table.5.5, the measured forces are close

to the table.5.4 but slight difference is observed. The difference can be due to normal force created by (i) elasticity of the fluid (ii) the measurement error (iii) insufficient number of experiments.

5.3 Summary of Experiments and Comments

The experimental aspect of this thesis, aimed primarily at numerical modeling, was intentionally limited and basic. This section serves as a foundational starting point for future studies, synthesizing insights from various references. Nevertheless, even with these preliminary experiments, there is potential to uncover more about the behavior of viscoelastic fluids

The methods employed for conducting load-carrying experiments with viscoelastic fluids encompass several key steps. These include defining the study scope, preparing fluid samples, and characterizing them using Anton-Paar rheometer and Stabinger viscometer instruments. Experimental techniques involve measuring relaxation time, loss modulus, normal stress difference, and Zimm's relaxation time. Lastly, methodologies are detailed for measuring normal load in the Anton-Paar 302 Rheometer, along with strategies to highlight the effects of viscoelasticity.

After numerous trials, we were unable to conclusively determine the relaxation time of fluids under shear flows. There is no clear evidence of shear viscoelasticity in the PEO-water solutions we tested. While extensional viscoelasticity was observed visually, shear viscoelasticity was not detected in either the Rheometer oscillatory tests or cone-plate shear flow experiments. The results of PEO mixtures consistently mirrored those of Newtonian fluids in many trials. Possible reasons for this failure include: (i) poor initial quality of the solution mixtures, (ii) insufficient concentration of PEO to observe relaxation effects, and (iii) lack of well-designed and sufficient

experiments with high-quality PEO mixtures. However, it is worth noting that literature reports observing viscoelasticity with PEO solutions similar to ours, although the detailed methodologies are not well-explained. In the three months of our study, we focused on reviewing the literature, refining the sample preparation process, and familiarizing ourselves with the instruments for our experiments. The cone-plate configuration requires further attention to accurately detect shear relaxation times in future studies, as it has not been extensively studied

Overall, this experimental work includes the basic steps for measuring low viscosity non-Newtonian fluids and initial data obtained from instruments. The experience during the work narrated to this report.

Chapter 6

Conclusion

Numerical viscoelastic models have been applied to solve the behavior of polymeric additive fluids in soft lubrication scenarios. These fluid numerical methods have been successfully integrated with the solid boundary element method. The results have expanded to investigate contraction geometries, shedding light on the reasons for load increment in soft EHL cases. Additionally, new numerical methods have been developed to solve the Oldroyd-B equations and validated against previous studies. Experimental studies on viscoelastic fluids have been conducted as an initial step for future investigations.

Soft lubrication receives more attention compared to hydrodynamic lubrication cases, particularly in terms of friction performance. When the fluid regime is fully controlled by viscous forces and solid elastic forces are low, the friction coefficient remains constant. However, higher elasticity of solids increases the effectiveness of viscoelasticity. These findings are linked to the load-carrying capacity of lubricants in various elastic contact geometries. Higher elasticity leads to greater deformation of the contact surface. This concept is applied to study simple contraction geometries,

aiming to simplify complex flow dynamics and analytical approaches.

The study of contraction and expansion geometries aims to isolate stress terms from complex flow fluxes and examine the relaxation of individual stress components. It is well-known that normal stress gradients are the primary source of pressure increment. The effects of elastic normal stress gradients and shear stress on the mass flow rate provide an explanation for load-carrying capacity. Investigating the relaxation behavior of polymers in diverging and converging channels of sufficient length can highlight their impact on load-carrying capacity. Thus, optimizing fluid relaxation or the design of flow channels can enhance the efficiency of polymeric fluids.

Experiments were conducted to compare the load-carrying capacity with the developed model. Due to time limitations and lack of experience, the measurements of normal force could not be completed, and thus comparison with the model could not be performed. However, this section provides essential insights to initiate further projects aimed at measuring viscoelastic effects. The experiments contributed to simulations by influencing ideas and parameter choices. Experimental findings necessitated several modifications to the models, such as incorporating periodic boundary conditions, which were not initially included in our model study. The selected parameters in the modeling phase were chosen to accurately reflect real-world conditions, despite the absence of field knowledge.

The parameter choice of De number and viscosity ratio, β in the models are reasonable and can be reproducible in laboratory environments. However, the reliability of these parameters in industrial fluids and bearings remains uncertain. Polymer additives used in industry are primarily focused on viscosity improvement or heat capacity, with limited study on viscoelasticity. Consequently, the relaxation times of polymers are largely unknown even within the industrial tribology field. This lack of understanding makes it challenging to estimate length scales and speed

ranges applicable to such applications.

An intriguing example highlighting the unavailability of viscoelastic effects is found in lip seals used in rotary shafts. Reports suggest an unexplained force that causes oil seals to leak. This force is speculated to be due to the normal force directed at the seal, given the absence of curvature in rotary shafts. However, studies on contractions demonstrate that even slight height differences of one to two percent can lead to load increments depending on the location. The initial assumptions for De and β in our models are relevant to this case. Industrial applications may not be limited to a single scenario but encompass various areas of study.

The thesis introduces an efficiently working reduced model with adjustable parameters supported by strong references in the field. The study on soft lubrication has been published in a journal article, underscoring the relevance of the subject. The investigation into high-gradient contraction/expansion channels provides a robust foundation for understanding polymeric relaxation, with plans to submit findings to respected journal articles in the coming months. Finally, the thesis demonstrates that experimental studies in lubrication are complemented by a developed and specialized numerical model, thereby generating increased interest in both academia and industry.

Bibliography

[1] Jost HP, Schofield J. Energy Saving through Tribology: A Techno-Economic Study. Proceedings of the Institution of Mechanical Engineers. 1981;195(1):151-73. Available from: https://doi.org/10.1243/PIME_PROC_1981_195_016_02.

[2] Holmberg K, Erdemir A. Influence of tribology on global energy consumption, costs and emissions. Friction. 2017 Sep;5(3):263-84. Available from: http://link.springer.com/10.1007/s40544-017-0183-5.

[3] Scaraggi M, Mezzapesa FP, Carbone G, Ancona A, Tricarico L. Friction Properties of Lubricated Laser-MicroTextured-Surfaces: An Experimental Study from Boundary- to Hydrodynamic-Lubrication. Tribology Letters. 2013 Jan;49(1):117-25. Available from: http://link.springer.com/10.1007/s11249-012-0045-2.

[4] Palacio M, Bhushan B. A Review of Ionic Liquids for Green Molecular Lubrication in Nanotechnology. Tribology Letters. 2010 Nov;40(2):247-68. Available from: http://link.springer.com/10.1007/s11249-010-9671-8.

[5] Maqbool K, Siddiqui AM, Mehboob H, Jamil Q. Study of non-Newtonian synovial fluid flow by a recursive approach. Physics of Fluids. 2022 Nov;34(11):111903. Available from:

https://pubs.aip.org/pof/article/34/11/111903/2846707/Study-of-non-Newtonian-synovial-fluid-flow-by-a.

[6] Vlădescu SC, Putignano C, Marx N, Keppens T, Reddyhoff T, Dini D. The Percolation of Liquid Through a Compliant Seal—An Experimental and Theoretical Study. Journal of Fluids Engineering. 2019 Mar;141(3):031101. Available from: https://asmedigitalcollection.asme.org/fluidsengineering/article/doi/10.1115/1.4041120/457711/The-Percolation-of-Liquid-Through-a-Compliant.

[7] Dapp WB, Lücke A, Persson BNJ, Müser MH. Self-Affine Elastic Contacts: Percolation and Leakage. Physical Review Letters. 2012 Jun;108(24):244301. Available from: https://link.aps.org/doi/10.1103/PhysRevLett.108.244301.

[8] El-Butch AM, Ashour NM. Analysis of heavy duty tilting-pad journal bearing taking into account pad distortion and possible adoption of rubber pad segments. Tribology International. 1999 Jun;32(6):285-93. Available from: https://linkinghub.elsevier.com/retrieve/pii/S0301679X99000468.

[9] Meng Y, Xu J, Jin Z, Prakash B, Hu Y. A review of recent advances in tribology. Friction. 2020 Apr;8(2):221-300. Available from: http://link.springer.com/10.1007/s40544-020-0367-2.

[10] Tao FF, Philippoff W. Hydrodynamic Behavior of Viscoelastic Liquids in a Simulated Journal Bearing. A S L E Transactions. 1967 Jan;10(3):302-15. Available from: http://www.tandfonline.com/doi/abs/10.1080/05698196708972188.

[11] Anand M, Kwack J, Masud A. A new generalized Oldroyd-B model for blood flow in complex geometries. International Journal of Engineering Science. 2013 Nov;72:78-88. Available from: https://linkinghub.elsevier.com/retrieve/pii/S0020722513001006.

[12] Reynolds O. On the Theory of Lubrication and Its Application to Mr. Beauchamp Tower's Experiments, Including an Experimental Determination of the Viscosity of Olive Oil. Philosophical Transactions of the Royal Society of London. 1886;177:157-234. Available from: https://www.jstor.org/stable/109480.

[13] B HW, I D. Boundary lubrication.— The paraffin series. Proceedings of the Royal Society. 1922;100:550-74.

[14] Gong L, Kinloch IA, Young RJ, Riaz I, Jalil R, Novoselov KS. Interfacial Stress Transfer in a Graphene Monolayer Nanocomposite. Advanced Materials. 2010 Jun;22(24):2694-7. Available from: https://onlinelibrary.wiley.com/doi/10.1002/adma.200904264.

[15] Hamrock BJ, Schmid SR, Jacobson BO. Fundamentals of Fluid Film Lubrication. CRC Press; 2004.

[16] Beeck O. On the mechanism of boundary lubrication. II. Wear prevention by addition agents. Proceedings of the Royal Society of London Series A Mathematical and Physical Sciences. 1940 Dec;177(968):103-18. Available from: https://royalsocietypublishing.org/doi/10.1098/rspa.1940.0113.

[17] Hamilton DB, Walowit JA, Allen CM. A Theory of Lubrication by Microirregularities. Journal of Basic Engineering. 1966 03;88(1):177-85. Available from: https://doi.org/10.1115/1.3645799.

[18] Gropper D, Wang L, Harvey TJ. Hydrodynamic lubrication of textured surfaces: A review of modeling techniques and key findings. Tribology International. 2016 Feb;94:509-29. Available from: https://linkinghub.elsevier.com/retrieve/pii/S0301679X15004582.

[19] Borras Subirana FX. Rotary Lip Seal Operation with Environmentally Acceptable Lubricants [PhD]. Enschede, The Netherlands; 2020. ISBN: 9789036550444. Available from: http://purl.org/utwente/doi/10.3990/1.9789036550444.

[20] Baart P. Grease lubrication in radial lip seals [PhD]. Luleå; 2009. ISBN: 978-91-86233-50-1.

[21] Etsion I, Burstein L. A Model for Mechanical Seals with Regular Microsurface Structure. Tribology Transactions. 1996 Jan;39(3):677-83. Available from: http://www.tandfonline.com/doi/abs/10.1080/10402009608983582.

[22] Rus D, Tolley MT. Design, fabrication and control of soft robots. Nature. 2015 May;521(7553):467-75. Available from: https://www.nature.com/articles/nature14543.

[23] Ahn BK, Lee DW, Israelachvili JN, Waite JH. Surface-initiated self-healing of polymers in aqueous media. Nature Materials. 2014 Sep;13(9):867-72. Available from: https://www.nature.com/articles/nmat4037.

[24] Bao G, Suresh S. Cell and molecular mechanics of biological materials. Nature Materials. 2003 Nov;2(11):715-25. Available from: https://www.nature.com/articles/nmat1001.

[25] Oates KMN, Krause WE, Colby RH. Using rheology to probe the mechanism of joint lubrication: Polyelectrolyte/protein interactions in synovial fluid. Materials Research Society Symposium. 2002 Jan;711:53-8.

[26] Rodríguez-Hakim M, Räz L, Vermant J. Variations in human saliva viscoelasticity affect aerosolization propensity. Soft Matter. 2022;18(13):2528-40. Available from: http://xlink.rsc.org/?DOI=D1SM01581H.

[27] Karimi A, Razaghi R, Padilla S, Rahmati SM, Downs JC, Acott TS, et al. Viscoelastic Biomechanical Properties of the Conventional Aqueous Outflow

Pathway Tissues in Healthy and Glaucoma Human Eyes. J Clin Med. 2022 Oct;11(20):6049.

[28] Bilgi C, Atalık K. Effects of blood viscoelasticity on pulsatile hemodynamics in arterial aneurysms. Journal of Non-Newtonian Fluid Mechanics. 2020 May;279:104263. Available from: https://linkinghub.elsevier.com/retrieve/pii/S0377025720300318.

[29] Tichy J, Bou-Saïd B. The Phan-Thien and Tanner Model Applied to Thin Film Spherical Coordinates: Applications for Lubrication of Hip Joint Replacement. Journal of Biomechanical Engineering. 2008 Apr;130(2):021012. Available from: https://asmedigitalcollection.asme.org/biomechanical/article/doi/10.1115/1.2899573/452367/The-PhanThien-and-Tanner-Model-Applied-to-Thin.

[30] Szeri AZ. Fluid film lubrication. 2nd ed. Cambridge ; New York: Cambridge University Press; 2011. OCLC: ocn656772007.

[31] Herzt VHH. Ueber die Berührung fester elastischer Körper. Journal fur die reine und angewandte Mathematik. 1881;92:156-71.

[32] Johnson KL. Contact Mechanics. Cambridge University Press; 1985.

[33] Spikes HA. Sixty years of EHL. Lubrication Science. 2006 Oct;18(4):265-91. Available from: https://onlinelibrary.wiley.com/doi/10.1002/ls.23.

[34] Bair S. The First Normal Stress Difference in a Shear-Thinning Motor Oil at Elevated Pressure. Tribology Transactions. 2015 Jul;58(4):654-9. Available from: http://www.tandfonline.com/doi/full/10.1080/10402004.2015.1012773.

[35] Mitsui H, Spikes HA. Predicting EHD Film Thickness of Lubricant Polymer Solutions. Tribology Transactions. 1998 Jan;41(1):1-10. Available from: http://www.tandfonline.com/doi/abs/10.1080/10402009808983715.

[36] Bair S, Qureshi F. The high pressure rheology of polymer-oil solutions. Tribology International. 2003 Aug;36(8):637-45. Available from: https://linkinghub.elsevier.com/retrieve/pii/S0301679X03000082.

[37] D'Agostino V, Petrone V, Senatore A. The Influence of Piezo-Viscous Lubricants on EHL Line and Point Contact Problems. In: Volume 3: Design, Materials and Manufacturing, Parts A, B, and C. Houston, Texas, USA: American Society of Mechanical Engineers; 2012. p. 1021-31. Available from: https://asmedigitalcollection.asme.org/IMECE/proceedings/IMECE2012/45196/1021/288745.

[38] Elsharkawy AA, Hamrock BJ. EHL of Coated Surfaces: Part I—Newtonian Results. Journal of Tribology. 1994 Jan;116(1):29-36. Available from: https://asmedigitalcollection.asme.org/tribology/article/116/1/29/437158/EHL-of-Coated-Surfaces-Part-INewtonian-Results.

[39] Bair S, Lockwood FE, Anderson WB, Zhang Z, Dotson D. Measurements of Elasticity in Multigrade Motor Oil at Elevated Pressure. Tribology Transactions. 2007 Jun;50(3):407-14. Available from: http://www.tandfonline.com/doi/abs/10.1080/10402000701429279.

[40] Williamson BP, Walters K, Bates TW, Coy RC, Milton AL. The viscoelastic properties of multigrade oils and their effect on journal-bearing characteristics. Journal of Non-Newtonian Fluid Mechanics. 1997 Nov;73(1-2):115-26. Available from: https://linkinghub.elsevier.com/retrieve/pii/S0377025797000396.

[41] Veltkamp B, Jagielka J, Velikov KP, Bonn D. Lubrication with Non-Newtonian Fluids. Physical Review Applied. 2023 Jan;19(1):014056. Available from: https://link.aps.org/doi/10.1103/PhysRevApplied.19.014056.

[42] Phan-Thien N, Low HT. Squeeze-film flow of a viscoelastic fluid a lubrication

model. Journal of Non-Newtonian Fluid Mechanics. 1988 Jan;28(2):129-48. Available from: https://linkinghub.elsevier.com/retrieve/pii/0377025788850365.

[43] Wang SH, Zhang HH. Combined Effects of Thermal and Non-Newtonian Character of Lubricant on Pressure, Film Profile, Temperature Rise, and Shear Stress in E.H.L. Journal of Tribology. 1987 Oct;109(4):666-70. Available from: https://asmedigitalcollection.asme.org/tribology/article/109/4/666/433626/Combined-Effects-of-Thermal-and-NonNewtonian.

[44] Wang J, Zhang HH. A Higher Order Perturbational Approach in the Lubricated EHL Contacts With Non-Newtonian Lubricant. Journal of Tribology. 1992 Jan;114(1):95-9. Available from: https://asmedigitalcollection.asme.org/tribology/article/114/1/95/435061/A-Higher-Order-Perturbational-Approach-in-the.

[45] Wolff R, Kubo A. A Generalized Non-Newtonian Fluid Model Incorporated Into Elastohydrodynamic Lubrication. Journal of Tribology. 1996 Jan;118(1):74-82. Available from: https://asmedigitalcollection.asme.org/tribology/article/118/1/74/439606/A-Generalized-Non-Newtonian-Fluid-Model.

[46] Khonsari MM, Hua DY. Generalized non-Newtonian elastohydrodynamic lubrication. Tribology International. 1993 Dec;26(6):405-11. Available from: https://linkinghub.elsevier.com/retrieve/pii/0301679X9390080K.

[47] Putignano C, Dini D. Soft Matter Lubrication: Does Solid Viscoelasticity Matter? ACS Applied Materials & Interfaces. 2017 Dec;9(48):42287-95. Available from: https://pubs.acs.org/doi/10.1021/acsami.7b09381.

[48] Putignano C, Rouzic JL, Reddyhoff T, Carbone G, Dini D. A theoretical and experimental study of viscoelastic rolling contacts incorporating thermal

effects. Proceedings of the Institution of Mechanical Engineers, Part J: Journal of Engineering Tribology. 2014;228(10):1112-21. Available from: https://doi.org/10.1177/1350650114530681.

[49] Zhao Y, Liu HC, Morales-Espejel GE, Venner CH. Effects of solid viscoelasticity on elastohydrodynamic lubrication of point contacts. Tribology International. 2022 Jul;171:107562. Available from: https://linkinghub.elsevier.com/retrieve/pii/S0301679X22001359.

[50] Carbone G, Putignano C. Rough viscoelastic sliding contact: Theory and experiments. Phys Rev E. 2014 Mar;89:032408. Available from: https://link.aps.org/doi/10.1103/PhysRevE.89.032408.

[51] James DF. Boger Fluids [Journal Article]. Annual Review of Fluid Mechanics. 2009;41(Volume 41, 2009):129-42. Available from: https://www.annualreviews.org/content/journals/10.1146/annurev.fluid.010908.165125.

[52] Morozov A, Spagnolie SE. Introduction to Complex Fluids. In: Spagnolie SE, editor. Complex Fluids in Biological Systems: Experiment, Theory, and Computation. New York, NY: Springer New York; 2015. p. 3-52. Available from: https://doi.org/10.1007/978-1-4939-2065-5_1.

[53] Larson RG. CHAPTER 8 - Viscoelasticity of Dilute Polymer Solutions. In: Larson RG, editor. Constitutive Equations for Polymer Melts and Solutions. Butterworths Series in Chemical Engineering. Butterworth-Heinemann; 1988. p. 219-70. Available from: https://www.sciencedirect.com/science/article/pii/B9780409901191500130.

[54] Yildirim AB, Erbaş A, Biancofiore L. Molecular rheology of nanoconfined oligomer melts. Journal of Rheology. 2024 03;68(3):285-99. Available from: https://doi.org/10.1122/8.0000751.

[55] Van Der Zanden J, Hulsen M. Mathematical and physical requirements for successful computations with viscoelastic fluid models. Journal of Non-Newtonian Fluid Mechanics. 1988 Jan;29:93-117. Available from: https://linkinghub.elsevier.com/retrieve/pii/0377025788850523.

[56] Oldroyd JG. On the formulation of rheological equations of state. Proc R Soc Lond. 1950 Feb;200:523-41. Available from: https://royalsocietypublishing.org/doi/10.1098/rspa.1950.0035.

[57] Tichy JA. Non-Newtonian Lubrication With the Convected Maxwell Model. Journal of Tribology. 1996 Apr;118(2):344-8. Available from: https://doi.org/10.1115/1.2831307.

[58] Olsson F, Yström J. Some properties of the Upper Convected Maxwell model for viscoelastic fluid flow. Journal of Non-Newtonian Fluid Mechanics. 1993 Jul;48(1-2):125-45. Available from: https://linkinghub.elsevier.com/retrieve/pii/037702579380068M.

[59] Thien NP, Tanner RI. A new constitutive equation derived from network theory. Journal of Non-Newtonian Fluid Mechanics. 1977 Jul;2(4):353-65. Available from: https://linkinghub.elsevier.com/retrieve/pii/0377025777800219.

[60] Tanner RI, Nasseri S. Simple constitutive models for linear and branched polymers. Journal of Non-Newtonian Fluid Mechanics. 2003 Dec;116(1):1-17. Available from: https://linkinghub.elsevier.com/retrieve/pii/S0377025703001940.

[61] Warner HR. Kinetic Theory and Rheology of Dilute Suspensions of Finitely Extendible Dumbbells. Industrial & Engineering Chemistry Fundamentals. 1972 Aug;11(3):379-87. Available from: https://pubs.acs.org/doi/abs/10.1021/i160043a017.

[62] Bird RB, Dotson PJ, Johnson NL. Polymer solution rheology based on a finitely extensible bead—spring chain model. Journal of Non-Newtonian Fluid Mechanics. 1980;7(2):213-35. Available from: https://www.sciencedirect.com/science/article/pii/0377025780850075.

[63] Sawyer WG, Tichy JA. Non-Newtonian Lubrication With the Second-Order Fluid. Journal of Tribology. 1998 07;120(3):622-8. Available from: https://doi.org/10.1115/1.2834596.

[64] White SA, Gotsis AD, Baird DG. Review of the entry flow problem: Experimental and numerical. Journal of Non-Newtonian Fluid Mechanics. 1987 Jan;24(2):121-60. Available from: https://linkinghub.elsevier.com/retrieve/pii/0377025787850073.

[65] Owens RG, Phillips TN. Computational Rheology. Imperial College Press; 2002.

[66] Alves MA, Oliveira PJ, Pinho FT. Numerical Methods for Viscoelastic Fluid Flows. Annual Review of Fluid Mechanics. 2021 Jan;53(1):509-41. Available from: https://www.annualreviews.org/doi/10.1146/annurev-fluid-010719-060107.

[67] Phillips TN, Williams AJ. Comparison of creeping and inertial flow of an Oldroyd B fluid through planar and axisymmetric contractions. Journal of Non-Newtonian Fluid Mechanics. 2002 Dec;108(1-3):25-47. Available from: https://linkinghub.elsevier.com/retrieve/pii/S0377025702001234.

[68] Chakraborty D, Ravi Prakash J. Viscoelastic fluid flow in a 2D channel bounded above by a deformable finite-thickness elastic wall. Journal of Non-Newtonian Fluid Mechanics. 2015 Apr;218:83-98. Available from: https://linkinghub.elsevier.com/retrieve/pii/S0377025715000282.

[69] Fattal R, Kupferman R. Constitutive laws for the matrix-logarithm of the conformation tensor. Journal of Non-Newtonian Fluid Mechanics. 2004 Nov;123(2-3):281-5. Available from: https://linkinghub.elsevier.com/retrieve/pii/S0377025704002630.

[70] Fattal R, Kupferman R. Time-dependent simulation of viscoelastic flows at high Weissenberg number using the log-conformation representation. Journal of Non-Newtonian Fluid Mechanics. 2005 Feb;126(1):23-37. Available from: https://linkinghub.elsevier.com/retrieve/pii/S0377025705000042.

[71] Habla F, Tan MW, Haßlberger J, Hinrichsen O. Numerical simulation of the viscoelastic flow in a three-dimensional lid-driven cavity using the log-conformation reformulation in OpenFOAM®. Journal of Non-Newtonian Fluid Mechanics. 2014 Oct;212:47-62. Available from: https://linkinghub.elsevier.com/retrieve/pii/S0377025714001189.

[72] Pimenta F, Alves MA. Stabilization of an open-source finite-volume solver for viscoelastic fluid flows. Journal of Non-Newtonian Fluid Mechanics. 2017 Jan;239:85-104. Available from: https://linkinghub.elsevier.com/retrieve/pii/S0377025716303329.

[73] Zhang R, Li XK. Non-Newtonian effects on lubricant thin film flows. Journal of Engineering Mathematics. 2005 Jan;51(1):1-13. Available from: https://doi.org/10.1007/s10665-004-1342-z.

[74] Li XK, Luo Y, Qi Y, Zhang R. On non-Newtonian lubrication with the upper convected Maxwell model. Applied Mathematical Modelling. 2011 May;35(5):2309-23. Available from: https://linkinghub.elsevier.com/retrieve/pii/S0307904X10004130.

[75] Boyko E, Christov IC. Non-Newtonian fluid–structure interaction: Flow of

a viscoelastic Oldroyd-B fluid in a deformable channel. Journal of Non-Newtonian Fluid Mechanics. 2023 Mar;313:104990. Available from: https://linkinghub.elsevier.com/retrieve/pii/S0377025723000022.

[76] Housiadas KD, Beris AN. Lubrication approximation of pressure-driven viscoelastic flow in a hyperbolic channel. Physics of Fluids. 2023 Dec;35(12):123116. Available from: https://pubs.aip.org/pof/article/35/12/123116/2930432/Lubrication-approximation-of-pressure-driven.

[77] Ahmed H, Biancofiore L. Modeling polymeric lubricants with non-linear stress constitutive relations. Journal of Non-Newtonian Fluid Mechanics. 2023 Nov;321:105123. Available from: https://linkinghub.elsevier.com/retrieve/pii/S0377025723001350.

[78] Ahmed H, Biancofiore L. A new approach for modeling viscoelastic thin film lubrication. Journal of Non-Newtonian Fluid Mechanics. 2021 Jun;292:104524. Available from: https://linkinghub.elsevier.com/retrieve/pii/S037702572100046X.

[79] B J, L F. The finite journal bearing, considering vaporization. Trans Chalmers Univ Technol. 1957;190.

[80] KO O. Cavitation in dynamically loaded bearings. Trans Chalmers Univ Technol. 1965;308.

[81] HG E. A cavitation algorithm. Transactions of the ASME. 1981 Jul;103(2):350-4. Available from: https://asmedigitalcollection.asme.org/tribology/article/103/3/350/411443/A-Cavitation-Algorithm.

[82] Elrod HG. A Cavitation Algorithm. Journal of Lubrication Technology. 1981 Jul;103(3):350-4. Available from: https://doi.org/10.1115/1.3251669.

[83] Vijayaraghavan D, Keith TG. An Efficient, Robust, and Time Accurate Numerical Scheme Applied to a Cavitation Algorithm. Journal of Tribology. 1990 Jan;112(1):44-51. Available from: https://asmedigitalcollection.asme.org/tribology/article/112/1/44/437239/An-Efficient-Robust-and-Time-Accurate-Numerical.

[84] Ausas R, Ragot P, Leiva J, Jai M, Bayada G, Buscaglia GC. The Impact of the Cavitation Model in the Analysis of Microtextured Lubricated Journal Bearings. Journal of Tribology. 2007 Oct;129(4):868-75. Available from: https://asmedigitalcollection.asme.org/tribology/article/129/4/868/468590/The-Impact-of-the-Cavitation-Model-in-the-Analysis.

[85] Ausas RF, Jai M, Buscaglia GC. A Mass-Conserving Algorithm for Dynamical Lubrication Problems With Cavitation. Journal of Tribology. 2009 Jul;131(3):031702. Available from: https://asmedigitalcollection.asme.org/tribology/article/doi/10.1115/1.3142903/462310/A-MassConserving-Algorithm-for-Dynamical.

[86] Giacopini M, Fowell MT, Dini D, Strozzi A. A Mass-Conserving Complementarity Formulation to Study Lubricant Films in the Presence of Cavitation. Journal of Tribology. 2010 Oct;132(4):041702. Available from: https://asmedigitalcollection.asme.org/tribology/article/132/4/041702/468753/A-Mass-Conserving-Complementarity-Formulation-to.

[87] Woloszynski T, Podsiadlo P, Stachowiak GW. Efficient Solution to the Cavitation Problem in Hydrodynamic Lubrication. Tribology Letters. 2015 Apr;58(1):18. Available from: http://link.springer.com/10.1007/s11249-015-0487-4.

[88] Allen Q, Raeymaekers B. Soft EHL Simulations of Lubricant Film Thickness in Textured Hard-on-Soft Bearings Considering Different Cavitation Models, in the Context of Prosthetic Hip Implants. Tribology Letters.

2021 Dec;69(4):118. Available from: https://link.springer.com/10.1007/s11249-021-01498-8.

[89] Carbone G. Adhesion and friction of an elastic half-space in contact with a slightly wavy rigid surface. Journal of the Mechanics and Physics of Solids. 2004 Jun;52(6):1267-87. Available from: https://linkinghub.elsevier.com/retrieve/pii/S0022509603002060.

[90] Carbone G, Mangialardi L. Analysis of the adhesive contact of confined layers by using a Green's function approach. Journal of the Mechanics and Physics of Solids. 2008 Feb;56(2):684-706. Available from: https://linkinghub.elsevier.com/retrieve/pii/S0022509607001147.

[91] Putignano C, Afferrante L, Carbone G, Demelio G. A new efficient numerical method for contact mechanics of rough surfaces. International Journal of Solids and Structures. 2012 Jan;49(2):338-43. Available from: https://linkinghub.elsevier.com/retrieve/pii/S0020768311003477.

[92] Putignano C. Oscillating viscoelastic periodic contacts: A numerical approach. International Journal of Mechanical Sciences. 2021 Oct;208:106663. Available from: https://linkinghub.elsevier.com/retrieve/pii/S0020740321003970.

[93] Stone HA, Shelley MJ, Boyko E. A note about convected time derivatives for flows of complex fluids. Soft Matter. 2023;19:5353-9. Available from: http://dx.doi.org/10.1039/D3SM00497J.

[94] Batchelor GK. An Introduction to Fluid Dynamics. Cambridge Mathematical Library. Cambridge University Press; 2000.

[95] Snoeijer J H HMA Pandey A, J E. The relationship between viscoelasticity and elasticity. J Proc R Soc A47620200419. 2020;476. Available from: http://doi.org/10.1098/rspa.2020.0419.

[96] Hinch J, Harlen O. Oldroyd B, and not A? Journal of Non-Newtonian Fluid Mechanics. 2021;298:104668. Available from: https://www.sciencedirect.com/science/article/pii/S0377025721001543.

[97] Beris AN. Continuum mechanics modeling of complex fluid systems following Oldroyd's seminal 1950 work. Journal of Non-Newtonian Fluid Mechanics. 2021;298:104677. Available from: https://www.sciencedirect.com/science/article/pii/S0377025721001610.

[98] Bird RB, Curtiss CF, Armstrong RC, Hassager O. Dynamics of Polymeric Liquids, Volume 2: Kinetic Theory. Wiley; 1987. Available from: https://books.google.com.tr/books?id=UG7HQgAACAAJ.

[99] Schuh JK, Ewoldt RH. Low Reynolds number friction reduction with polymers and textures. Journal of Non-Newtonian Fluid Mechanics. 2019 Nov;273:104167. Available from: https://linkinghub.elsevier.com/retrieve/pii/S0377025719300187.

[100] Gamaniel SS, Dini D, Biancofiore L. The effect of fluid viscoelasticity in lubricated contacts in the presence of cavitation. Tribology International. 2021 Aug;160:107011. Available from: https://linkinghub.elsevier.com/retrieve/pii/S0301679X21001596.

[101] Vijayaraghavan D, Keith TG. Development and Evaluation of a Cavitation Algorithm. Tribology Transactions. 1989 Jan;32(2):225-33. Available from: http://www.tandfonline.com/doi/abs/10.1080/10402008908981882.

[102] Guy B. From a compressible fluid model to new mass conserving cavitation algorithms. Tribology International. 2014 Mar;71:38-49. Available from: https://linkinghub.elsevier.com/retrieve/pii/S0301679X13003575.

[103] Sahlin F, Almqvist A, Larsson R, Glavatskih S. A cavitation algorithm for arbitrary lubricant compressibility. Tribology International. 2007

Aug;40(8):1294-300. Available from: https://linkinghub.elsevier.com/retrieve/pii/S0301679X07000400.

[104] Batista M. A cyclic block-tridiagonal solver. Advances in Engineering Software. 2006;37(2):69-74. Available from: https://www.sciencedirect.com/science/article/pii/S0965997805000840.

[105] Batista M, Ibrahim Karawia ARA. The use of the Sherman–Morrison–Woodbury formula to solve cyclic block tri-diagonal and cyclic block penta-diagonal linear systems of equations. Applied Mathematics and Computation. 2009;210(2):558-63. Available from: https://www.sciencedirect.com/science/article/pii/S0096300309000125.

[106] Venner CH, Lubrecht AA. Multilevel methods in lubrication. vol. 37. Elsevier Tribology Series; 2000.

[107] Sari MH, Putignano C, Carbone G, Biancofiore L. The effect of fluid viscoelasticity in soft lubrication. Tribology International. 2024;195:109578. Available from: https://www.sciencedirect.com/science/article/pii/S0301679X2400330X.

[108] Jacobson BO, Hamrock BJ. Non-Newtonian Fluid Model Incorporated Into Elastohydrodynamic Lubrication of Rectangular Contacts. Journal of Tribology. 1984 Apr;106(2):275-82. Available from: https://doi.org/10.1115/1.3260901.

[109] Veltkamp B, Velikov KP, Venner CH, Bonn D. Lubricated Friction and the Hersey Number. Phys Rev Lett. 2021 Jan;126(4):044301. Publisher: American Physical Society. Available from: https://link.aps.org/doi/10.1103/PhysRevLett.126.044301.

[110] Alves MA, Oliveira PJ, Pinho FT. On the effect of contraction ratio in viscoelastic flow through abrupt contractions. Journal of Non-Newtonian Fluid

Mechanics. 2004 Sep;122(1-3):117-30. Available from: https://linkinghub.elsevier.com/retrieve/pii/S0377025704001995.

[111] Ferrás LL, Afonso AM, Alves MA, Nóbrega JM, Pinho FT. Newtonian and viscoelastic fluid flows through an abrupt 1:4 expansion with slip boundary conditions. Physics of Fluids. 2020 Apr;32(4):043103. Available from: https://pubs.aip.org/pof/article/32/4/043103/1080504/Newtonian-and-viscoelastic-fluid-flows-through-an.

[112] Rothstein JP, McKinley GH. Extensional flow of a polystyrene Boger fluid through a 4 : 1 : 4 axisymmetric contraction/expansion. Journal of Non-Newtonian Fluid Mechanics. 1999 Sep;86(1-2):61-88. Available from: https://linkinghub.elsevier.com/retrieve/pii/S037702579800202X.

[113] McKinley GH, Raiford WP, Brown RA, Armstrong RC. Nonlinear dynamics of viscoelastic flow in axisymmetric abrupt contractions. Journal of Fluid Mechanics. 1991 Feb;223(-1):411. Available from: http://www.journals.cambridge.org/abstract_S0022112091001489.

[114] Debbaut B, Marchal JM, Crochet MJ. Numerical simulation of highly viscoelastic flows through an abrupt contraction. Journal of Non-Newtonian Fluid Mechanics. 1988;29:119-46. Available from: https://www.sciencedirect.com/science/article/pii/0377025788850535.

[115] Boger DV. Viscoelastic Flows Through Contractions. Annual Review of Fluid Mechanics. 1987 Jan;19:157-82. Available from: https://www.annualreviews.org/content/journals/10.1146/annurev.fl.19.010187.001105.

[116] Alves MA, Oliveira PJ, Pinho FT. Benchmark solutions for the flow of Oldroyd-B and PTT fluids in planar contractions. Journal of Non-Newtonian Fluid Mechanics. 2003 Feb;110(1):45-75. Available from: https://linkinghub.elsevier.com/retrieve/pii/S037702570200191X.

[117] Keiller RA. Entry-flow calculations for the Oldroyd-B and FENE equations. Journal of Non-Newtonian Fluid Mechanics. 1993 Apr;46(2-3):143-78. Available from: https://linkinghub.elsevier.com/retrieve/pii/037702579385045C.

[118] Binding DM, Phillips PM, Phillips TN. Contraction/expansion flows: The pressure drop and related issues. Journal of Non-Newtonian Fluid Mechanics. 2006 Aug;137(1-3):31-8. Available from: https://linkinghub.elsevier.com/retrieve/pii/S0377025706000772.

[119] Boyko E, Hinch J, Stone HA. Flow of an Oldroyd-B fluid in a slowly varying contraction: theoretical results for arbitrary values of Deborah number in the ultra-dilute limit. Journal of Fluid Mechanics. 2024;988:A10.

[120] Hinch J, Boyko E, Stone HA. Fast flow of an Oldroyd-B model fluid through a narrow slowly varying contraction. Journal of Fluid Mechanics. 2024;988:A11.

[121] Quinzani LM, McKinley GH, Brown RA, Armstrong RC. Modeling the rheology of polyisobutylene solutions. Journal of Rheology. 1990 Jul;34(5):705-48. Available from: https://pubs.aip.org/sor/jor/article/34/5/705-748/238426.

[122] Rodd LE, Scott TP, Boger DV, Cooper-White JJ, McKinley GH. The inertio-elastic planar entry flow of low-viscosity elastic fluids in micro-fabricated geometries. Journal of Non-Newtonian Fluid Mechanics. 2005 Aug;129(1):1-22. Available from: https://linkinghub.elsevier.com/retrieve/pii/S0377025705000893.

[123] Rodd LE, Cooper-White JJ, Boger DV, McKinley GH. Role of the elasticity number in the entry flow of dilute polymer solutions in micro-fabricated contraction geometries. Journal of Non-Newtonian Fluid Mechanics. 2007 May;143(2-3):170-91. Available from: https://linkinghub.elsevier.com/retrieve/pii/S0377025707000493.

[124] Tirtaatmadja V, McKinley GH, Cooper-White JJ. Drop formation and breakup of low viscosity elastic fluids: Effects of molecular weight and concentration. Physics of Fluids. 2006 Apr;18(4):043101. Available from: https://pubs.aip.org/pof/article/18/4/043101/915425/Drop-formation-and-breakup-of-low-viscosity.

[125] Zilz J, Schäfer C, Wagner C, Poole RJ, Alves MA, Lindner A. Serpentine channels: micro-rheometers for fluid relaxation times. Lab Chip. 2014;14(2):351-8. Available from: https://xlink.rsc.org/?DOI=C3LC50809A.

[126] Sousa PC, Vega EJ, Sousa RG, Montanero JM, Alves MA. Measurement of relaxation times in extensional flow of weakly viscoelastic polymer solutions. Rheologica Acta. 2017 Jan;56(1):11-20. Available from: http://link.springer.com/10.1007/s00397-016-0980-1.

[127] Raj A, Sen AK. Flow-induced deformation of compliant microchannels and its effect on pressure–flow characteristics. Microfluid Nanofluid. 2016:20-31.

[128] Lander M. Preparation and Characterization of Polyethylene-oxide (PEO) Solution; 2018.

[129] Del Giudice F, Greco F, Netti PA, Maffettone PL. Is microrheometry affected by channel deformation? Biomicrofluidics. 2016 Jul;10(4):043501. Available from: https://pubs.aip.org/bmf/article/10/4/043501/133938/Is-microrheometry-affected-by-channel-deformation.

[130] Phan-Thien N, Dudek J, Boger DV, Tirtaatmadja V. Squeeze film flow of ideal elastic liquids. Journal of Non-Newtonian Fluid Mechanics. 1985 Jan;18(3):227-54. Available from: https://linkinghub.elsevier.com/retrieve/pii/0377025785870014.

[131] Casanellas L, Alves MA, Poole RJ, Lerouge S, Lindner A. The stabilizing effect of shear thinning on the onset of purely elastic instabilities in serpentine microflows. Soft Matter. 2016;12(29):6159-322.

Appendix A

Polinom Solution of VR

Polynomial Approach

The latter method is the polynomial approximations for stress fields for y dependence. By the equation of 2.32b we can say that τ_{xx} is one order less from the τ_{xy}. The polynomial order for Oldroyds-B stress is determined by mimicking [78] and given such that:

$$\tau_{xx}(x,y,t) = A^I(x,t) + A^{II}(x,t)y + A^{III}(x,t)y^2 + A^{IV}(x,t)y^3 \tag{A.1a}$$

$$\tau_{xy}(x,y,t) = B^I(x,t) + B^{II}(x,t)y + B^{III}(x,t)y^2 + B^{IV}(x,t)y^3 + B^V(x,t)y^4 \tag{A.1b}$$

$$\tau_{yy}(x,y,t) = C^I(x,t) + C^{II}(x,t)y + C^{III}(x,t)y^2 + C^{IV}(x,t)y^3 + C^V(x,t)y^4 \tag{A.1c}$$

Each coefficient in front of y is dependent on position and time. This is an important feature while taking derivatives. By constructing a polynomial in y direction we can directly take derivative y without considering any grid

transformation. In order to find coefficients $A,\ B,\ C$ we use curve fitting for selected points. For xx we need 4 points to make cubic fit and 5 points for xy and yy for 4.th order fit. The points are selected symmetrically in order to make it a consistent fit. It can given in a more compact form in such ways:

$$\begin{bmatrix} \tau_{xx}(x,t,y=0) \\ \tau_{xx}(x,t,y=h/3) \\ \tau_{xx}(x,t,y=2h/3) \\ \tau_{xx}(x,t,y=h) \end{bmatrix} = \begin{bmatrix} 1 & 0 & 0 & 0 \\ 1 & h/3 & (h/3)^2 & (h/3)^3 \\ 1 & 2h/3 & (2h/3)^2 & (2h/3)^3 \\ 1 & h & (h)^2 & (h)^3 \end{bmatrix} \begin{bmatrix} A^I(x,t) \\ A^{II}(x,t) \\ A^{III}(x,t) \\ A^{IV}(x,t) \end{bmatrix}$$

$$\begin{bmatrix} \tau_{xy}(x,t,y=0) \\ \tau_{xy}(x,t,y=h/4) \\ \tau_{xy}(x,t,y=h/2) \\ \tau_{xy}(x,t,y=3h/4) \\ \tau_{xy}(x,t,y=h) \end{bmatrix} = \begin{bmatrix} 1 & 0 & 0 & 0 & 0 \\ 1 & h/4 & (h/4)^2 & (h/4)^3 & (h/4)^4 \\ 1 & h/2 & (h/2)^2 & (h/2)^3 & (h/2)^4 \\ 1 & 3h/4 & (3h/4)^2 & (3h/4)^3 & (3h/4)^4 \\ 1 & h & (h)^2 & (h)^3 & (h)^4 \end{bmatrix} \begin{bmatrix} B^I(x,t) \\ B^{II}(x,t) \\ B^{III}(x,t) \\ B^{IV}(x,t) \\ B^V(x,t) \end{bmatrix}$$

$$\begin{bmatrix} \tau_{yy}(x,t,y=0) \\ \tau_{yy}(x,t,y=h/4) \\ \tau_{yy}(x,t,y=h/2) \\ \tau_{yy}(x,t,y=3h/4) \\ \tau_{yy}(x,t,y=h) \end{bmatrix} = \begin{bmatrix} 1 & 0 & 0 & 0 & 0 \\ 1 & h/4 & (h/4)^2 & (h/4)^3 & (h/4)^4 \\ 1 & h/2 & (h/2)^2 & (h/2)^3 & (h/2)^4 \\ 1 & 3h/4 & (3h/4)^2 & (3h/4)^3 & (3h/4)^4 \\ 1 & h & (h)^2 & (h)^3 & (h)^4 \end{bmatrix} \begin{bmatrix} C^I(x,t) \\ C^{II}(x,t) \\ C^{III}(x,t) \\ C^{IV}(x,t) \\ C^V(x,t) \end{bmatrix}$$

We can call the height property matrix as $\boldsymbol{H_1}$ and $\boldsymbol{H_2}$ for xx, and xy, yy respectively. By taking an inverse matrix we can estimate the coefficients of the polynomials if the stress is known. The given polynomial coefficients vector forms are called T_{xx}, T_{xy}, T_{yy} afterwards to be consistent with Humayun & Luca and coding [78]. The compact form of the stress vectors on the given position can be shown as:

$$\boldsymbol{\tau_{xx}} = \boldsymbol{H_1 T_{xx}} \tag{A.2a}$$

$$\boldsymbol{\tau_{xy}} = \boldsymbol{H_2 T_{xy}} \tag{A.2b}$$

$$\boldsymbol{\tau_{yy}} = \boldsymbol{H_2 T_{yy}} \tag{A.2c}$$

For a known stress on the position the coefficient vector can be shown as:

$$\boldsymbol{T_{xx}} = \boldsymbol{H_1^{-1} \tau_{xx}} \tag{A.3a}$$

$$\boldsymbol{T_{xy}} = \boldsymbol{H_2^{-1} \tau_{xy}} \tag{A.3b}$$

$$\boldsymbol{T_{yy}} = \boldsymbol{H_2^{-1} \tau_{yy}} \tag{A.3c}$$

Equations A.3 and A.2 will be very helpful for us to find stress and its coefficients easily in the latter stages. Using the polynomial approach shines as it eliminates the meshing in y-direction. Thus, the y-derivative of the stress is very straightforward. By using Eqs.A.1a-A.1c, simplify derivative in y by just using $\boldsymbol{H_1}$, $\boldsymbol{H_2}$ matrices. Given such that:

$$\frac{d\boldsymbol{H_1}}{dy} = \begin{bmatrix} 0 & 0 & 0 & 0 \\ 0 & 1 & 2(h/3) & 3(h/3)^2 \\ 0 & 1 & 2(2h/3) & 3(2h/3)^2 \\ 0 & 1 & 2(h) & 3(h)^2 \end{bmatrix} \tag{A.4}$$

$$\frac{d\boldsymbol{H_2}}{dy} = \begin{bmatrix} 0 & 0 & 0 & 0 & 0 \\ 0 & 1 & 2(h/4) & 3(h/4)^2 & 4(h/4)^3 \\ 0 & 1 & 2(h/2) & 3(h/2)^2 & 4(h/2)^3 \\ 0 & 1 & 2(3h/4) & 3(3h/4)^2 & 4(3h/4)^3 \\ 0 & 1 & 2(h) & 3(h)^2 & 4(h)^3 \end{bmatrix} \tag{A.5}$$

Now, discretized the general form of the Oldroyds-B equation can be written similarly to the 2D adaptive mesh formulation 3.26 in matrix form. the derivation is not given as it is very similar to the earlier section. The given form is the most generic stress expression:

$$\boldsymbol{\tau}^{\boldsymbol{t+\delta t}} = \boldsymbol{\tau}^{\boldsymbol{t}} + \delta t \left\{ \boldsymbol{M}\boldsymbol{\tau}^{t} + \boldsymbol{D} - \boldsymbol{u}\frac{d\boldsymbol{\tau}^{t}}{dx} - \boldsymbol{v}\frac{d\boldsymbol{H}_{(.)}}{dy}\boldsymbol{T}^{t}_{(.)} \right\} \tag{A.6}$$

where $\boldsymbol{M}$ and $\boldsymbol{D}$ are the upper convected term matrix and deformation tensor respectively. The vectors are in (3x1) form. To calculate stress in 7 different locations we need to have 7 different stress in the form of equation A.6 with a given position.

After introducing the matrix forms, we can solve the equations. After obtaining the non-transient velocity field from the LIN solver, the transient stress field can be calculated with the help of the polynomials we constructed. So, the first step is to solve LIN for a given profile and use the velocity field that has been calculated. The second step is to determine the initial values of stress for 2D domain similar to the adaptive mesh method. Each stress term has a value for each location of the domain. The initial value problem is solved by assuming the initial stress is the same as the zero-order stress terms calculated by LIN. With this knowledge, $\boldsymbol{D}$ and $\boldsymbol{M}$ are calculated and constant over time.

The initial values help to determine the coefficients with the help of A.3. The x-derivative for the stress is taken from the coefficients by the central difference scheme. Knowing the velocity field and derivatives the equation A.6 can be solved for any y. The new stress $\boldsymbol{\tau}^{\boldsymbol{t+\delta t}}$ is used to calculated new coefficients $\boldsymbol{T}^{\boldsymbol{t+\delta t}}$. Before updating the old stress, the new calculated $\boldsymbol{\tau}^{\boldsymbol{t+\delta t}}$ is used to recalculate the stress. Thus, old stress is updated by using equation A.2 and this process continues until it converges. The convergence is guaranteed by taking the Euclidean norm for each location. The residual is calculated $\boldsymbol{r} = |\boldsymbol{\tau}^{\boldsymbol{t+\delta t}} - \boldsymbol{\tau}^{\boldsymbol{t}}|$. The tolerance has parametric selection by

the time step. The tolerance $Tol = 10^{(-7+log(dt))}$ is arranged after empirical studies.